The Effect of the Parallel Flow on the Ion Resonant Electric Field and the Stability of the Momentum Balance Equations for the Helically Symmetric Experiment

by

Dimitrios Nicolas Michaelides

A dissertation submitted to in partial fulfillment of the requirements for the degree of

Doctor of Philosophy

(Nuclear Engineering and Engineering Physics)

at the

UNIVERSITY OF WISCONSIN – MADISON

2024

Date of final oral examination: 12/19/2023

This dissertation is approved by the following members of the Final Oral committee:

Chris C. Hegna, Professor, Nuclear Engineering and Engineering Physics

David T. Anderson, Professor, Electrical and Computer Engineering

Riccardo Bonazza, Professor, Nuclear Engineering and Engineering Physics

Joseph Talmadge, Staff Scientist, Electrical and Computer Engineering

Abstract

The Helically Symmetric Experiment (HSX) is a quasisymmetric stellarator which has minimal parallel viscous damping in a helical direction. The parallel flow along the magnetic field is similarly weakly damped by viscosity. The momentum balance equations are introduced and solved with the linear model of viscosity and neutral damping to demonstrate this. Shaing's model of nonlinear viscosity is introduced to calculate the ion resonant electric field. We use the self-consistent steady-state parallel and poloidal momentum balance equations to show that a large parallel flow can increase the ion resonant electric field beyond the value calculated using the typical approximation that the parallel flow is zero. By altering the damping of the parallel flow, either by breaking the quasisymmetry or by increasing the neutral density, the resonant ion Er can shift in a controllable fashion. It is shown explicitly there exists stable and unstable steady-state solutions in the two-dimensional space of the parallel flow and radial electric field. A stability analysis of each solution has been performed by calculating the eigenvalues and corresponding eigenvectors of the Jacobian. It is shown that the unstable solution corresponds to a saddle point in which the eigenvalues have opposite signs. The stability analysis indicates that solutions occur when the derivative of the magnitude of the poloidal damping with respect to the magnitude of the radial electric field is negative. A hysteresis is observed when simulating the plasma transition between stable states in both the radial electric field and the parallel flow.

For all generations of my family.

Acknowledgments

This dissertation and my position in life was made possible with the help of many individuals. I am thankful to my mother Laura and father Stathis for their love, support, and guidance throughout the years that have made me into the man I am today. Without you both, I would not have made it anywhere near as far as I have without you, and I am truly blessed to call you both my parents. Hopefully, I have made you proud and will continue to be the favorite child! To my siblings Eleni and Emmanuel, for being sources of encouragement that I can always talk to. I am glad we don't bicker as much as we used to when we were kids!

I would like to thank my many mentors and educators that I have had in my long academic career. First and foremost, I would like to thank Joseph Talmadge. It is no exaggeration to say that this work would not be anywhere near where it is today without you. You helped me understand the project from the start, guided me as I was uncovering results, and have refined my work in each step of the way. You have gone above and beyond your position as a scientist and mentor with your wisdom, guidance, and often saintly patience when working with me through both academic and personal matters. Hopefully you can enjoy retirement more once I'm out!

I would also like to thank my advisors David Anderson and Chris Hegna. In addition to the wonderful education I received from you as a student, I am also grateful for the faith you put in me when I came to you for help. To Simon, Konstantin, and Santhosh for helping me grow in the lab and always having a smiling face I could share a joke with. It is thanks to you that I still have all my fingers. To Benedikt, Rex, Ben, Kyle, and Giorgos thanks for helping me in the lab in the latter days of my time here and for working for the future of HSX. To Riccardo, Carl, and Doug: while I did not interact with you professionally very much, I am thankful that I got to see you as a friendly face in the halls.

To my fellow colleagues at HSX, namely Ian, Alex, Celine, Fernie, Tom, Jason, Wayne, Evan, and all the recent members. Thanks for making that basement a fun place to be and for helping me refine my ideas. To my pals in Pegasus, namely Alex (and Allison), Matt, Temo, and Caroline for sharing stories from across the street. And thanks to my friends from all other walks of life who had to listen to me talk about grad school over the years.

Finally, my eternal thanks to God, who has made me strong in life through faith. Δόξα Πατρί, και Υιώ και αγίω Πνεύματι. Καί νυν και αεί και εις τους αιώνας των αιώνων. Αμήν.

Table of Contents:

List of Figures:

List of Tables:

---1---

Introduction

In the race to make nuclear fusion a viable energy source for mankind, several reactor concepts have been proposed and developed, each with their own advantages and disadvantages. Stellarators use three dimensional magnetic coils to create a confining field and can run at an intrinsically stable regime. However, these coils are difficult to produce due to their complexity. In addition, classical stellarators have had very poor neoclassical particle confinement, where drift orbital losses would lead to the escape of the particles. Modern stellarators have been able to improve confinement, however, due to innovations in design such as Quasi-Helical Symmetry (QHS).

Tokamaks have good neoclassical confinement and have made improvements in transport due to turbulence. In addition to the tokamak's improved confinement regimes, the two-dimensional nature of tokamak coils makes them much easier to produce. However, the two-dimensional coils of tokamaks require an additional power input, such as a driven current to produce a poloidal magnetic field, in the machine in order to confine the plasma, though it is still susceptible to instabilities. This results in the Greenwald density limit [1] as well as limits to other parameters such as current [2]. Because there is a risk of disruptions in tokamaks while stellarators are able to exceed this density limit, this is a problem for tokamaks as fusion reaction rates scale with the square of the density while confinement scales with current, both of which are necessary to maintain fusion reactions.

This thesis focuses on modeling the radial electric field and the plasma flow as well as its effects on the ion resonant electric field in the Helically Symmetric Stellarator (HSX) through

the momentum balance equations. The importance of this topic is that it could lead to an improvement in transport, which could bring the world a step closer to a viable fusion reactor. In tokamaks especially, a reduction in turbulent-driven transport has been observed when the tokamak is able to enter H-mode or super H-mode regimes [3]. Here, H-mode stands for "High Confinement Mode" and Super H-Mode stands for "Super High-Confinement Mode" which has higher pedestal pressure and confinement compared to standard H-mode [4]. These regimes have been observed in other non-tokamak toroidal devices [5, 6], but not all, such as HSX. By better understanding the transition mechanisms from L-mode to H or super H-mode, we can improve the chances of these modes being seen more stellarators and thus further improving their historically lacking confinement. The mechanisms behind these improved confinement states can be seen by examining the radial force balance equation:

$$\boldsymbol{E_r} = \frac{\boldsymbol{\nabla} P_i}{z_i e n_i} - \boldsymbol{V_{\theta i}} B_\zeta + \boldsymbol{V_{\zeta i}} B_\theta \qquad (1.1)$$

where E_r is the radial electric field, ∇P_i is the ion pressure gradient, z_i is the ion charge, n_i is the ion density, θ and ζ are the poloidal and toroidal angles respectively, V is the ion flow, and B is the magnetic field. Turbulence can be suppressed by shear in the ExB flow, generated from the cross product of the electric and magnetic fields, and the radial electric field can be driven by pressure gradients, poloidal flow, and toroidal flow [3]. In H mode, the field is driven by pressure gradient and poloidal flow, while in super H mode, the field is driven by toroidal flow, the direction of symmetry in a tokamak [3].

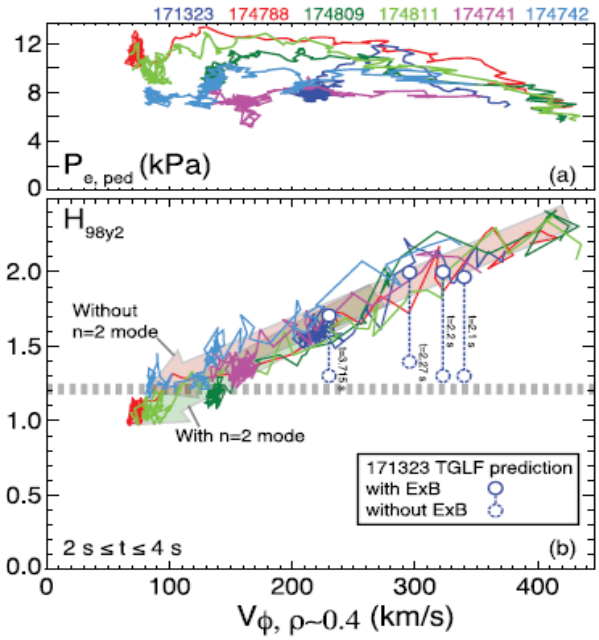

Figure 1. 1 Plasma confinement (H_{98y2}) does not scale with plasma pressure (a) but scales linearly as a function of toroidal rotation (b). *[3]*

As seen in Figure 1.1, the plasma confinement (H_{98y2}) in super H-mode does not scale with pedestal pressure (a) but scales linearly as a function of toroidal rotation, including the ExB flow (b). This result is seen for a number of plasma discharges in DIII-D's super H-mode represented by different colored lines in Figure 1.1. At least some experiments for both stellarators and tokamaks have shown the ability to achieve an H-mode state through a bifurcation in the radial electric field [7, 8] after which the ExB shear suppresses turbulent fluctuations. However, despite some stellarators, such as W7-AS [5] being able to reach H-mode, a stellarator's current H-mode confinement properties are inferior to those of tokamak H-modes.

While not all stellarators are able to reach H-mode, research into the phenomena of how plasma flows affect confinement is critical for the development of future quasisymmetric stellarators [8] that are able to improve plasma confinement by suppressing turbulence via ExB shear. This would help to improve the viability of stellarators as future candidates for a fusion device as stellarators have traditionally had poor confinement properties compared to tokamaks. The confinement of a stellarator would be further improved if it were designed with a QHS configuration, where the magnetic field strength is a constant in a given helical direction, as was demonstrated by the Helically Symmetric Experiment (HSX) [9]. In addition to improving a stellarator's transport properties by reducing the drift orbit losses, the QHS property lowers the viscosity in the direction parallel to the magnetic field and thus allows flow higher flows to exist in that direction. The possibility of improved confinement as well as the inherent stability of stellarators would make them an attractive alternative to tokamaks which suffer from current-driven instabilities in their confined plasma.

1.1 Ion Resonance and Non-Linear Viscosity

In the past, substantial work has been done to locate a resonance in plasma viscosity with respect to the electric field [10, 11, 6, 12]. The theory of this resonance will be covered in detail in Chapter 4 of this document. One can physically interpret the resonance as the point at which the poloidal ExB drift cancels out the rotational transform in the plasma. In certain experiments, the resonance has been seen as the point at which L-H transitions occur [13, 6].

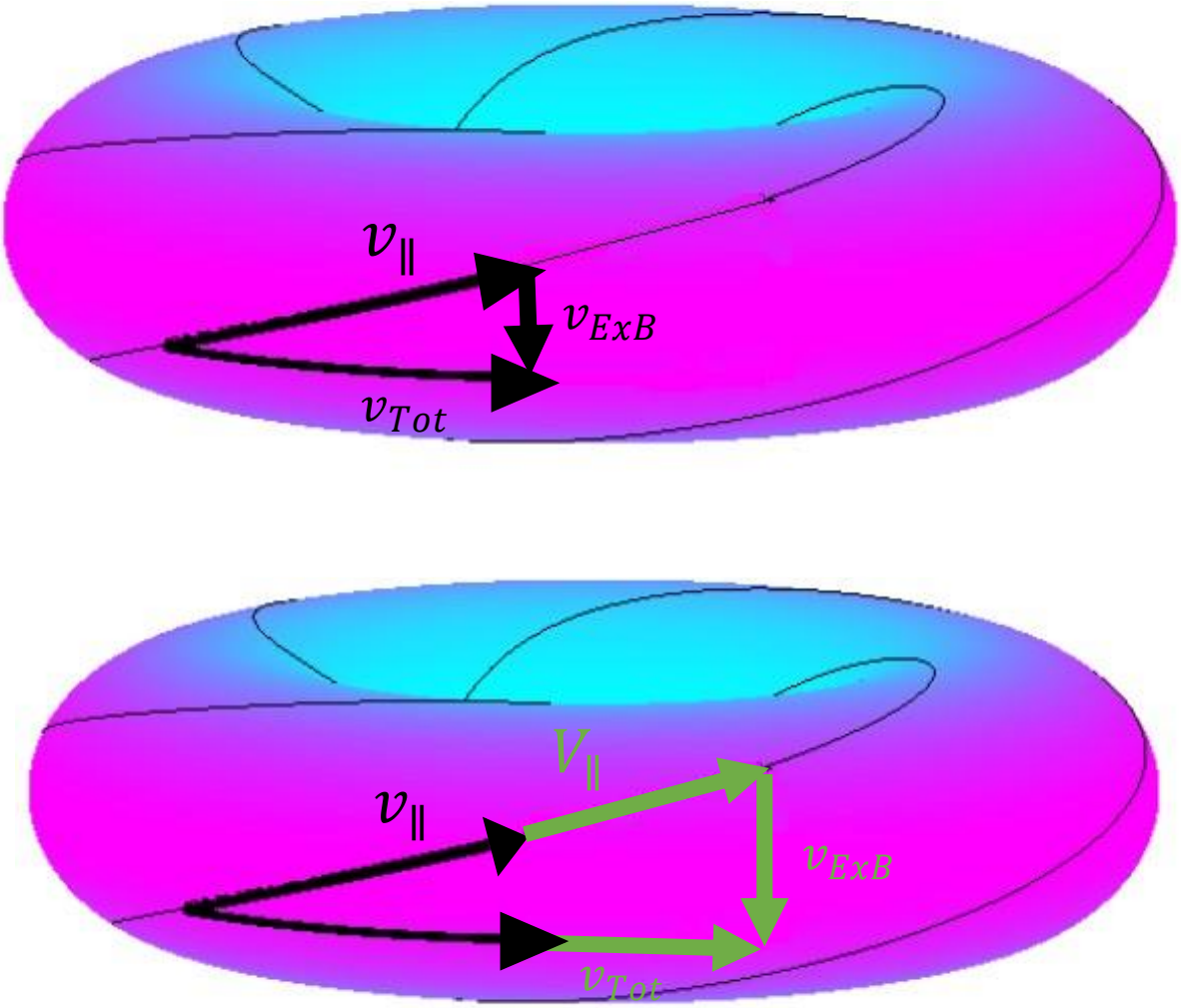

Figure 1. 2 (Top) Physical illustration of flow activity at the resonance. ExB drift cancels out poloidal rotation in plasma resulting in pure toroidal flow. *[14]* (Bottom) The parallel mass flow is added to show that a larger ExB drift is needed to reach the large resonance for values of the parallel mass flow on the order of the parallel flow.

The top of Figure 1.2 gives a physical illustration of the cause of the resonance in the plasma. In the figure, the ExB drift cancels out the poloidal rotation to create a purely toroidal flow [14]. However, when the parallel mass flow, $V_{\parallel}$, is on the order of the parallel particle flow, $v_{\parallel}$, a larger ExB drift is needed to cancel the additional poloidal rotation. This will be discussed further in Chapter 5. Figure 1.2 represents the flow activity in the resonance of a

tokamak where the direction of symmetry and the magnetic Fourier mode is toroidal. The resonance, without taking the parallel mass flow into account, occurs approximately at a point defined by the poloidal Mach number (M_p) and the magnetic spectrum given by the relation:

$$M_p \cong -\left(\frac{m-nq}{m}\right) \tag{1.3}$$

where q=1/ι is the safety factor while m and n are the magnetic mode numbers. The poloidal Mach number is defined as:

$$M_p = -\frac{cE_r}{v_{th}B_p} \tag{1.4}$$

where c is the speed of light, E_r is the radial electric field, v_{th} is the ion thermal velocity, and B_p is the poloidal magnetic field. The derivation of Equation 1.3 is explained in Chapter 4 of this document. Using Equation 1.3 for the QHS configuration of HSX, one of its three main magnetic configurations, one would expect that the resonance could be found around $M_p = 3$, since the dominant mode has m=1, n=4, and q~1. For a tokamak which has magnetic mode numbers m =1 and n =0, one would see this resonance around $M_p = 1$.

Experimentally, this resonance has been seen in other machines by inserting a bias electrode and driving a current which induces a radial electric field in the plasma. These

machines include the Interchangeable Module Stellarator (IMS) [11], the Tohoku University Heliac [6], the CCT tokamak [12], and the TEXTOR tokamak [10]. Evidence of this resonance is seen as a peak in the bias electrode current as a function of bias voltage. This effect can be explained with the poloidal momentum balance equation where once the viscosity peaks and begins to decrease, the external current similarly decreases despite the increasing voltage. This will be covered in greater detail in Chapter 4 of this document.

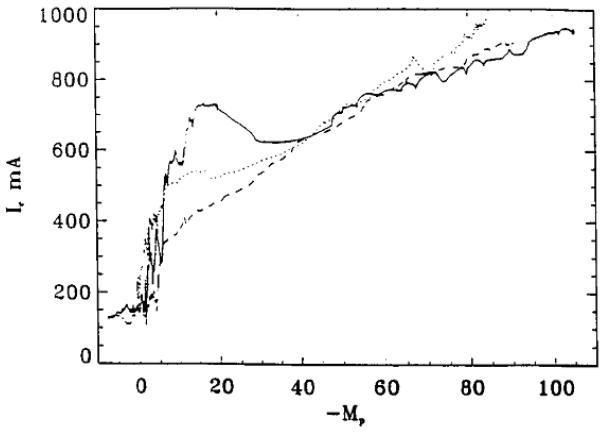

Figure 1. 3. Biasing current vs poloidal Mach number in IMS. Lines represent different plasma discharges with varying neutral density. *[11]* At higher neutral densities, the neutral damping becomes the dominant damping mechanism to the point where a maximum in the viscosity cannot be seen.

Figure 1.3 shows the presence of the resonance in the IMS. The resonance is seen as a peak in electrode current as a function of poloidal Mach number in the solid line. The resonant poloidal Mach number is high due to the magnetic geometry of IMS with m=3, n=7, and q=3 at about r/a=0.7. The other, dashed lines were recorded from different plasma discharges with increased neutral density to show that the resonance can vanish by increasing the neutral

damping to the point where neutral damping is much higher than viscous damping and becomes the dominant damping mechanism.

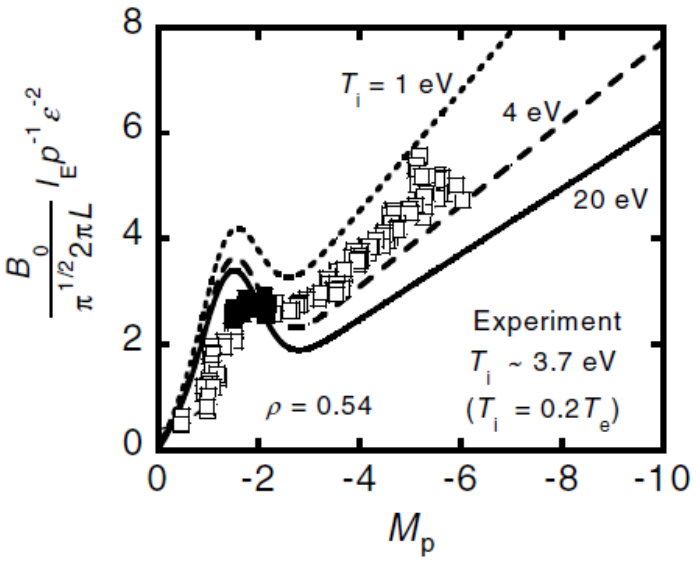

Figure 1. 4. Plasma driving force in the Tohoku Heliac as a function of poloidal Mach number. Experimental values of the driving force are shown as rectangles. Neoclassical modeling results for viscous damping forces are shown as lines for different ion temperatures. *[6]*

Figure 1.4 shows results from the Tohoku University Heliac where an electrode was inserted in the Heliac and the viscosity peak was found, similar to IMS in Figure 1.3. The rectangular points are the normalized electrode current as a function of poloidal Mach number. The solid points indicate values of current measured between the transition of L and H-modes in the Heliac. The peak in the driving force is located where predicted by the calculated viscosity peaks and indicates the resonance point.

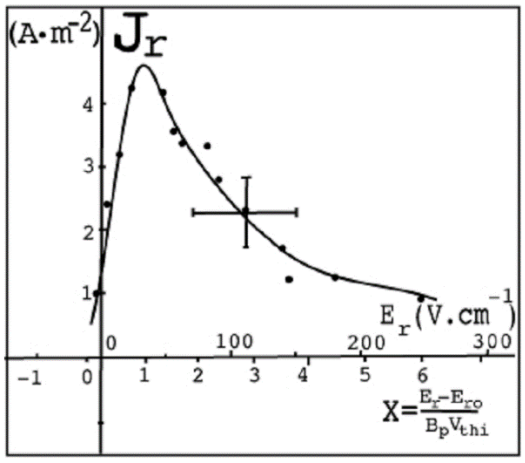

Figure 1. 5: Radial electric field and poloidal Mach number vs current density due to the external bias electrode current in the TEXTOR tokamak. The resonance is seen at a poloidal Mach number value of 1. *[10]*

Figure 1.5 shows the resonance occurring in the TEXTOR tokamak in a similar manner to Figures 1.3 and 1.4 as a peak in current density as a function of the radial electric field or a modified poloidal Mach number denoted by X in Figure 1.6. X differs slightly from M_p due to the subtraction of the normalized pressure gradient, E_{ro}, from the electric field. Here, the peak is seen to occur around X=1.

Despite this resonance being documented in different machines of different classes, it has still not been seen in HSX, despite attempts to locate it. This will be discussed more in Chapter 2.

1.2 Hysteresis Behavior

In certain biasing experiments, such as in the Tohoku University Heliac [13] and LHD [15], hysteresis like behavior was observed. In these experiments, the bias electrode voltage was linearly ramped up to the point where H-mode was achieved, past the peak in the current, and then back down to L-mode.

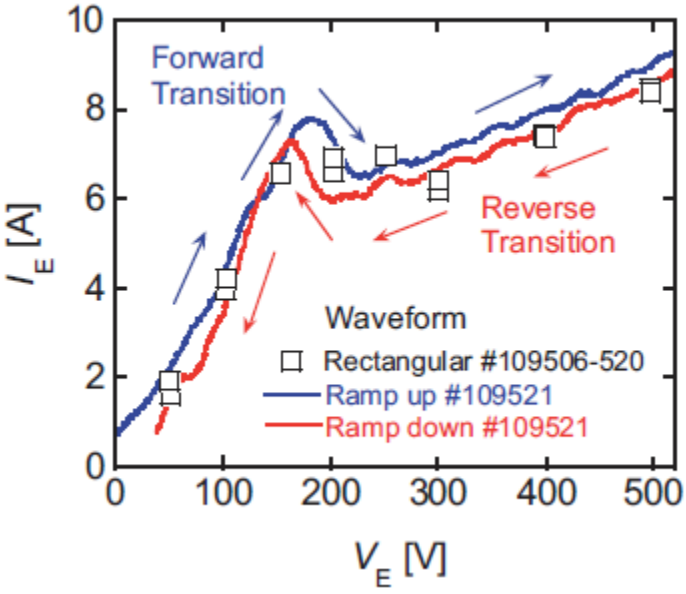

Figure 1.6: The hysteresis in the bias electrode current and voltage profile in LHD *[15]*. The peak in current corresponding to the L-H transition (blue) was seen to occur at a different point than the current peak corresponding to the H-L transition (red).

As seen in Figure 1.6, I-V curve traced out differs depending on whether power to the bias electrode was increasing or decreasing. As such, the peak in the current, and thus, the ion resonance is seen to differ depending on whether the voltage is ramped up or down. Similar results were seen in the Tohoku University Heliac where other parameters such as the electron density and the electron stored energy were seen to display hysteresis behavior during the transitions as well [13]. The existence of a hysteresis has not been offered a sufficient explanation in the past, nor was it predicted in Shaing's model of non-linear viscosity [7], which offers an explanation for the peak in the current as the voltage increases. Shaing's model of

viscosity that explains L-H transitions using the viscosity, and subsequent current, peaks will be discussed more in depth in Chapter 4. This document will explore the behavior and discuss the physical mechanisms that may lead to hysteresis behavior in Chapter 5.

1.3 Direction of Work

This research will explore the role of the parallel flow in determining the ion resonance in a quasihelically symmetric stellarator as well as what an equivalent to an L-H transition may look like in HSX. As explained in the next chapter, data from Bob Wilcox showed that the bias current increased monotonically with the voltage in HSX. Typically, as seen in both IMS and TEXTOR, the current will suddenly decrease with increasing radial electric field after the maximum in poloidal viscosity is reached. Shaing's model of nonlinear viscosity [7] has been used in the past to determine the resonant electric field while assuming that the parallel flow is zero. For most stellarators this is a good assumption since there is large flow damping in all directions. However, for a quasihelical stellarator like HSX this assumption is no longer valid. This topic will be expanded on in Chapter 3.

Solving the momentum balance equations, which will be introduced in Chapter 3, on a flux surface yields two characteristic damping times [16]. The slow damping time corresponds to the direction of quasi-symmetry, which, as Alexis Breismeister demonstrated, is the direction of the maximum flow [14]. It has been shown that at low flow speeds the time evolution of the parallel flow is strongly dependent on the slow damping time [17] while the time evolution of the radial electric field is strongly dependent on the fast damping time. Therefore, it would be expected that with a biased electrode adding momentum to the plasma, the driven parallel flow

might be substantial. However, the data from Stefan Gerhardt showed that in addition to damping due to parallel viscosity and neutrals there was at least one additional unknown damping mechanism in the direction of symmetry [18]. As part of this research we will simulate the parallel flow when a biased electrode is providing a torque on the plasma via an external current and investigate what effect the parallel flow has on the ion resonance. HSX has the ability to vary the viscous damping of the parallel flow with the auxiliary coils, which in turn changes the equilibrium value of the parallel flow. This research will determine whether the difference in parallel flows for the Mirror and F14 configurations, which HSX achieves using auxiliary coils, yields a clear difference in the resonant electric field in those configurations from the resonant electric field in QHS.

Extending the work at low flow speeds, the time dependence of the radial electric field and parallel flows will be solved with the inclusion of Shaing's nonlinear viscosity and the numerically calculated basis vectors of HSX. By simulating the time dependence of the momentum balance equation, the stability of different solutions to the equations as well as the physical mechanisms that cause certain solutions to be unstable, and thus experimentally improbable to see, can be understood. The information obtained for this thesis will be helpful to explore the possibility of obtaining higher confinement regimes in stellarators due to the potentially high poloidal . In addition, if the ion resonance is shown to depend on the parallel flow, then codes such as PENTA [19], which have been used for neoclassical calculations on HSX, may not provide accurate results for HSX. This subject will be discussed in greater detail in Chapter 6 of this document.

Chapter 2 focuses on HSX, its typical machine parameters, unique properties, and past research that has been performed on this machine. As HSX will be the focus of the work done in

this document, the plasma parameters outlined in that chapter will be used throughout the rest of this document. Chapter 3 introduces the momentum balance equations and the Hamada coordinate system in which they are solved. Using linear viscosity, the equations are solved analytically to demonstrate how the parallel flow in the QHS configuration is very weakly damped by viscosity and provides motivation to include the parallel flow when calculating the ion resonant electric field. Chapter 4 introduces Shaing's viscosity model and how the maximum in viscosity is generated and the variables that affect it. Computational simulations of this effect are described in Chapter 4 on how Shaing's viscosity model applies to HSX. These simulations show multiple solution states to the momentum balance equations, highlight the importance of plasma flows in HSX, and offer explanations as to why the resonance has not yet been observed in HSX. Chapter 5 looks at the time evolution of the radial electric field and the parallel flow. The stabilities of different solution states are examined and the equivalent of an L-H transition in HSX is simulated. Finally, Chapter 6 summarizes the work and its conclusions in addition to proposing future experimental and computational work to be performed.

References

[1] M. Greenwald, "Density limits in toroidal plasmas," *Plasma Physics and Controlled Fusion,* vol. 44, no. 8, p. R27, 2002.

[2] H. R. Koslowski, "Operational Limits and LImiting Instabilites in Tokamak Machines," *Fusion Science and Technology,* p. 115, 2004.

[3] S. Ding et al, "On the very high energy confinement observed in super H-Mode DIII-D experiments," *Nuclear Fusion,* vol. 60, no. 3, p. 034001, 2020.

[4] e. a. M. Knolker, "Optimizing the Super H-mode pedistal to improve performance and facilitate divertor integration," *Physics of Plasmas,* p. 102506, 2020.

[5] F. Wagner et al, "H-Mode of the W7-AS Stellarator," *Plasma Physics and Controlled Fusion,* vol. 36, p. A61, 1994.

[6] S. Kitajima et al, "LH transition by a biased hot cathode in the Tohoku University Heliac," *Nuclear Fusion,* vol. 46, no. 2, p. 200, 2006.

[7] K. C. Shaing, "Test of tokamak low-mode-high-mode transition theory in stellarators," *Physics of Fluids B: Plasma Physics,* vol. 5, no. 11, p. 3841, 1993.

[8] F. Wagner et al, "W7-AS: One Step of the Wendelstein Stellarator Line," *Physics of Plasmas,* vol. 12, no. 7, p. 072509, 2005.

[9] J. M. Canik et al, "Experimental Evidence of Reduced Plasma Flow Damping with Quasisymmetry," *Physical Review Letters,* vol. 98, no. 8, pp. 015002-1, 2007.

[10] R. R. Weynants, S. Jachmich and M. Van Schoor, "Electrode Biasing on TEXTOR: A Tool for Fundamental Physics Studies," *Fusion Science and Technology,* vol. 47, no. 2, p. 202, 2005.

[11] H. Dahi, "Nonlinear Viscosity in the Interchangeable Module Stellarator," *University of Wisconsin-Madison,* 1997.

[12] R. J. Taylor et al, "H-Mode behavior induced by cross-field currents in a tokamak," *Physical Review Letters,* vol. 63, no. 21, p. 2365, 1989.

[13] H. Takahashi and et al, "Hysteresis during transition into improved mode on biasing experiment under the electrode current control in Tohoku University Heliac," *Plasma Physics and Controlled Fusion,* vol. 48, no. 1, p. 39, 2005.

[14] A. Briesmeister, "Measurement and Modeling of the Flows and Radial Electric Field in the HSX Stellarator," *University of Wisconsin-Madison,* 2013.

[15] S. Kitajima, "Transition of Poloidal Viscosity by Electrode Biasing in the Large Helical Device," *Nuclear Fusion,* vol. 53, no. 7, p. 073014, 2013.

[16] M. Coronado and J. N. Talmadge, "Evolution of the plasma rotation and the radial electric field for a toroidal plasma in the Pfirsch-Schluter and plateau regimes subject to a biased electrode," *Physics of Plasmas,* vol. 5, no. 4, p. 1200, 1993.

[17] J. N. Talmadge, "Evolution of plasma flow and radial electric field in HSX," in *APS DPP*, Portland, OR, 2018.

[18] S. Gerhardt, "Measurements and Modeling of the Plasma Response to Electrode Biasing in the HSX Stellarator," *University of Wisconsin-Madison,* 2004.

[19] D. A. Spong, "Generation and damping of neoclassical plasma flows in stellarators," *Pysics of Plasmas,* vol. 12, no. 5, p. 056114, 2005.

---2---

The HSX Stellarator

The Helically Symmetric Experiment is a unique in that it is the only stellarator that is quasihelically symmetric (QHS). In addition to this configuration, it has a set of auxiliary coils that allow for the quasisymmetry to be broken. This allows the physics properties of the QHS configuration to be compared to that of a more traditional stellarator. In this thesis we are interested specifically in how the parallel viscosity differs between the various configurations. Section 2.1 of this chapter will describe the QHS configuration and the mechanisms by which HSX changes configurations. Section 2.2 discusses the machine and plasma parameters of HSX. Finally, Section 2.3 will present a summary of previous work done on HSX that relates to the measurement of plasma flow and radial electric field.

2.1 HSX Configurations

In the QHS configuration, there is a constant magnetic field strength along the helical direction of quasisymmetry which is analogous to the toroidal direction of a tokamak. Except that in a tokamak it's the vector **B** that is preserved along the toroidal direction, not just the field magnitude.

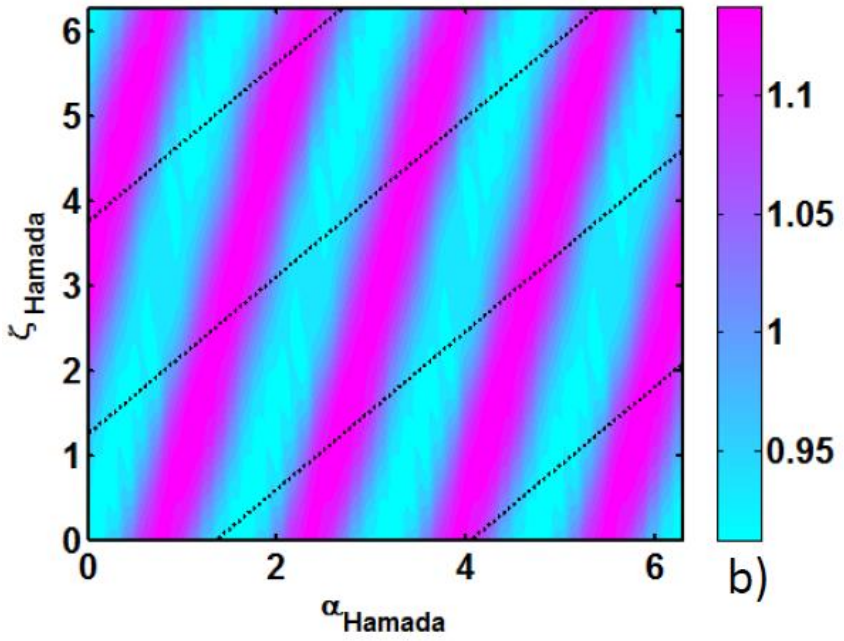

Figure 2. 1 The magnetic field strength of HSX as a function of the poloidal (ζ) and toroidal (α) angles. The dashed lines indicate the direction of the magnetic field. *[1]*

As seen in Figure 2. 1 the magnetic field strength remains constant in a helical direction that orbits poloidally 4 times, for every toroidal orbit [1]. HSX has shown that the QHS configuration reduces neoclassical transport of heat and particles compared to conventional stellarators [20]. This is achieved by having a single dominant mode in the magnetic field spectrum, compared to a conventional stellarator which has a multiplicity of modes. It is the combination of toroidal and helical spectral components that the endpoints of a banana particle orbits are not on the same flux surface. It also allows for high plasma flows in the direction of symmetry [1].

In general, for stellarators, magnetic field strength, B, can be written as

$$B = B_o\left(1 + \sum_{m,n} \varepsilon_{mn} cos\ (m\theta - n\zeta)\right) \qquad (2.1)$$

where B_o is the total field strength, ε_{mn} is the amplitude of a magnetic mode defined by mode numbers m and n, and ζ and θ are the toroidal and poloidal angles. A unique property of the QHS configuration, where the dominant magnetic mode is (n,m)=(4,1), is that it has a high effective transform $\iota_{eff}=n-m\iota\approx 3$ where ι is the nominal transform and varies from 1.04 at the magnetic axis to 1.12 at the edge. A high effective transform leads to small drifts of passing particles from a flux surface, low neoclassical transport, and small plasma currents [3].

HSX can also be configured in other modes where the symmetry is broken with planar auxiliary magnetic coils.

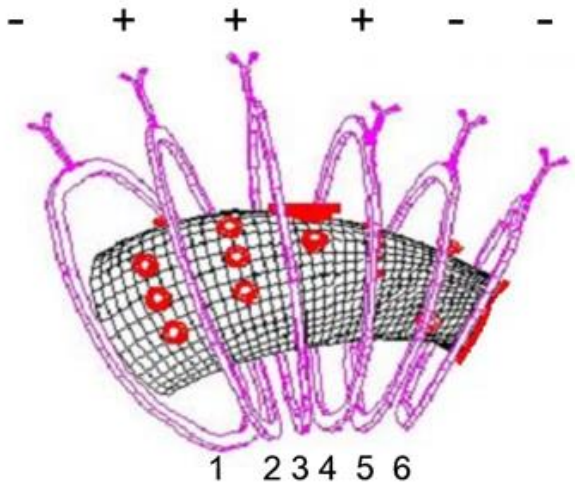

Figure 2.2 A diagram of the poloidal direction of auxiliary currents for the F14 configuration *[4]*.

Figure 2.2 shows how the planar auxiliary coils are activated in HSX in order to break the quasisymmetry of the QHS mode. Although there are 48 auxiliary coils, only six (one-half of a field period) are shown in the figure, because the remaining coils follow stellarator symmetry over four periods. In the figure, plus means the current is in the same direction as the main

modular coils, which are three dimensional, minus means the current is in the opposite direction. In the F14 configuration, they are turned on with current directions as shown in the figure. In the Mirror configuration, the directions of current are reversed for coils 1 and 4. That is, the configuration for the Mirror is [+ + + - - -]. This creates a magnetic configuration in which the transport resembles a conventional stellarator due to an increase in amplitude of other symmetry-breaking modes in the magnetic spectrum The difference in both neoclassical transport and viscous damping for the Mirror and F14 configurations is due to the difference in strength of the different symmetry-breaking modes.

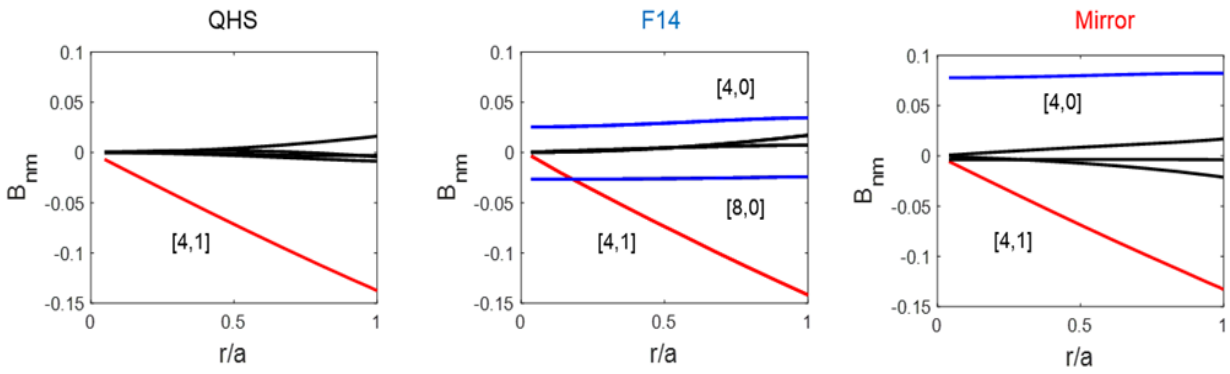

Figure 2. 3 The leading five spectral components for each configuration of HSX as a function of r/a. F14 and Mirror configurations are obtained by using auxiliary coils to degrade the designed QHS symmetry. *[5]*

The mode spectrum shown in Figure 2. 3 is given in Hamada coordinates [6]. The reason for this choice of a coordinate system is explained in Chapter 3. As seen in the left most plot of Figure 2. 3, the (n,m) = (4,1) mode dominates in the QHS configuration. In the Flip 1-4 (F14) and Mirror configurations where the quasisymmetry is broken, on the middle and right of Figure 2. 3 respectively, other modes, specifically the (4,0) and the (8,0) modes in the F14 configuration

and especially the (4,0) mode in the Mirror configuration, become comparable to or even exceed that of the (4,1) mode close to the core.

2.2 HSX Parameters

HSX has a 1.2m major radius, a 12cm minor radius, and a maximum field strength of 1T. It has 48 magnetic coils in 6 unique shapes that are distributed across 4 periods. In addition to these, there are the auxiliary coils, discussed above, which enable the quasisymmetry to be altered. The plasma in HSX is generated and heated with two 28GHz gyrotrons which provide a total heating power of 100kW of electron cyclotron resonant heating (ECRH). The ECRH heating is directed into the plasma by a transmission line and set of mirrors in the vacuum vessel which launch the first harmonic ordinary electron cyclotron wave perpendicular to the magnetic flux surfaces.

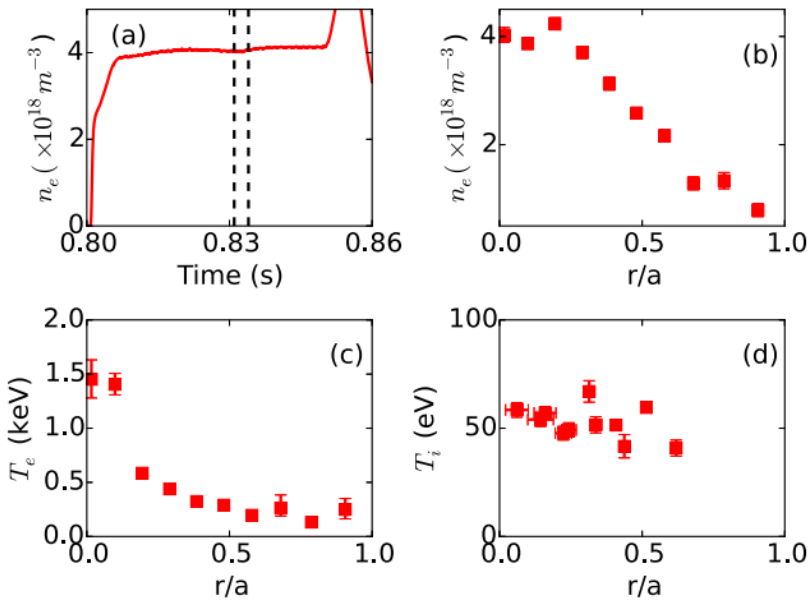

Figure 2. 4 Plasma parameters in the QHS configuration. Line averaged electron density (a), radial profiles of electron density (b) and electron temperature (c) measured at 0.82s into the discharge, and C^{+6} ion temperatures (d). Vertical dashed lines on (a) represent start and end times of the diagnostic neutral beam. *[7]*

Figure 2. 4 shows typical HSX machine parameters in the QHS configuration with the magnetic field at 1T measured by a Thomson scattering system, an interferometer, and Charge Exchange Recombination Spectroscopy (CHERS) diagnostics. All three of these diagnostics are optical diagnostics. The Thomson system scatters photons off the electrons in the plasma, with the change in frequency from the scattered photons being measured to calculate the electron temperature of the plasma [8]. The interferometer uses the plasma to create an interference pattern from a beam of light with known energy. The interference pattern created by the known beam combined with light that had traveled through the plasma can be used to measure the plasma density [9]. The CHERS system injects neutral atoms into the plasma [10]. The neutrals donate electrons to ionized particles at an excited state. As the electrons decay to less excited

states, they produce photons which can be measured to determine the impurity ion temperature and plasma flow.

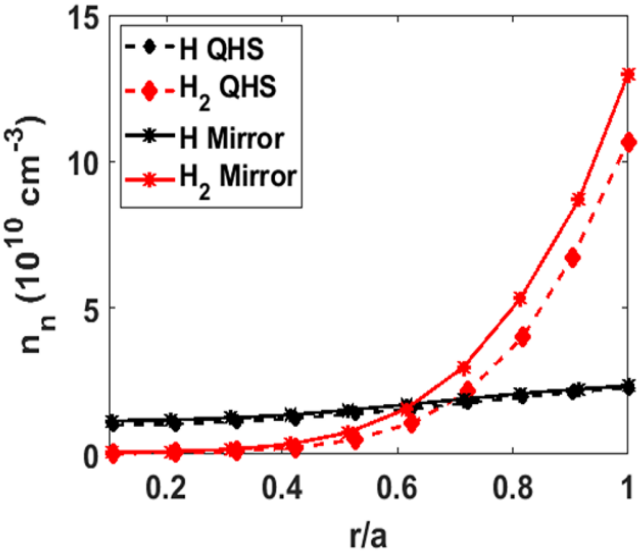

Figure 2. 5 The neutral density of hydrogen calculated by DEGAS in HSX plotted for the QHS (diamond) and Mirror (star) configurations for both atomic (black) and molecular (red) hydrogen. *[11]*

Figure 2. 5 shows a neutral density profile of hydrogen calculated by DEGAS in HSX's QHS and Mirror configurations [11]. This profile was constructed with data obtained using H_α detector array measurements in HSX. Future experiments will search for the resonant electric field by placing diagnostic probes at a position of r/a=0.7, where r is the radial distance from the center of the machine and a is the minor radius. For this reason, the values corresponding to r/a=0.7 from Figure 2. 4 and Figure 2. 5 will be used in the calculations shown in the following Chapters. It will also be assumed for the calculations presented later that the plasma parameters in the Mirror and F14 configurations are the same as in the QHS configuration. This is to enable

differences in the plasma flow and radial electric [12]field to be due solely to the magnetic field spectrum for each configuration and not to differences in plasma parameters.

2.3 Previous Work on HSX

Work has previously been performed by graduate students and scientists on HSX to study plasma flow and electric field in HSX. [1, 13, 11, 14]. Stefan Gerhardt measured the flow using a Mach probe, which measures the velocity of a plasma by measuring the potential difference between two Langmuir probes separated by a barrier, and determined the rate and direction of flow decay on different timescales [13]. These decay rates were compared to the Coronado and Talmadge (C&T) model of flow and electric field decay which established distinct "fast" and "slow" timescales over which both the radial electric field and parallel flow evolved [15].

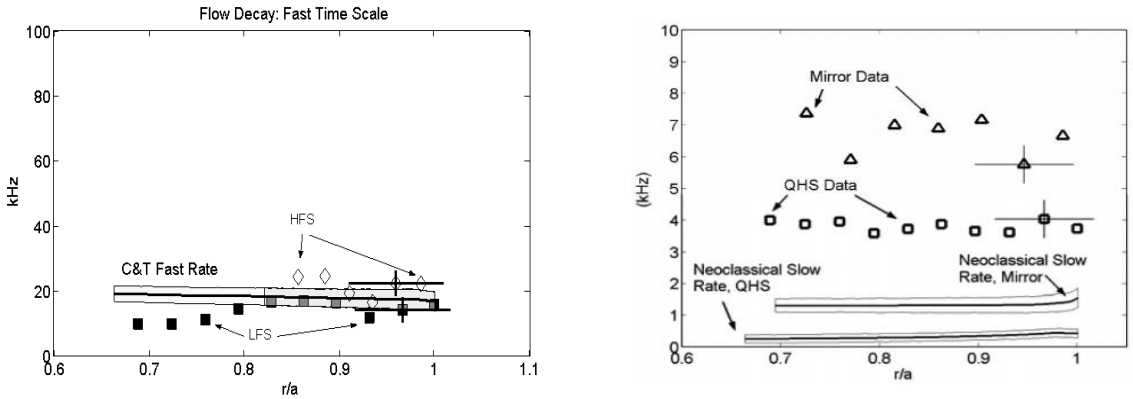

Figure 2. 6 On the left, fast flow decay rate as a function of r/a in the QHS configuration. The experimental values measured on the High Field Side (diamonds) and the Low Field Side (squares) were compared to the C&T model (solid line). On the right, slow flow decay rate as a function of r/a in the QHS (square) and mirror (triangle) configurations. The experimental values are compared to the C&T model (solid lines) for each configuration *[16, 13]*

The left side of Figure 2. 6 compares the experimental results from measurements of the fast time scale of flow decay to the theoretical calculation of the fast time scale using the C&T model. As can be seen, the model agrees very well with the experimental results measured on both the high and low field side of HSX. The right side of Figure 2. 6 shows experimental measurements of the slow timescale compared to calculations from the C&T model for both the QHS and Mirror configurations. It is clear that neither configuration shows good agreement between the theoretical and experimental results. The flows in both configurations are damped much faster than the model predicts, with the QHS model off by about an order of magnitude. However, the difference between the experimentally measured slow decay rates in Mirror and QHS configurations is roughly in agreement with the difference between the decay rates calculated by the C&T model for the Mirror and QHS configurations. This indicates the possible presence of other damping mechanisms present in HSX not included in the C&T model, such as turbulence.

Alexis Briesemeister used a CHERS system to measure the plasma flow velocity and ion temperature in HSX [1]. CHERS is a spectroscopy system utilizing a neutral hydrogen beam to stimulate light emission in the plasma. The system can measure temperature, density, and velocity, from which other quantities such as the radial electric field can be calculated using the radial force balance Equation 1.1. She measured flows as high as 20 km/s towards the core, as seen in Figure 2. 7. The flows were measured in the absence of an external bias and without an external momentum source in the QHS configuration.

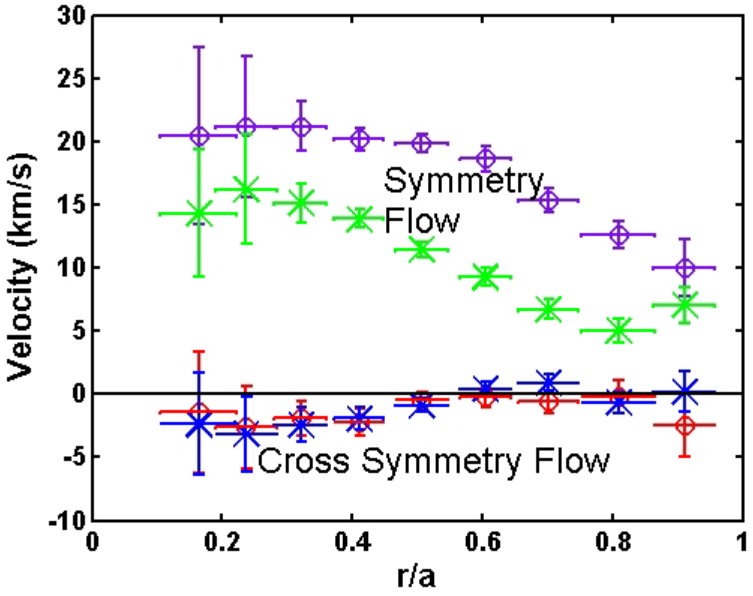

Figure 2. 7 Plasma flows measured along the direction of symmetry (purple and green) and cross symmetry (red and blue) in QHS as a function of r/a. X marks indicate 50 kW of heating power while O marks indicate 100 kW of heating power. *[12]*

Figure 2. 7 shows that flows are sustained in HSX's direction of quasisymmetry due to the reduced parallel viscous damping, even close to the edge and that the flow increases with increased heating power [12]. Since the parallel direction is close to the direction of quasisymmetry, it benefits greatly from the reduced viscosity. These flows occur naturally in the machine as a result of the energy input from the gyrotrons to heat the plasma. This is opposed to the velocity in the cross-symmetry direction which is unable to sustain much plasma flow due to the increased viscosity that acts as a damping mechanism.

Tom Dobbins studied flow discrepancies between experimental and neoclassical modeling results in HSX using the CHERS system. He used H_α measurements with the DEGAS code to produce neutral density profiles for HSX, as seen in Figure 2. 5. He determined that the neutral damping on plasma flows plays a greater role in the QHS configuration than other configurations in which the quasisymmetry is degraded due to the lower viscosity in the QHS

configuration's direction of symmetry. In particular, Dobbins modified the PENTA code to include damping due to neutrals, where charged particles lose energy as they collide with neutral particles in the machine, and compared it to experimental results. Figure 2. 8 shows that including neutral damping in PENTA brings the calculated results to match the experimental measurements much better than calculations done without neutrals.

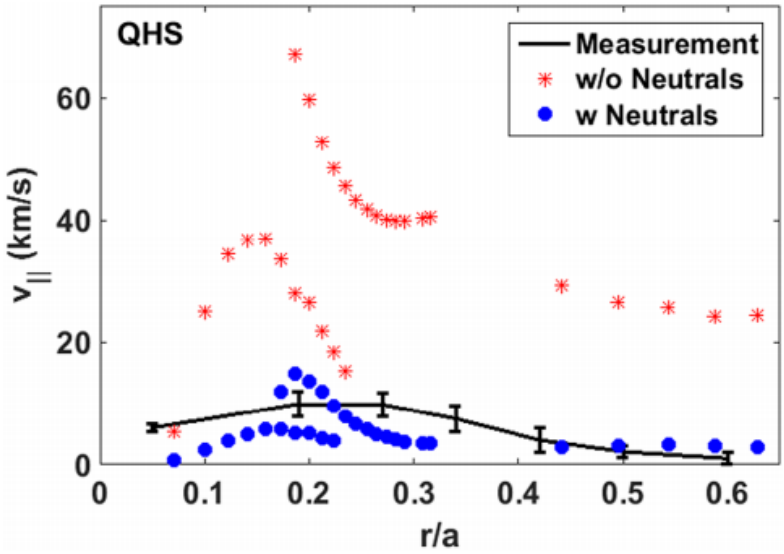

Figure 2. 8 Parallel plasma flow as a function of r/a. Experimental results (black line) are compared to PENTA calculations with and without neutrals (blue and red respectively) *[11].*

The multiple solutions seen in Figure 2. 8 are due to the electron and ion root solutions to the ambipolarity condition. Of these two roots, the electron root predicts larger values of parallel velocity and has not been seen in the HSX core as calculated. While the inclusion of neutrals in the PENTA code improves the agreement between the experimental measurements and the modeling, neutrals do not fully account for the discrepancy in the slow decay rate seen in Gerhardt's work. In that work only a neutral density approximately 10 times the experimental

value was there agreement between the measured slow rate and the model. This indicates the possibility that are other mechanisms that influence plasma flow for the QHS configuration.

Santhosh Kumar showed that radial electric field and parallel flow could be obtained by measuring the total ion flow at two locations on a flux surface. This work was done in order to investigate why a very large positive electron root of the ambipolarity constraint that was calculated using the PENTA code could not be found experimentally close to the plasma core. In this method, the CHERS neutral beam is injected through the center of the plasma profile. By taking measurements along the inboard and the outboard sides of the neutral beam shown in Figure 2. 9, the contribution of the Pfirsch-Schlüter flow to the total ion flow could be measured. These measurements show counter-streaming Pfirsch-Schlüter flows, and from the difference of the flows, the radial electric field and mean flow may be calculated directly without using the radial force balance equation.

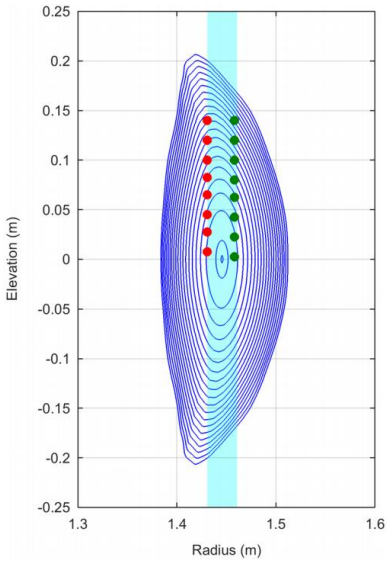

Figure 2. 9 HSX plasma profile showing the path of neutral beam injection (cyan) and the location of inboard (red) and outboard (green) measurements. *[7]*

Bob Wilcox attempted to search for the resonance in HSX. By inserting a bias electrode attached to a capacitor bank into the plasma and activating the electrode during a discharge, he was able to drive a current and induce a radial electric field. By plotting the electrode current against the voltage, the resonance would be seen as a peak in the current, similar to the peaks seen in Figures 1.4, 1.5, and 1.6.

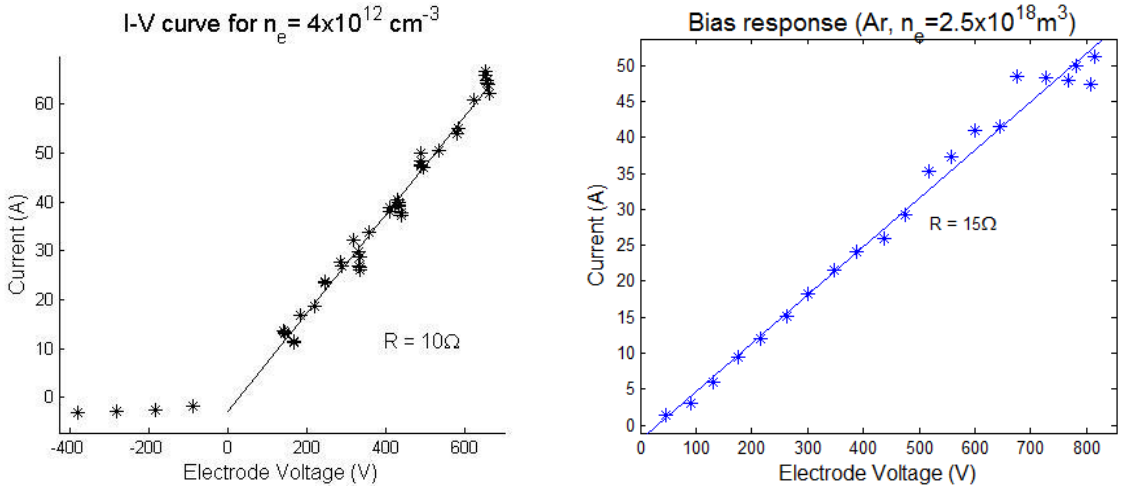

Figure 2. 10 Current and voltage of bias electrode discharges in HSX. Each point represents an individual discharge in hydrogen (left) and argon (right). *[14]*

Figure 2. 10 shows Wilcox's attempts to locate the resonance in both hydrogen (left) and argon (right). The experiments were performed in argon as ions are 40 times heavier than hydrogen which would lead to the resonant electric field being about a factor of 6 less in argon than in hydrogen. The electrode was inserted to the plasma at a position of r/a=0.8. At this point, based on calculations using Equation 1.3, the resonance should be seen in hydrogen at around 600V and in argon close to 100V. However, both plots in Figure 2. 10 show a linear relation between voltage and current with no indication of the resonance.

The data from Bob Wilcox showed that the bias current increased monotonically with the voltage in HSX. Typically, as seen in both IMS and TEXTOR, the current will suddenly decrease with increasing radial electric field after the maximum in poloidal viscosity is reached. Shaing's model of nonlinear viscosity [17] has been used in the past to determine the resonant electric field while assuming that the parallel flow is zero. For most stellarators this is a good assumption since there is large flow damping in all directions. However, for a quasihelical stellarator like HSX this assumption is no longer valid.

Solving the momentum balance equations on a flux surface yields two characteristic damping times[18]. The slow damping time corresponds to damping in the direction of quasi-symmetry, which, as Alexis Briesemeister demonstrated, is the direction of the maximum parallel flow [1]. It has been shown that at low flow speeds the time evolution of the parallel flow is strongly dependent on the slow damping time [5] while the time evolution of the radial electric field is dependent on the both the slow and fast damping time. This will be explained in the next chapter.

It would be expected that with a biased electrode adding momentum to the plasma, the driven parallel flow might be substantial. However, the data from Stefan Gerhardt showed that in addition to damping due to parallel viscosity and neutrals there was an additional unknown damping mechanism in the direction of symmetry [13]. As part of this research, we will simulate the parallel flow when a biased electrode is providing a torque on the plasma and investigate what effect the parallel flow has on the ion resonance. HSX has the ability to vary the viscous damping of the parallel flow with the auxiliary coils, which in turn changes the equilibrium value of the parallel flow. This research will demonstrate that the difference in parallel flows for the

Mirror and F14 configurations yields a clear difference in the resonant electric field in those configurations from the resonant electric field in QHS.

Extending the work at low flow speeds, the time dependence of the radial electric field and parallel flows will be solved with the inclusion of Shaing's nonlinear viscosity and the numerically calculated basis vectors of HSX. By simulating the time dependence of the momentum balance equation, the stability of different solutions to the equations as well as the physical mechanisms that cause instabilities can be understood. The information obtained for this thesis will be helpful to explore the possibility of obtaining higher confinement regimes in stellarators. In addition, if the ion resonance is shown to depend on the parallel flow, then codes such as PENTA, which have been used for neoclassical calculations on HSX, may not provide accurate results for HSX. This subject will be discussed in greater detail in Chapter 6 of this document.

References

[1] A. Briesmeister, "Measurement and Modeling of the Flows and Radial Electric Field in the HSX Stellarator," *University of Wisconsin-Madison,* 2013.

[2] J. M. Canik et al, "Experimental Evidence of Reduced Plasma Flow Damping with Quasisymmetry," *Physical Review Letters,* vol. 98, no. 8, 2007.

[3] J. N. Talmadge, V. Sakaguchi, F. S. B. Anderson, D. T. Anderson and A. F. Almagri, "Experimental determination of the magnetic field spectrum in the Helically Symmetric Experiment using passing particle orbits," *Physics of Plasmas,* vol. 8, no. 12, pp. 5165-5170, 2001.

[4] J. Canik, "Experimental Verification of Reduced Particle and Electron Heat Transport with Quasisymmetry in the HSX Stellarator," *University of Wisconsin-Madison,* 2007.

[5] J. N. Talmadge, "Evolution of plasma flow and radial electric field in HSX," in *APS DPP*, Portland, OR, 2018.

[6] S. Hamada, "Hydromagnetic equilibria and their proper coordinates," *Nuclear Fusion,* vol. 2, p. 23, 1962.

[7] S. T. A. Kumar et al, "Determination of radial electric field from Pfirsh-Schluter flows in the HSX stellarator," *Nuclear Fusion,* vol. 57, no. 3, 2017.

[8] J. S. R. L. D. S. H. G. D. H. Froula, "Thomson-scattering techniques to diagnose local electron and ion temperatures, density, and plasma wave amplitudes in laser produced plasmas," *Review of Scientific Instruments,* vol. 77, no. 10, p. 10E522, 2006.

[9] M. S. T. S. S. Harilal, "Laser plasma density measurements using interferometry," Fusion Division, Center for Energy Research, San Diego, CA, 2004.

[10] R. C. Isler, "An overview of charge exchange spectroscopy as a plasma diagnostic," *Plasma Physics and Controlled Fusion,* vol. 36, no. 2, p. 171, 1994.

[11] T. Dobbins, S. T. A. Kumar, J. N. Talmadge and D. T. Anderson, "The role of neutral friction in governing parallel flows in the HSX stellarator," *Nuclear Fusion,* vol. 59, no. 2, p. 046007, 2019.

[12] A. Briesemeister, K. Zhai, D. T. Anderson, F. S. B. Anderson, J. Lore and J. N. Talmadge, "Flow Velocity Measurements Using ChERS in the HSX Stellarator," *Contributions to Plasma Physics,* vol. 50, no. 8, p. 741, 2009.

[13] S. Gerhardt, "Measurements and Modeling of the Plasma Response to Electrode Biasing in the HSX Stellarator," *University of Wisconsin-Madison,* 2004.

[14] R. Wilcox, *HSX Group Meeting,* Madison, WI, 2012.

[15] M. Coronado and J. N. Talmadge, "Evolution of the plasma rotation and the radial electric field for a toroidal plasma in the Pfirsch-Schluter and plateau regimes subject to a biased electrode," *Physics of Plasmas,* vol. 5, no. 4, p. 1200, 1993.

[16] S. Gerhardt, J. N. Talmadge, J. M. Canik and D. T. Anderson, "Experimental Evidence of Reduced Plasma Flow Damping with Quasisymmetry," *Physical Review Letters,* vol. 24, no. 3, p. 015002, 2005.

[17] K. C. Shaing, "Test of tokamak low-mode-high-mode transition theory in stellarators," *Physics of Fluids B: Plasma Physics,* vol. 5, no. 11, p. 3841, 1993.

[18] M. Coronado and J. N. Talmadge, "Evolution of the plasma rotation and the radial electric field for a toroidal plasma in the Pfirsch-Schluter and plateau regimes subject to a biased electrode," *Physics of Plasmas,* vol. 5, no. 4, 1993.

---3---

Demonstrating the Importance of the Parallel Flow in HSX Using Linear Viscosity in the Momentum Balance Equations

In this Chapter, we introduce the momentum balance equations that will be focal point of the rest of this work. Transforming the equations into Hamada coordinates and using linear viscosity (along with neutral damping) allows for the equations to be solved analytically. The major result from this is to demonstrate clearly that the parallel flow is only very weakly damped by viscosity for the QHS configuration, similar to the damping in the direction of quasisymmetry. This information provides motivation for including the parallel flow in Shaing's model of nonlinear viscosity in the following chapter, rather than setting it to zero as is commonly done [1]. Section 3.1 introduces the momentum balance equations and defines the model that will be used in the calculations shown in this document. Section 3.2 introduces the Hamada coordinate system and, except for the viscosity terms, expands the momentum balance equations in this coordinate system. Section 3.3 then uses a linear viscosity model in Hamada coordinates, which allows the equations to be solved analytically. This section will show that the parallel flow is very weakly damped for the QHS configuration, but that the F14 and Mirror configuration have increasing levels of parallel flow damping. In Chapter 4, a nonlinear viscosity model in Hamada coordinates will be used along with the momentum balance equations to solve the effect of the parallel flow on the ion resonant electric field.

3.1 The Momentum Balance Equations

The evolution of the parallel mass flow and the radial electric field in a plasma composed of only hydrogen and electrons is calculated using the poloidal momentum balance equation [2]

$$M_i N_i \frac{\partial \langle \boldsymbol{B_p} \cdot \boldsymbol{V_i} \rangle}{\partial t} = -\langle \boldsymbol{B_p} \cdot \boldsymbol{\nabla} \cdot \boldsymbol{\pi} \rangle - M_i N_i \nu_{in} \langle \boldsymbol{B_p} \cdot \boldsymbol{V_i} \rangle - \frac{\sqrt{g} B^\theta B^\zeta}{c} \langle \boldsymbol{J_{plasma}} \cdot \boldsymbol{\nabla} \Psi \rangle \quad (3.1)$$

whose right-hand side terms correspond to poloidal viscosity, poloidal damping due to neutrals, and the radial plasma current. Other damping mechanisms, such as turbulence, are not considered in the calculations done in this work. Here, the subscript i denotes a given ion species, M_i is the ion mass, N_i is the number density, $\mathbf{B_p}$ is a vector in Hamada coordinates in the poloidal direction so that $\boldsymbol{B_p} \equiv B^\theta \boldsymbol{e_\theta}$, V is the mass flow velocity, t is time, $\langle \boldsymbol{B_p} \cdot \boldsymbol{\nabla} \cdot \boldsymbol{\pi} \rangle$ is the viscosity, ν_{in} is the neutral particle collision frequency, $\sqrt{g}$ is the Jacobian, c is the speed of light, J_{plasma} is the plasma current density, and B^θ and B^ζ are the contravariant components of the magnetic field in the θ and ζ directions respectively and e_θ is the covariant basis vector in the θ direction. This work will use Hamada coordinates [3] for HSX in evaluating the equations where the space is defined by the poloidal angle θ, the toroidal angle ζ, and the toroidal flux through a magnetic surface Ψ which acts as a radial coordinate. The angle brackets denote the flux surface average of the enclosed quantity. We use Hamada coordinates in this work in order to have a coordinate system in which the magnetic field and plasma flows are straight, unlike other

coordinate systems where only the field lines are straight. In Hamada coordinates , the Jacobian and contravariant components of both the plasma flows and magnetic fields are constant on a flux surface, which allows us to solve the equations analytically in Section 3.3.

Similar to Equation 3.1, the parallel momentum balance equation

$$M_i N_i \frac{\partial \langle \boldsymbol{B} \cdot \boldsymbol{V_i} \rangle}{\partial t} = -\langle \boldsymbol{B} \cdot \boldsymbol{\nabla} \cdot \boldsymbol{\pi} \rangle - M_i N_i \nu_{in} \langle \boldsymbol{B} \cdot \boldsymbol{V_i} \rangle \qquad (3.2)$$

has terms on the right-hand side corresponding to parallel viscosity and parallel damping due to neutrals. These equations neglect electron viscosity and are obtained by adding the momentum balance equations for ions and electrons, which cancels out the frictional force between the two [2].

By setting the left-hand sides of both equations equal to zero, the steady state values of the parallel flow and the electric field can be found for a given radial current. These calculations will be performed in Chapter 4 of this document. The radial current density can be related to an externally biased current density by the radial component of Ampere's law,

$$\frac{\partial}{\partial t}\frac{\partial \Phi}{\partial \Psi}\langle \boldsymbol{\nabla}\Psi \cdot \boldsymbol{\nabla}\Psi \rangle = 4\pi\left(\langle \boldsymbol{J_{plasma}} \cdot \boldsymbol{\nabla}\Psi \rangle + \langle \boldsymbol{J_{ext}} \cdot \boldsymbol{\nabla}\Psi \rangle\right) \qquad (3.3)$$

Here Φ is the plasma potential, $\frac{\partial \Phi}{\partial \Psi}$ is a flux surface constant, and J_{ext} is an externally driven current. It is clear that in steady state, the plasma current is equal to the external current, but as the plasma current rises to that value, an electric field is produced in the plasma. Ampere's law can be substituted into the poloidal momentum balance equation via the plasma current term:

$$M_i N_i \frac{\partial \langle \boldsymbol{B_p} \cdot \boldsymbol{V_i} \rangle}{\partial t} + \frac{\sqrt{g} B^\theta B^\zeta}{4\pi c} \frac{\partial}{\partial t} \frac{\partial \Phi}{\partial \Psi} \langle \nabla \Psi \cdot \nabla \Psi \rangle = -\langle \boldsymbol{B_p} \cdot \nabla \cdot \boldsymbol{\pi} \rangle -$$

$$M_i N_i \nu_{in} \langle \boldsymbol{B_p} \cdot \boldsymbol{V_i} \rangle + \frac{\sqrt{g} B^\theta B^\zeta}{c} \langle \boldsymbol{J_{ext}} \cdot \nabla \Psi \rangle \qquad (3.4)$$

By solving Equations 3.2 and 3.4 simultaneously, the radial electric field and parallel flow can be solved, with the external radial current used as an independent driving term.

3.2. Expansion of the momentum balance equations in Hamada coordinates

In a Hamada coordinate system we can write a vector **A** in terms of the covariant and contravariant basis vectors respectively as $\boldsymbol{A} = A^\psi \boldsymbol{e_\psi} + A^\theta \boldsymbol{e_\theta} + A^\zeta \boldsymbol{e_\zeta} = A^\psi \nabla \boldsymbol{\psi} + A^\theta \nabla \boldsymbol{\theta} + A^\zeta \nabla \boldsymbol{\zeta}$, where $e_i \cdot \nabla u^j = \delta_j^i$ The specific Hamada coordinate system in this thesis uses the toroidal flux ψ as the radial coordinate, while the poloidal coordinate θ and the toroidal coordinate ζ vary between 0 and 2π, as in [4] and the Jacobian, denoted by $\sqrt{g}$ is equal to $(1/4\pi^2)\, dV/d\psi$. In this coordinate system, the contravariant radial component of $B^\Psi \equiv \boldsymbol{B} \cdot \nabla \boldsymbol{\Psi} = V^\Psi = 0$ so that $\boldsymbol{B} = B^\theta \boldsymbol{e_\theta} + B^\zeta \boldsymbol{e_\zeta}$ and $\boldsymbol{V} = V^\theta \boldsymbol{e_\theta} + V^\zeta \boldsymbol{e_\zeta}$.

Since the contravariant components of the magnetic field and parallel flow are flux surface constants, they can be removed from flux surface averages. We can then write $\langle \boldsymbol{B} \cdot \boldsymbol{V} \rangle = \langle B_{\boldsymbol{\theta}} \rangle V^{\boldsymbol{\theta}} + \langle B_{\boldsymbol{\zeta}} \rangle V^{\boldsymbol{\zeta}}$. In this work we assume that the plasma current is zero. In reference [4] it was shown that $<B_{\boldsymbol{\theta}}>$ is proportional to the current within a flux surface; therefore this term is zero. The flux surface average of the covariant component of the field in the toroidal direction is then $\langle B_{\zeta} \rangle = \langle \boldsymbol{B} \cdot \boldsymbol{e_{\zeta}} \rangle = B^{\theta} \langle \boldsymbol{e_{\theta}} \cdot \boldsymbol{e_{\zeta}} \rangle + B^{\zeta} \langle \boldsymbol{e_{\zeta}} \cdot \boldsymbol{e_{\zeta}} \rangle$.Thus the term $\langle \boldsymbol{B} \cdot \boldsymbol{V} \rangle$ is given by

$$\langle \boldsymbol{B} \cdot \boldsymbol{V} \rangle = B^{\theta} V^{\zeta} \langle \boldsymbol{e_{\theta}} \cdot \boldsymbol{e_{\zeta}} \rangle + B^{\zeta} V^{\zeta} \langle \boldsymbol{e_{\zeta}} \cdot \boldsymbol{e_{\zeta}} \rangle \qquad (3.5)$$

Similarly, $\langle \boldsymbol{B_p} \cdot \boldsymbol{V} \rangle = \langle \boldsymbol{V_{\theta}} \rangle \boldsymbol{B^{\theta}}$ and since$\langle V_{\theta} \rangle = V^{\theta} \langle \boldsymbol{e_{\theta}} \cdot \boldsymbol{e_{\zeta}} \rangle + V^{\zeta} \langle \boldsymbol{e_{\zeta}} \cdot \boldsymbol{e_{\zeta}} \rangle$

$$\langle \boldsymbol{B_P} \cdot \boldsymbol{V} \rangle = B^{\theta} V^{\theta} \langle \boldsymbol{e_{\theta}} \cdot \boldsymbol{e_{\theta}} \rangle + B^{\theta} V^{\zeta} \langle \boldsymbol{e_{\theta}} \cdot \boldsymbol{e_{\zeta}} \rangle \qquad (3.6)$$

For this thesis, the numerically computed contravariant components of the magnetic field and the flux surface average of the basis vectors are used as given in Reference [4].

The contravariant components of the flow are given in Equations 23a and 23b of Reference [2] as

$$V^{\theta} = c \left(\frac{p'}{eN} + \frac{\boldsymbol{d\Phi}}{\boldsymbol{d\Psi}} \right) \left(\frac{1}{B^{\zeta} \sqrt{g}} \right) + \lambda B^{\theta} \qquad (3.7)$$

and

$$V^{\zeta} = \lambda B^{\zeta} \qquad (3.8)$$

Here, e is the elementary charge, p' is the ion pressure gradient, c is the speed of light, λ is a flux surface constant such that the flux surface averaged parallel mass flow $V_{\|} = \lambda B$. In this document, all calculations for the two unknowns λ and $\frac{d\Phi}{d\Psi}$ are performed in cgs units and then converted to $V_{\|}$ in km/s and E_r in kV/m. The following relationships are used for the conversions: $V_{\|} = \lambda B_0(\text{gauss})/10^5$ and $E_r = -60\frac{\partial\Phi}{\partial\Psi}\sqrt{\pi\psi B_0}$ where the toroidal flux $\psi = \pi r^2 B_0$ and r is the minor radius. For the remainder of this document, when discussing the calculation of E_r or $V_{\|}$ using the momentum balance equations, we refer to the conversions from $\frac{d\Phi}{d\Psi}$ or λ respectively.

The assumption is made that the terms $\frac{d\Phi}{d\Psi}$ and λ evolve on a time-scale faster than that of the plasma density and pressure gradient. Therefore,

$$\frac{\partial\langle \boldsymbol{B}\cdot\boldsymbol{V}\rangle}{\partial t} = \frac{\partial\lambda}{\partial t}B^{\zeta}\left(B^{\theta}\langle \boldsymbol{e_\theta}\cdot\boldsymbol{e_\zeta}\rangle + B^{\zeta}\langle \boldsymbol{e_\zeta}\cdot\boldsymbol{e_\zeta}\rangle\right) \tag{3.9}$$

Since the term in parenthesis is equal to $\langle B_\zeta\rangle$ and $\langle B^2\rangle = \langle \boldsymbol{B}\cdot\boldsymbol{B}\rangle = B^{\theta}\langle B_\theta\rangle + B^{\zeta}\langle B_\zeta\rangle = B^{\zeta}\langle B_\zeta\rangle$ (again, because $\langle B_\theta\rangle = 0$), this equation can be written more succinctly as

$$\frac{\partial\langle \boldsymbol{B}\cdot\boldsymbol{V}\rangle}{\partial t} = \frac{\partial\lambda}{\partial t}\langle B^2\rangle \tag{3.10}$$

For the poloidal component of the momentum balance equation, the time derivative term can be written as

$$\frac{\partial\langle \boldsymbol{B_P}\cdot V_i\rangle}{\partial t} = B^{\theta}\langle \boldsymbol{e_\theta}\cdot\boldsymbol{e_\theta}\rangle\frac{\partial V^{\theta}}{\partial t} + B^{\theta}\langle \boldsymbol{e_\theta}\cdot\boldsymbol{e_\zeta}\rangle\frac{\partial V^{\zeta}}{\partial t} \tag{3.11}$$

So that inserting Equations 3.7 and 3.8 it becomes,

$$\frac{\partial\langle \boldsymbol{B_p}\cdot\boldsymbol{V}\rangle}{\partial \boldsymbol{t}} = \frac{\partial}{\partial \boldsymbol{t}}\frac{\partial \boldsymbol{\Phi}}{\partial \boldsymbol{\Psi}}\frac{cB^{\theta}}{B^{\zeta}\sqrt{g}}\langle \boldsymbol{e_\theta}\cdot\boldsymbol{e_\theta}\rangle + \frac{\partial\lambda}{\partial t}B^{\theta}\left(B^{\theta}\langle \boldsymbol{e_\theta}\cdot\boldsymbol{e_\theta}\rangle + B^{\zeta}\langle \boldsymbol{e_\theta}\cdot\boldsymbol{e_\zeta}\rangle\right) \quad (3.12)$$

We can further reduce Equation 3.12 by recognizing that $B^{\theta}\langle \boldsymbol{e_\theta}\cdot\boldsymbol{e_\theta}\rangle + B^{\zeta}\langle \boldsymbol{e_\zeta}\cdot\boldsymbol{e_\theta}\rangle = \langle B_\theta\rangle = 0$ so that the coefficient multiplying $\frac{\partial\lambda}{\partial t}$ is zero. In this case,

$$\frac{\partial\langle \boldsymbol{B_p}\cdot\boldsymbol{V_i}\rangle}{\partial \boldsymbol{t}} = \frac{\partial}{\partial \boldsymbol{t}}\frac{\partial \boldsymbol{\Phi}}{\partial \boldsymbol{\Psi}}\frac{cB^{\theta}}{B^{\zeta}\sqrt{g}}\langle \boldsymbol{e_\theta}\cdot\boldsymbol{e_\theta}\rangle = \frac{\partial}{\partial \boldsymbol{t}}\frac{\partial \boldsymbol{\Phi}}{\partial \boldsymbol{\Psi}}\frac{c\langle B_p^2\rangle}{B^{\theta}B^{\zeta}\sqrt{g}} \quad (3.13)$$

where $\langle B_p^2\rangle = \langle \boldsymbol{B_p}\cdot\boldsymbol{B_p}\rangle = B^{\theta}B^{\theta}\langle \boldsymbol{e_\theta}\cdot\boldsymbol{e_\theta}\rangle$.

Applying Equation 3.5 to the neutral damping in the parallel direction:

$$M_i N_i \nu_{in}\langle \boldsymbol{B}\cdot\boldsymbol{V_i}\rangle = M_i N_i \nu_{in}\left(B^{\theta}V^{\zeta}\langle \boldsymbol{e_\theta}\cdot\boldsymbol{e_\zeta}\rangle + B^{\zeta}V^{\zeta}\langle \boldsymbol{e_\zeta}\cdot\boldsymbol{e_\zeta}\rangle\right) \quad (3.14)$$

Similarly for the poloidal neutral damping, we apply Equation 3.6:

$$M_i N_i \nu_{in}\langle \boldsymbol{B_P}\cdot\boldsymbol{V_i}\rangle = M_i N_i \nu_{in}\left(B^{\theta}V^{\theta}\langle \boldsymbol{e_\theta}\cdot\boldsymbol{e_\theta}\rangle + B^{\theta}V^{\zeta}\langle \boldsymbol{e_\theta}\cdot\boldsymbol{e_\zeta}\rangle\right) \quad (3.15)$$

This model of neutral damping will be used in the calculations presented in the remainder of this document. Substituting the equations from this section into Equation 3.2 the parallel momentum balance equation becomes:

$$M_i N_i \frac{\partial \lambda}{\partial t}\langle B^2 \rangle = \tag{3.16}$$

$$-\langle \boldsymbol{B} \cdot \boldsymbol{\nabla} \cdot \boldsymbol{\pi} \rangle - M_i N_i v_{in}\left(B^{\theta}\lambda B^{\zeta}\langle \boldsymbol{e_{\theta}} \cdot \boldsymbol{e_{\zeta}} \rangle + B^{\zeta}\lambda B^{\zeta}\langle \boldsymbol{e_{\zeta}} \cdot \boldsymbol{e_{\zeta}} \rangle\right)$$

While it appears that the parallel momentum balance equation is only dependent on λ, there is coupling between λ and $\frac{d\Phi}{d\psi}$ within the viscosity term. Similarly substituting into Equation 3.4 the poloidal momentum balance equation becomes:

$$\frac{\boldsymbol{\partial}}{\boldsymbol{\partial t}}\frac{\boldsymbol{\partial \Phi}}{\boldsymbol{\partial \Psi}}\left(M_i N_i \frac{c\langle B_p^2 \rangle}{B^{\theta}B^{\zeta}\sqrt{g}} + \frac{\sqrt{g}B^{\theta}B^{\zeta}}{4\pi c}\langle \boldsymbol{\nabla}\Psi \cdot \boldsymbol{\nabla}\Psi \rangle\right) \tag{3.17}$$

$$= -\left\langle \boldsymbol{B_p} \cdot \boldsymbol{\nabla} \cdot \boldsymbol{\pi} \right\rangle + \frac{\sqrt{g}B^{\theta}B^{\zeta}}{c}\langle \boldsymbol{J_{ext}} \cdot \boldsymbol{\nabla}\Psi \rangle$$

$$- M_i N_i v_{in}\left(B^{\theta}\left(c\left(\frac{p'}{eN} + \frac{\boldsymbol{\partial \Phi}}{\boldsymbol{\partial \Psi}}\right)\left(\frac{1}{B^{\zeta}\sqrt{g}}\right) + \lambda B^{\theta}\right)\langle \boldsymbol{e_{\theta}} \cdot \boldsymbol{e_{\theta}} \rangle\right.$$

$$\left. + B^{\theta}\lambda B^{\zeta}\langle \boldsymbol{e_{\theta}} \cdot \boldsymbol{e_{\zeta}} \rangle\right)$$

Linear viscosity for these equations will be discussed in the next section, while nonlinear viscosity will be presented in Chapter 4.

3.3 Application of Linear Viscosity

In this section, we apply the analytic linear viscosity model for ions to in the plateau regime [5] where the parallel viscosity is:

$$\langle \boldsymbol{B} \cdot \boldsymbol{\nabla} \cdot \boldsymbol{\pi} \rangle = \boldsymbol{\mu_\theta V^\theta} + \boldsymbol{\mu_\zeta V^\zeta} \tag{3.18}$$

Where $\mu_\theta = \kappa\left(B^\theta \alpha_P + B^\zeta \alpha_C\right)$, $\mu_\zeta = \kappa\left(B^\theta \alpha_C + B^\zeta \alpha_T\right)$, and V^θ and V^ζ are the contravariant components of parallel mass flow velocities in the θ and ζ directions respectively. In these expressions: $\kappa = \pi^{1/2} P B_0 / V_{ta} B^\zeta$, $\alpha_T = \frac{\Sigma n^2 \varepsilon_{n,m}}{|n - m\iota|}$, $\alpha_P = \frac{\Sigma m^2 \varepsilon_{n,m}}{|n - m\iota|}$, and $\alpha_C = \frac{\Sigma nm \varepsilon_{n,m}}{|n - m\iota|}$. Where P is the pressure, B_0 is the magnetic field strength, V_{ta} is the ion thermal velocity, ι is the rotational transform, n and m are the magnetic mode numbers, and $\varepsilon_{n,m}$ is the magnetic mode amplitude of mode (n,m).

Similarly for the poloidal viscosity:

$$\left\langle \boldsymbol{B_p} \cdot \boldsymbol{\nabla} \cdot \boldsymbol{\pi} \right\rangle = \boldsymbol{\mu_\theta}^{\boldsymbol{P}} \boldsymbol{U^\theta} + \boldsymbol{\mu_\zeta}^{\boldsymbol{P}} \boldsymbol{U^\zeta} \tag{3.19}$$

Where and $\mu_\theta{}^P = \kappa B^\theta \alpha_P$ and $\mu_\zeta{}^P = \kappa B^\theta \alpha_C$.

Using Equations 3.18 and 3.19 as the models for viscosity, they can be inserted into Equations 3.16 and 3.17 respectively. The result is two coupled ordinary differential equations in the matrix form:

$$A \frac{dX}{dt} + BX = C \tag{3.20}$$

where $X = [\frac{\partial \boldsymbol{\Phi}}{\partial \boldsymbol{\Psi}} ; \lambda]$.

Using the Hamada basis vectors calculated in [4] instead of making approximations to cylindrical coordinates or a large aspect ratio tokamak [6], the coefficients A and B in Equation 3.20 are matrices that depend on flux surface constants independent of E_r and $V_\parallel$ and thus are time independent. However, the term C contains the external current which we vary with time.

In this section, we assume a square wave behavior where $J_{ext}=0$ at $t=t_0$ and is a constant at $t>t_0$. Because we use a linear model of viscosity as well as Hamada coordinates, the differential equations can be solved analytically for $\frac{\partial \Phi}{\partial \Psi}$ and λ. With this framework, the solution to Equation 3.20 for the parallel flow and radial electric field becomes the sum of two exponentials as given in Equations 67a and 67b in reference [2]:

$$\frac{\partial \Phi}{\partial \Psi} = k_1\left(1 - e^{\gamma_s(t-t_0)}\right) + k_2\left(1 - e^{\gamma_f(t-t_0)}\right) + k_3 \qquad (3.21)$$

$$\lambda = k_4\left(1 - e^{\gamma_s(t-t_0)}\right) + k_5\left(1 - e^{\gamma_f(t-t_0)}\right) \qquad (3.22)$$

Where γ_s and γ_f are the eigenvalues of Equation 3.20. They are both negative and correspond to the slow and fast damping given in Equation 60 of reference [2], which themselves correspond to the direction of quasisymmetry for the slow damping time and the orthogonal direction for the fast damping time. The constant k_3 is the initial steady state value of $\frac{\partial \Phi}{\partial \Psi}$ while the final steady state value is $\frac{\partial \Phi}{\partial \Psi}_{SS} = \boldsymbol{k_1 + k_2 + k_3}$. Similarly, the final steady state value for the parallel flow is $\lambda = k_4 + k_5$ as the initial value of the parallel flow is assumed to be zero.

Equations 3.21 and 3.22 can be solved to determine the contributions of each timescale to the evolution of E_r and $V_{\|}$.

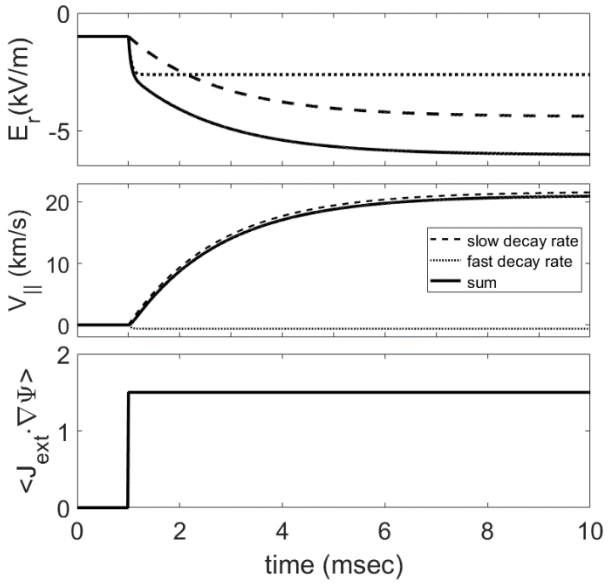

Figure 3.1 the time evolution of the radial electric field (top) and the parallel flow (middle) due to the rise in the external current (bottom). The individual contributions from the fast and slow time scales are shown by the dotted and dashed lines respectively with the total evolution shown by the solid line *[7]*.

As seen in Figure 3.1, the simulated external bias electrode at the position of r/a=0.7 draws current at t_0=1ms until the simulation ends at 10ms. As can be seen clearly in the figure, $V_{||}$ is almost completely dominated by the slow timescale with the tiny contribution from the fast timescale actually being negative. Meanwhile, the time evolution of E_r is determined by a more balanced mix of the fast and slow timescales but ends up having the majority of its rise from the slow timescale.

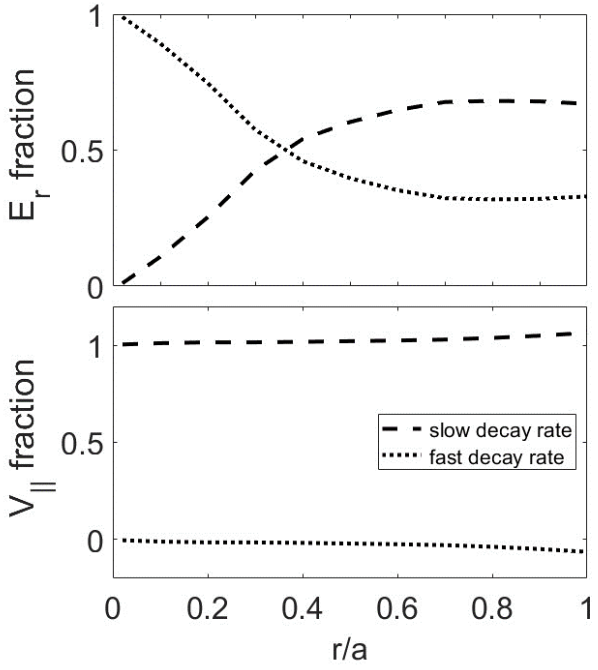

Figure 3.2 The steady state fractional contributions of the fast and slow timescales to the evolutions of E_r (top) and $V_{\|}$ (bottom) as a function of the normalized minor radius *[7]*.

Figure 3.2 shows the fractional dominance of each timescale for the evolution of both E_r and $V_{\|}$ as a function of the plasma radius. As can be seen, the slow timescale dominates the time evolution of the parallel flow throughout the plasma. However, the characteristics of the radial electric field's evolution change depending on the location. Close to the core, the contribution from the slow timescale is negligible while on the edge, it rises to roughly double that of the fast timescale's contribution.

Having shown that E_r and $V_{\|}$ rise in the presence of an external current and that $V_{\|}$ is completely dominated by the slow timescale, it can now be shown that the magnitude of both E_r and $V_{\|}$ can be altered by varying the damping mechanisms in the momentum balance equations. This is done either by changing the magnetic configuration of HSX, which alters the viscosity, or

changing the neutral density. By changing the magnetic configuration of HSX, the magnetic mode numbers change, as seen in Figure 2.3. The viscosity is then recalculated using Equations 3.16 and 3.17 and the momentum balance equations are once again solved for the time evolution of E_r and $V_{||}$.

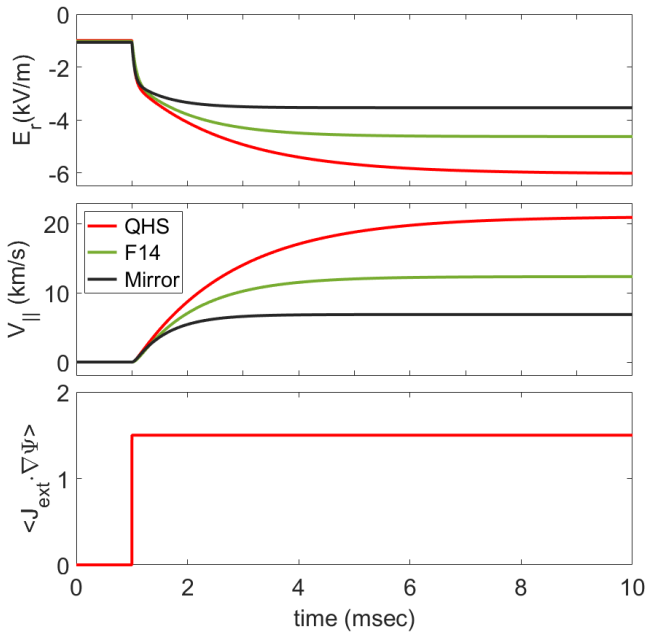

Figure 3.3 The time evolutions of both E_r (top) and $V_{||}$ (middle) as a function of the external current (bottom). The evolutions for HSX's three configurations QHS (red), F14 (green) and Mirror (black) are shown.

Figure 3.3 The time evolutions of both E_r (top) and $V_{||}$ (middle) as a function of the external current (bottom). The evolutions for HSX's three configurations QHS (red), F14 (green) and Mirror (black) are shown. shows the effects of the different configurations on the evolutions of E_r and $V_{||}$. For $V_{||}$ the slow damping mechanism dominates in all three cases, although the increased damping in F14 and Mirror configuration means that a lower steady state value is reached than QHS for the same external current. This clearly shows that the QHS configuration leads to the parallel flow being weakly damped by viscosity and being able to increase to the

order of the ion thermal speed (~60km/s) with the drive of the external current. The time evolution of E_r, on the other hand, shows that the fast damping mechanism is not affected very much by the increased viscosity in different configurations. The contribution of the fast timescale is seen to be very similar in all three cases, with the difference in the final value of E_r determined by the slow timescale contribution.

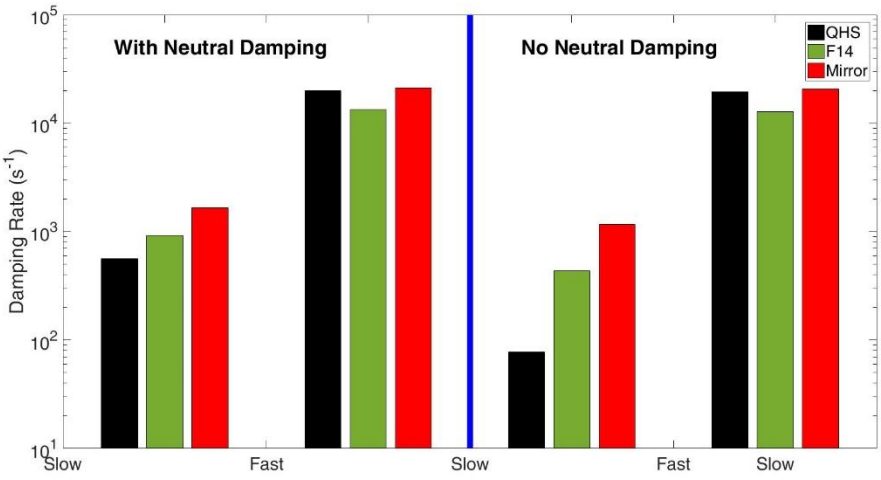

Figure 3.4 Comparison of the absolute values of the fast and slow damping rates in the QHS (black), F14 (green), and mirror (red) configurations of HSX, with (left) and without (right) neutral damping *[7]*.

Figure 3.4 summarizes the relative values of the fast and slow damping rates for the three configurations of HSX. Their values with and without neutral damping can be compared. It can be clearly seen that the fast timescale remains relatively constant to changes in damping, be they due to changes in neutral density or viscosity.

From Reference [2] the total fast and slow damping rates are the sum of the ion neutral damping rate and the slow or fast viscous damping rates. For the QHS configuration, the neutral damping rate is $487s^{-1}$ and the slow damping rate is $78s^{-1}$ so the total rate is $565s^{-1}$ [2]. From these numbers, it is clear that the total slow damping rate is dominated by the neutral damping. Thus,

the parallel flow for the QHS configuration is especially sensitive to changes in the neutral density, while the radial electric field may not be, depending on the location in the plasma.

In the next chapter Shaing's nonlinear model of viscosity is introduced and steady-state momentum balance equations for the parallel flow and the radial electric field are solved numerically for varying values of $\langle \boldsymbol{J}_{\boldsymbol{ext}} \cdot \boldsymbol{\nabla}\Psi \rangle$.

References

[1] K. C. Shaing, "Test of tokamak low-mode-high-mode transition theory in stellarators," *Physics of Fluids B: Plasma Physics,* vol. 5, no. 11, p. 3841, 1993.

[2] M. Coronado and J. N. Talmadge, "Evolution of the plasma rotation and the radial electric field for a toroidal plasma in the Pfirsch-Schluter and plateau regimes subject to a biased electrode," *Physics of Plasmas,* vol. 5, no. 4, p. 1200, 1993.

[3] S. Hamada, "Hydromagnetic equilibria and their proper coordinates," *Nuclear Fusion,* vol. 2, p. 23, 1962.

[4] J. N. Talmadge and S. Gerhardt, "Numerical calculation of the Hamada basis vectors for three-dimensional toroidal magnetic configurations," *Physics of Plasmas,* vol. 12, no. 7, p. 072513, 2005.

[5] K. C. Shaing, S. P. Hirshman and J. D. Callen, "Plasma transport coefficients for nonsymmetric toroidal confinement systems," *Physics of Fluids,* vol. 29, no. 9, 1986.

[6] M. Coronado and J. Galindo Trejo, "Calculation of Hamada coordiantes for a large-aspect-ratio tokamak," *Physics of Fluids B: Plasma Physics,* vol. 2, no. 3, p. 530, 1990.

[7] J. N. Talmadge, *Personal Communication,* 2023.

---4---

Nonlinear Viscosity and Steady State Solutions to the Momentum Balance Equations

The effect of the parallel flow on the resonant electric field, as discussed in this chapter is based on Shaing's nonlinear viscosity model [1] as applied to HSX. As Shaing's model was originally constructed to explain L-H transitions, it will be applied to the momentum balance equations presented in Chapter 3, in place of the linear viscosity model used in that chapter. A derivation of the poloidal and toroidal viscosities is presented in Section 4.1. The general form of the resonant electric field that includes the parallel flow is given in Section 4.2. This will be shown to reduce to the more widely known form of the poloidal Mach number given by Shaing when using a large aspect ratio tokamak approximation for the Hamada coordinates and assuming that the parallel flow is zero. The nonlinear poloidal viscosity is calculated and plotted in Section 4.3 with varying parallel velocities to show that the inclusion of parallel velocity shifts the resonant electric field. The steady-state momentum balance equations are solved in Section 4.4 for the radial electric field and the parallel velocity as a function of an externally driven torque. These steady-state values show that by varying the neutral or viscous damping the parallel flow can be altered, thereby modifying the resonant electric field value in a controlled manner. Finally, Section 4.5 shows that the resonant electric field in a tokamak shifts less for a given parallel velocity than in a QHS configuration.

4.1 Calculation of the Viscosity in the Shaing Model

The poloidal and toroidal viscosities are calculated with the linearized Drift Kinetic Equation (DKE) with plasma flows:

$$[(v_{\|} + V_{\|})\hat{\boldsymbol{n}} + \boldsymbol{V_E}] \cdot \boldsymbol{\nabla} f - C(f) = \tag{4.1}$$

$$2\left(\frac{v^2}{v_t^2}\right)\left(\frac{1}{2} - \frac{3v_{\|}^2}{2v^2}\right) f_M \left[\boldsymbol{V} \cdot \boldsymbol{\nabla} \ln(B) - L_1^{3/2} \frac{2}{5p}(\boldsymbol{q} \cdot \boldsymbol{\nabla} \ln(B))\right]$$

Here bold characters indicate vector quantities, $v_{\|}$ is the particle velocity parallel to the magnetic field, $V_{\|}$ is the mass flow velocity in that direction, $\boldsymbol{V_E}$ is the ExB drift velocity, f is the perturbed particle distribution function, f_M is the Maxwellian particle distribution function, C is the Coulomb collision operator, v is the particle velocity, v_t is the thermal velocity, $\boldsymbol{V}$ is the mass flow velocity, B is the magnetic field strength, p is the plasma pressure, $\boldsymbol{q}$ is the heat flux, and

$$L_1^{3/2} = 2.5 - \frac{v^2}{v_t^2} \tag{4.2}$$

To simplify the calculation, Shaing uses a Krook collision operator, C $= -f * \nu_K$, where ν_K is defined as [2]

$$\nu_K = \frac{3\sqrt{\pi}}{4} \sum_{a,b} \frac{1}{\tau_{ab}} \left[\frac{\Phi\left(\frac{x_a}{x_{ab}}\right) - 3G\left(\frac{x_a}{x_{ab}}\right)}{x_a^3} + 4\frac{G\left(\frac{x_a}{x_{ab}}\right)}{x_a}\left(\frac{T_a}{T_b} + \frac{1}{x_{ab}^2}\right)\right] \tag{4.3}$$

where a and b denote the particle species, T is the temperature and

$$x_{ab} = \frac{v_{tb}}{v_{ta}},\ x_a = \frac{v}{v_{ta}} \tag{4.4}$$

$$G\left(\frac{x_a}{x_{ab}}\right) = \frac{\left[\Phi\left(\frac{x_a}{x_{ab}}\right) - \frac{x_a}{x_{ab}}\Phi'\right]}{2\left(\frac{x_a}{x_{ab}}\right)^2} \tag{4.5}$$

Here Φ is the error function and

$$\Phi'\left(\frac{x_a}{x_{ab}}\right) = 2\sqrt{\frac{x_a}{\pi x_{ab}}}e^{-\frac{x_a}{x_{ab}}} \tag{4.6}$$

In Equation 4.3, τ_{ab} is the collision time between species a and b defined as:

$$\frac{1}{\tau_{ab}} = \frac{16\sqrt{\pi}}{3}\frac{N_b e_a^2 e_b^2 ln(\Lambda)}{M_a^2 v_{Ta}^2} \tag{4.7}$$

where e denotes the charge of the species, M is the mass, N is the particle density, v_T is the thermal velocity, and ln(Λ) is the Coulomb Logarithm:

$$\ln(\Lambda) = 23 - ln\left(Z\sqrt{\frac{2N}{T^3}}\right) \tag{4.8}$$

where Z is the ion charge and T is the ion temperature. The Hamada coordinates used by Shaing are the volume V, the poloidal angle θ, and the toroidal angle ζ. For this set of Hamada coordinates, the poloidal and toroidal angles vary between 0 and 1 so that the Jacobian is equal to one. When solving the momentum balance equations, the coordinate system discussed in Chapter 3 will be used.

Because the magnetic field spectrum is a summation of cosine terms corresponding to different magnetic mode numbers m and n as seen in Equation 2.1 we assume the perturbed distribution function will be of the form:

$$f = \sum_{m,n} f_{1mn} \sin(m\theta - n\zeta) + \sum_{m,n} f_{2mn} \cos(m\theta - n\zeta) \quad (4.9)$$

With this assumption, Equation 4.1 can then be solved for the perturbed distribution function:

$$f = 2\left(\frac{v^2}{v_t^2}\right)\left(\frac{1}{2} - \frac{3v_\parallel^2}{2v^2}\right) f_M \cdot \quad (4.10)$$

$$\left\{ \left(\boldsymbol{V} \cdot \boldsymbol{\nabla}\theta - L_1^{3/2} \frac{2\boldsymbol{q}}{5p} \cdot \boldsymbol{\nabla}\theta \right) \cdot \left[\sum_{m,n} -m * \varepsilon_{mn} (R_{mn} \sin(m\theta - n\zeta) + S_{mn} \cos(m\theta - n\zeta)) \right] + \right.$$
$$\left. \left(\boldsymbol{V} \cdot \boldsymbol{\nabla}\zeta - L_1^{3/2} \frac{2\boldsymbol{q}}{5p} \cdot \boldsymbol{\nabla}\zeta \right) \cdot \left[\sum_{m,n} n * \varepsilon_{mn} (R_{mn} \sin(m\theta - n\zeta) + S_{mn} \cos(m\theta - n\zeta)) \right] \right\}$$

Here, f_M is the Maxwellian distribution function, ε_{mn} is the magnetic mode amplitude, and

$$R_{mn} = \left[\frac{\nu_\kappa}{\left(m\omega_\theta - n\omega_\zeta\right)^2 + \nu_\kappa^2}\right] \tag{4.11}$$

$$S_{mn} = \left[\frac{\left(m\omega_\theta - n\omega_\zeta\right)}{\left(m\omega_\theta - n\omega_\zeta\right)^2 + \nu_\kappa^2}\right] \tag{4.12}$$

where

$$\omega_\theta = \left(\frac{v_\parallel + V_\parallel}{|B|}\right)\boldsymbol{B}\cdot\boldsymbol{\nabla}\theta + \boldsymbol{V_E}\cdot\boldsymbol{\nabla}\theta \tag{4.13}$$

$$\omega_\zeta = \left(\frac{v_\parallel + V_\parallel}{|B|}\right)\boldsymbol{B}\cdot\boldsymbol{\nabla}\zeta + \boldsymbol{V_E}\cdot\boldsymbol{\nabla}\zeta \tag{4.14}$$

The poloidal and toroidal viscosities may be calculated using the perturbed distribution function. The poloidal viscosity is defined as

$$\langle \boldsymbol{B_p}\cdot\boldsymbol{\nabla}\cdot\boldsymbol{\pi}\rangle = \langle \int M\left[\frac{v^2}{2} - \frac{3v_\parallel^2}{2}\right]\cdot\frac{f\boldsymbol{B_p}\cdot\boldsymbol{\nabla}B}{B}d^3v\rangle \tag{4.15}$$

where M is the particle mass and $\boldsymbol{B_p}$ is defined as:

$$\boldsymbol{B_p} = B^{\theta}\boldsymbol{e_\theta} \tag{4.16}$$

where $\boldsymbol{e_\theta}$ is the covariant basis vector and B^{θ} is the contravariant component of the magnetic field, both in the θ direction. The angled brackets in Equation 4.15 denote a flux surface average. Similarly, the toroidal viscosity is defined as

$$\langle \boldsymbol{B_t} \cdot \boldsymbol{\nabla} \cdot \boldsymbol{\pi} \rangle = \langle \int M \left[\frac{v^2}{2} - \frac{3v_{\|}^2}{2} \right] \cdot \frac{f \boldsymbol{B_t} \cdot \boldsymbol{\nabla} B}{B} d^3 v \rangle \tag{4.17}$$

where $\boldsymbol{B_t}$ is defined as:

$$\boldsymbol{B_t} = B^{\zeta}\boldsymbol{e_\zeta} \tag{4.18}$$

The total vector form of the magnetic field can be written as:

$$\boldsymbol{B} = B^{\zeta}\boldsymbol{e_\zeta} + B^{\theta}\boldsymbol{e_\theta} + B^{V}\boldsymbol{e_V} \tag{4.19}$$

The B^{V} term in Equation 4.19 is zero for any toroidal device. This is because there is no component of the magnetic field that is perpendicular to magnetic flux surfaces. Thus, the parallel viscosity can be calculated as:

$$\langle \boldsymbol{B} \cdot \boldsymbol{\nabla} \cdot \boldsymbol{\pi} \rangle = \langle \boldsymbol{B_t} \cdot \boldsymbol{\nabla} \cdot \boldsymbol{\pi} \rangle + \langle \boldsymbol{B_p} \cdot \boldsymbol{\nabla} \cdot \boldsymbol{\pi} \rangle \tag{4.20}$$

For Equations 4.15 and 4.17, the integral is performed over all velocity space using spherical coordinates:

$$\int d^3v = \iiint v^2 \sin(\mu)\, d\mu d\varphi dv \tag{4.21}$$

where φ and μ are the polar and azimuthal angles respectively in a spherical coordinate system. Figure 4.1 shows a spherical coordinate system where the angles (r,θ,φ) in the figure correspond to (v,μ,φ) in the integral.

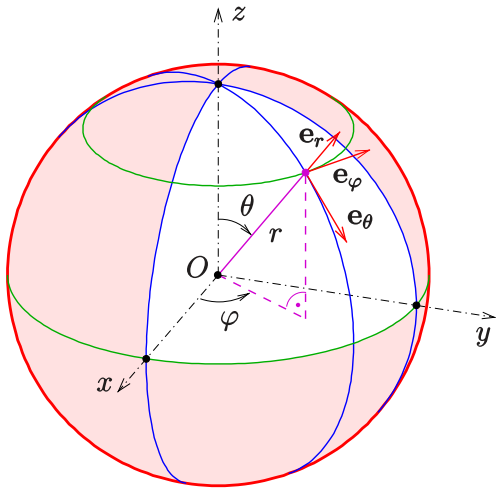

Figure 4.1 An illustration of spherical coordinates (r,θ,φ) corresponding to radial position, azimuthal angle, and polar angle respectively. *[3]*

To solve this integral, we perform variable substitutions:

$$x = \frac{v^2}{v_{th}^2} \tag{4.22}$$

and

$$y = \frac{v_{\|}}{v} = \cos(\mu) \tag{4.23}$$

This allows us to combine Equations 4.10 and 4.15 to solve for poloidal viscosity as the following expression:

$$\langle \boldsymbol{B_p} \cdot \boldsymbol{\nabla} \cdot \boldsymbol{\pi} \rangle = \frac{v_{th} NMB}{4\pi^{1/2}} \sum_{m,n} m\varepsilon_{mn}{}^2 \iint x^2 e^{-x} (1 - 3y^2)^2 \cdot R_{mn} \frac{B^\theta}{B} \left\{ (m\boldsymbol{V} \cdot \boldsymbol{\nabla}\theta - n\boldsymbol{V} \cdot \boldsymbol{\nabla}\zeta) + \left(n\left(\frac{5}{2} - x\right)\frac{2\boldsymbol{q}}{5p} \cdot \boldsymbol{\nabla}\zeta - m\left(\frac{5}{2} - x\right)\frac{2\boldsymbol{q}}{5p} \cdot \boldsymbol{\nabla}\theta \right) \right\} v dx dy \tag{4.24}$$

The expression for viscosity is not dependent on the S_{mn} term. When the S_{mn} terms are multiplied by the $\boldsymbol{B_p} \cdot \boldsymbol{\nabla B}$ term in Equation 4.17 the terms include a sine multiplied by a cosine, which disappear upon taking the flux surface average of the expression. Similarly, Equations 4.10 and 4.17 are combined to solve for the toroidal viscosity as

$$\langle \boldsymbol{B_t} \cdot \boldsymbol{\nabla} \cdot \boldsymbol{\pi} \rangle = \frac{v_{th} NMB}{4\pi^{1/2}} \sum_{m,n} -n\varepsilon_{mn}{}^2 \iint x^2 e^{-x} (1 - 3y^2)^2 \cdot R_{mn} \left\{ (m\boldsymbol{V} \cdot \boldsymbol{\nabla}\theta - n\boldsymbol{V} \cdot \boldsymbol{\nabla}\zeta) + \left(n\left(\frac{5}{2} - x\right)\frac{2\boldsymbol{q}}{5p} \cdot \nabla\zeta - m\left(\frac{5}{2} - x\right)\frac{2\boldsymbol{q}}{5p} \cdot \boldsymbol{\nabla}\theta \right) \right\} v dx dy \tag{4.25}$$

4.2 Determining the Resonant Electric Field

In HSX, there is very low ion heat flux due to the small ion temperature gradient, so for the purpose of this work we stipulate, $\boldsymbol{q} = 0$. Repeating Equations 3.7 and 3.8 that are based on Reference [4]:

$$\boldsymbol{V} \cdot \boldsymbol{\nabla}\theta = c\left(\frac{p'}{eN} + \Phi'\right)\left(\frac{1}{B^{\zeta}\sqrt{g}}\right) + \lambda_a B^{\theta} \tag{4.26}$$

and

$$\boldsymbol{V} \cdot \boldsymbol{\nabla}\zeta = \lambda_a B^{\zeta} \tag{4.27}$$

where λ_a is a flux surface constant defined so that $\lambda_a * B$ is equal to the flux surface averaged parallel flow, $\sqrt{g}$ is the coordinate Jacobian, B^{ζ} and B^{θ} are the contravariant magnetic field components in the ζ and θ directions respectively, e is the elementary charge, p' is the ion

pressure gradient, c is the speed of light, and Φ' is the derivative of the electric potential with respect to the volume defined as

$$\Phi' = \frac{\partial \Phi}{\partial V} \tag{4.28}$$

The resonance occurs in the viscosity when the denominator in the R_{mn} term defined in Equation 4.11 is minimized. More specifically, the resonant electric field occurs when

$$m\omega_\theta = n\omega_\zeta \tag{4.29}$$

Using the definitions of ω_θ and ω_ζ found in Equations 4.13 and 4.14 respectively, the resonant electric field may be solved for by isolating the ExB terms, that is, those including Φ', in Equations 4.26 and 4.27 to get

$$\boldsymbol{V_E} \cdot \boldsymbol{\nabla}\theta = c\frac{\Phi'}{B^\zeta \sqrt{g}} \tag{4.30}$$

and

$$\boldsymbol{V_E} \cdot \boldsymbol{\nabla}\zeta = 0 \tag{4.31}$$

Equation 4.29 can then be rearranged as:

$$c\Phi' = -\frac{m-nq}{m}\frac{q(B^{\theta})^2}{B}(v_{\parallel} + V_{\parallel})\sqrt{g} \tag{4.32}$$

For the coordinate system used by Shaing, the angle coordinates θ and ζ are both defined to be between zero and one so that the Jacobian is equal to 1. In addition, $V_{\parallel}$ was assumed to be 0 and $v_{\parallel}$ was assumed to be on the order of the thermal velocity. Shaing then uses a large aspect ratio tokamak approximation [5] to convert from Hamada coordinates to cylindrical coordinates. The contravariant component of B in the poloidal direction is a flux surface quantity and is calculated as:

$$B^{\theta} = \frac{B_0}{2\pi Rq} \tag{4.33}$$

where B_0 is the magnetic field on the magnetic axis and R is the major radius of the toroidal system. The definition of q is:

$$q = \frac{r\boldsymbol{B_t}}{R\boldsymbol{B_p}} \tag{4.34}$$

where r is the minor radius of the system. Converting Φ' to the radial electric field, we also define

$$E_r = -\frac{\partial \Phi}{\partial r} = -\frac{\partial \Phi}{\partial V}4\pi^2 Rr \tag{4.35}$$

With these definitions and assumptions, Equation 4.32 can be rewritten as

$$c\frac{\partial \Phi}{\partial V} = \frac{c}{4\pi^2 rR}\frac{\partial \Phi}{\partial r} = -\frac{m-nq}{m}\frac{q}{B}\frac{B_0^2 v_{\parallel}}{(2\pi qR)^2} \tag{4.36}$$

Equation 4.36 can then be further rearranged to give the equation relating the poloidal Mach number to each magnetic mode (m,n), shown in Chapter 1 of this document that has been used in past calculations:

$$M_p = -\frac{cE_r}{v_t B_p} = -\left(\frac{m-nq}{m}\right) \tag{4.37}$$

In this work, we no longer make the assumption that the parallel flow is zero as $V_{\|}$ has been measured to be 20 km/s in HSX as shown in Figure 2.7 with the potential to grow to the order of the ion thermal speed when an external current is applied to the plasma, as seen in Figure 3.3. From Equation 4.32 it is clear that by increasing the parallel velocity, the resonant electric field also increases and that any parallel velocity at least on the order of the thermal velocity will be significant in shifting the resonance point. This work also does not use the large aspect ratio tokamak approximation that Shaing used to reach Equation 4.36, but rather a numerical calculation of the Hamada coordinates [6] where the toroidal flux is the radial coordinate. In this coordinate system, the poloidal and toroidal angles vary between 0 and 2π instead of 0 and 1. This Jacobian is then given as:

$$\sqrt{g} = \frac{1}{4\pi^2}\frac{dV}{d\psi} \tag{4.38}$$

where ψ is the toroidal flux through a magnetic surface. The calculations presented in the next chapter also use the full magnetic field spectrum for HSX.

A comparison of the resonant electric field using the numerically calculated values in Equation 4.32 and the large aspect ratio tokamak approximation used by Shaing in Equation 4.37 is shown in Figure 4. 2 as a function of r/a. For this comparison the parallel velocity was set to zero. It can be seen that the approximation used by Shaing largely agrees with the numerical calculations to within 20%.

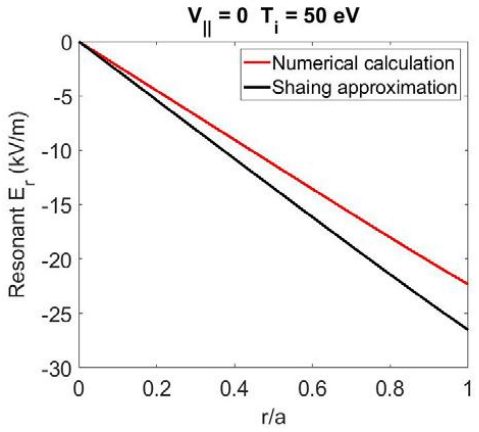

Figure 4. 2 The resonant electric field as a function of r/a using the numerically calculated HSX values (red) and the Shaing approximations (black). *[7]*

4.3 Poloidal Viscosity in HSX

The poloidal viscous damping as defined in Equation 4.15 is plotted as a function of the radial electric field without parallel flow for the HSX parameters shown in Figures 2.4 and 2.5.

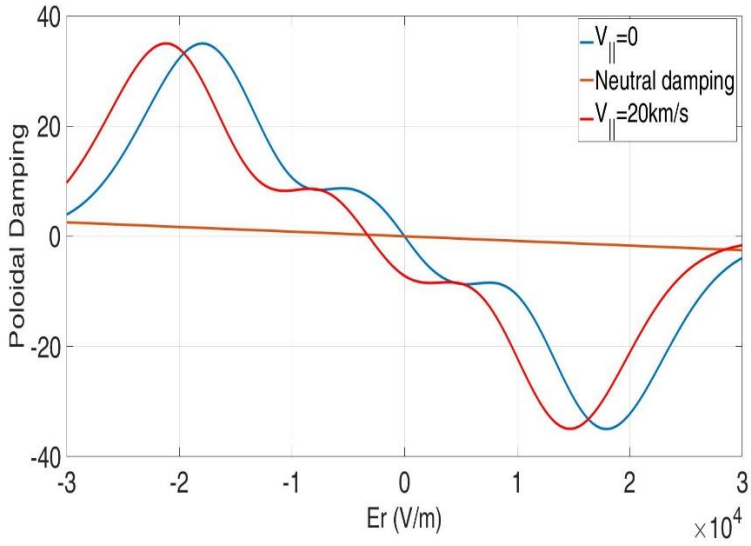

Figure 4. 3 Poloidal damping mechanisms in HSX's QHS configuration plotted for comparison as functions of the radial electric field. The poloidal viscous damping with no parallel flow (blue), the poloidal viscous damping with HSX's intrinsic parallel flow (red), and neutral damping (orange) are all shown.

Figure 4. 3 shows the poloidal viscosity with $V_{||} = 0$ as well as with $V_{||} = 20$km/s, the parallel flow that was measured in HSX in the absence of any external momentum sources, as shown in Figure 1.8. Figure 4. 3 clearly shows that the viscous damping plot including parallel flow is a shifted version of the one where $V_{||} = 0$. This is consistent with the physical interpretation of the resonance presented by Figure 1.3. It is also important to note that the neutral damping in HSX is much lower than the viscous damping in the vicinity of the resonant electric field. This indicates that, unlike what was observed in IMS in Figure 1.4, the neutral damping is not strong enough to cause the resonance to vanish in HSX. In the remainder of this work, the term "poloidal damping" will refer to the addition of the neutral damping and the poloidal viscous damping.

4.4 Solutions to the Steady-state Momentum Balance Equations

Figure 3.1 clearly shows that the parallel flow is increased in the presence of an external bias and Figure 4. 3 shows that the parallel flow shifts the location of the resonant electric field. The question is then posed as to whether the shift in the resonant electric field due to the parallel flow will outpace the bias electrode's increase of the radial electric field. To answer this question, the momentum balance Equations 3.2 and 3.4 will be solved at steady-state with the external torque $\langle \boldsymbol{J_{ext}} \cdot \boldsymbol{\nabla \Psi} \rangle$ as an independent variable to determine the equilibrium values of the parallel flow and the radial electric field at the resonance. Due to the shape of the poloidal viscosity profile, it is expected that for a given external torque, which is independent of the radial electric field, multiple steady-state solutions would be found for the momentum balance equations.

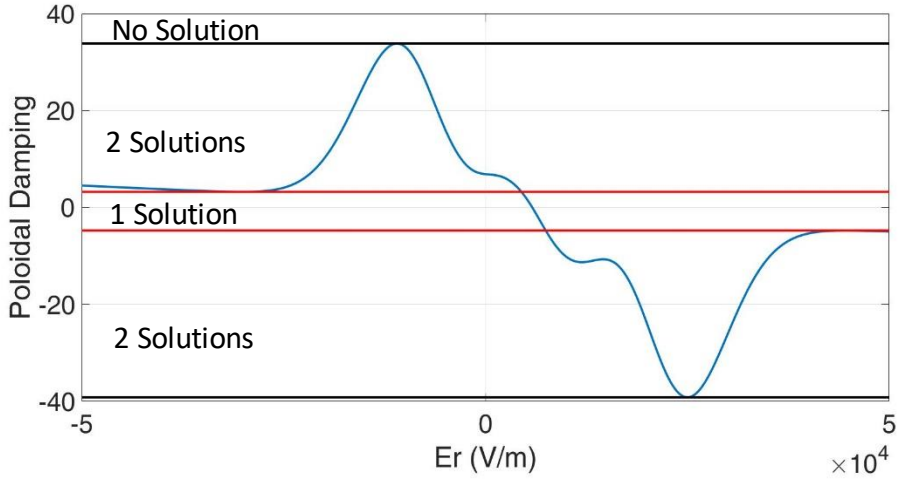

Figure 4. 4 Regions of multiple solutions due to the non-linearity of viscosity. The horizontal lines indicate the boundaries to regions where a different number of solutions to the momentum balance equations exist.

Figure 4. 4 shows regions of multiple solutions to the steady-state poloidal and parallel momentum balance Equations 3.4 and 3.2 previously shown in Chapter 3:

$$\langle \boldsymbol{B_p} \cdot \boldsymbol{\nabla} \cdot \boldsymbol{\pi} \rangle + M_i N_i v_{in} \langle \boldsymbol{B_p} \cdot \boldsymbol{V_i} \rangle = \frac{\sqrt{g} B^{\theta} B^{\zeta}}{c} \langle \boldsymbol{J_{ext}} \cdot \boldsymbol{\nabla} \Psi \rangle \quad (4.39)$$

and

$$\langle \boldsymbol{B} \cdot \boldsymbol{\nabla} \cdot \boldsymbol{\pi} \rangle + M_i N_i v_{in} \langle \boldsymbol{B} \cdot \boldsymbol{V_i} \rangle = 0 \quad (4.40)$$

respectively. Because these equations are being solved in steady-state, the external current, $\boldsymbol{J_{ext}}$, is equal to the negative plasma current, $\boldsymbol{J_{plasma}}$. The existence of multiple solutions is because of the nonlinear nature of the viscosity. The horizontal lines in Figure 4. 4 correspond to values of $\langle \boldsymbol{J_{ext}} \cdot \boldsymbol{\nabla} \Psi \rangle$ which are equal to the total poloidal damping and separate the regions where a different number of solutions to the momentum balance equations exist. Between the two red lines one solution to the momentum balance equations exists. Between the red and black lines two solutions of interest exist. Past the black lines, no solutions exist. In the two-solutions region, this work defines the solution found between the peaks of the poloidal damping as "Solution 1" and the solution found past the peaks as the "Solution 2".

Matlab's "fsolve" function was used to solve the system of two non-linear equations, Equations 4.39 and 4.40, for the radial electric field and the induced parallel flow for a given

$\langle \boldsymbol{J_{ext}} \cdot \boldsymbol{\nabla \Psi} \rangle$. For the next iteration of $\langle \boldsymbol{J_{ext}} \cdot \boldsymbol{\nabla \Psi} \rangle$, the solutions from the previous iterations were used as the initial starting points for the fsolve function.

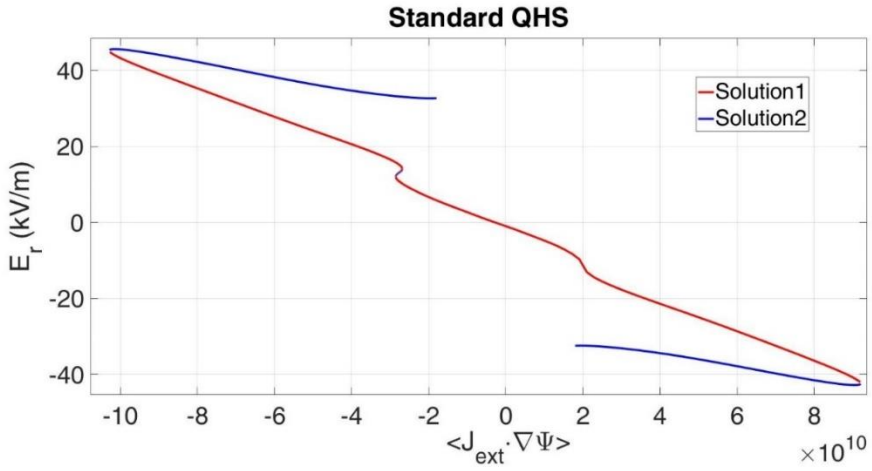

Figure 4. 5 The steady-state radial electric field as a function of the external current in the QHS configuration. The resonant electric field values are at 45kV/m and -42kV/m.

Figure 4. 5 shows how the steady-state electric field changes as a function of an external torque. The points where Solution 1, in red, and Solution 2, in blue, meet correspond to the maximum in poloidal damping and, therefore, to the resonant electric field. The resonant electric field calculated with this model for the QHS configuration, about 45kV/m, is over twice as large as the resonant electric field where $V_{\parallel} = 0$, about 18kV/m as seen in Figure 4.4.

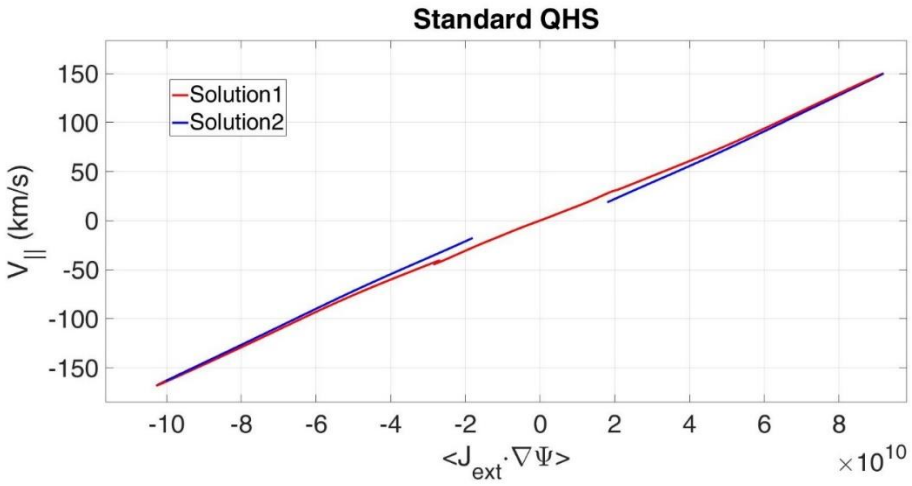

Figure 4. 6 The steady-state parallel mass flow as a function of the external current in the QHS configuration. Flows driven at the two resonance points are -168km/s and 150km/s.

Figure 4. 6 shows the steady-state values for parallel mass flow as a function of externally driven torque. The large parallel flow, approximately 168km/s, is what shifts the peak in viscosity to a radial electric field value larger than what was predicted in the $V_{\parallel} = 0$ calculations. These velocity values are much larger than the ion thermal velocity. However, other damping mechanisms such as turbulence or perpendicular viscosity that are not included in the model may also damp the parallel flow. This will be discussed further in Chapters 5 and 6.

Because large parallel flow shifts the location of the resonant electric field, our attention is focused on controlling the parallel flow damping mechanisms, in order to make the resonant electric field more accessible on HSX. Since neutral damping plays a major role in damping parallel flow, as shown by Dobbins [8], steady-state value calculations were performed for the QHS configuration with varying levels of neutral density while keeping all other parameters at the same values.

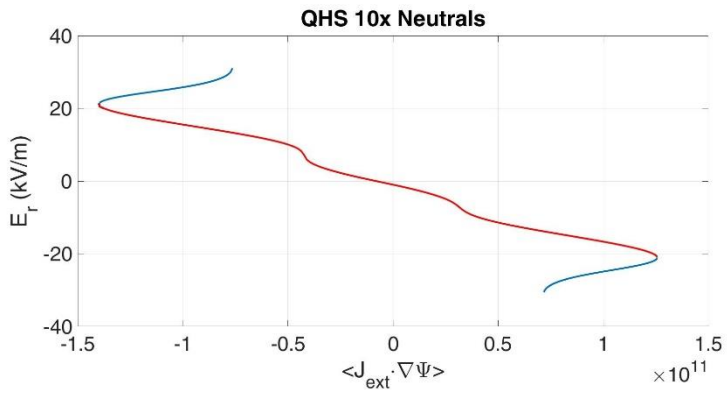

Figure 4. 7 The steady-state radial electric field as a function of the external current in the QHS configuration with ten times neutral density values. The resonant electric field values are 23kV/m and -23kV/m.

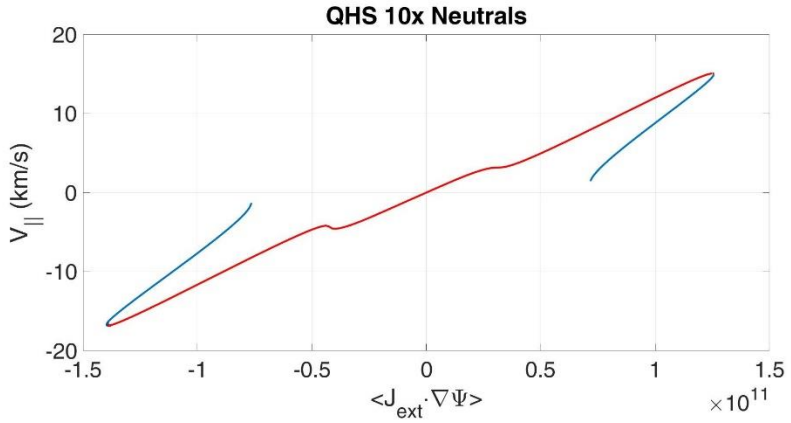

Figure 4. 8 The steady-state parallel mass flow as a function of the external current in the QHS configuration with ten times neutral values. The flows driven at resonance points are -34km/s and 30km/s.

As seen by comparing Figure 4. 6 to Figure 4. 8, the increased neutral density damps the parallel flow. The decreased parallel flow causes less of a shift in the viscosity, thus decreasing the resonant electric field by about 50% from the regular QHS case, as seen by comparing Figure 4. 5 to Figure 4. 7.

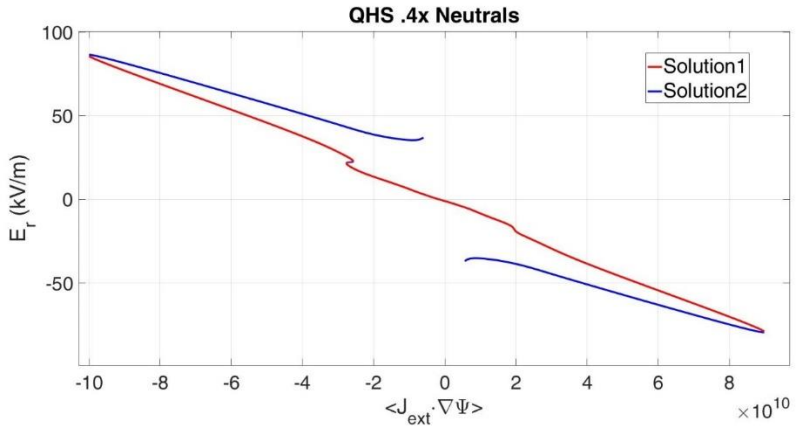

Figure 4. 9 The steady-state radial electric field as a function of the external current in the QHS configuration with 0.4 times neutral values. The resonant electric field values are 86kV/m and -80kV/m.

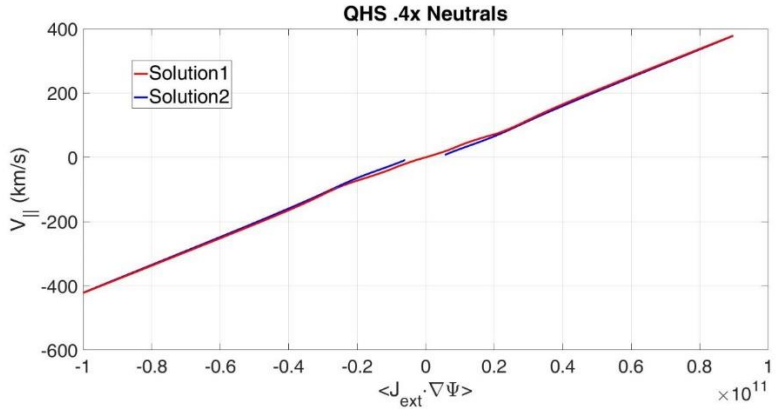

Figure 4. 10 The steady-state parallel mass flow as a function of the external current in the QHS configuration with 0.4 times neutral values. The flows driven at resonance points are -422km/s and 376km/s.

Figure 4. 9 and Figure 4. 10 show the converse of what was seen in Figure 4. 7 and Figure 4. 8: the decreased neutral density allows for extremely high parallel flows to develop, which raises the resonant electric field by a factor of almost two from the regular QHS case.

Experimentally, it is difficult to simply raise and lower the neutral damping, especially without affecting the other plasma parameters. This would make it an impractical method to find the resonant electric field in the laboratory. One of the features of the QHS configuration, compared to the other configurations, is that the viscous damping is very low in the direction of symmetry. Steady-state value calculations were performed in the Mirror and F14 configurations, which have larger viscous damping along the magnetic field, to see how the resonant electric field is affected.

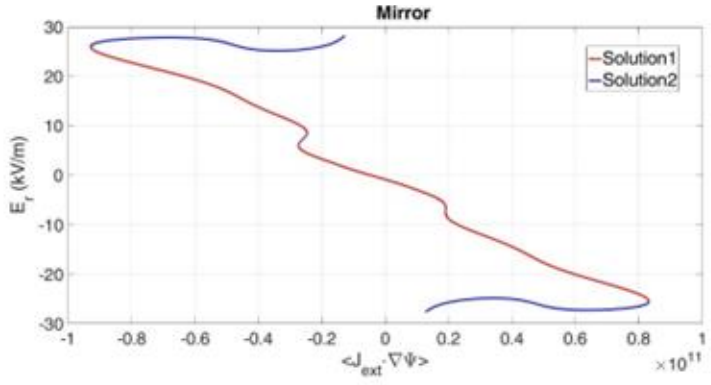

Figure 4. 11 The steady-state radial electric field as a function of the external current in the Mirror configuration. The resonant electric field values are 26kV/m and -25kV/m.

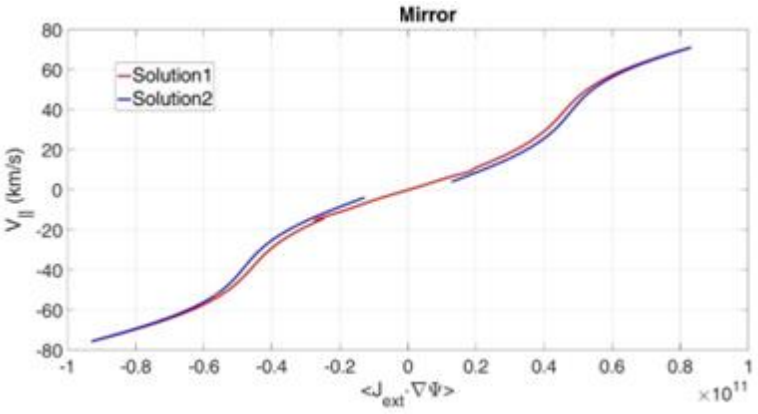

Figure 4. 12 The steady-state values for parallel mass flow as a function of the external current in the Mirror configuration. Flows driven at the resonance points are -76km/s and 71km/s.

As seen in Figure 4. 11, the resonant electric field drops significantly from the QHS case to the Mirror case, down to about 55% of the resonant electric field from the regular QHS case. The increase in viscosity from the Mirror configuration heavily damps the parallel flow to less than half of what its value is at the resonant point in the regular QHS case. This result is important for experimental work because, unlike the neutral density, the configuration of HSX can be changed relatively easily. More steady-state value simulations were conducted in different configurations such as the Mirror with no neutrals and for the F14 configuration. The resonant electric field and parallel velocity for these cases are also included in the figure below.

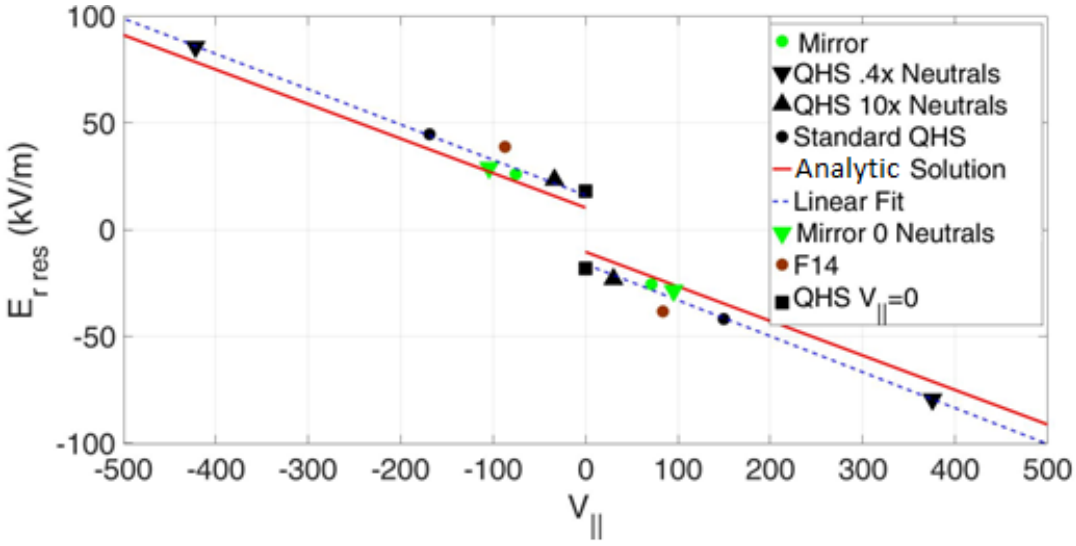

Figure 4. 13 Resonant electric field as a function of parallel velocity at resonance of several configurations in HSX. Points denote the QHS configuration (black), the Mirror configuration (lime), and the Flip14 configuration (brown). Also plotted are a linear regression of the HSX cases (blue dotted line) and the analytic approximation of the resonant electric field (red) given by Equation 4.32.

Figure 4. 13 depicts the resonant electric fields and parallel flows at the resonance points for all the configurations simulated. A linear regression for the calculated points as a dashed blue line is also shown. The red line in this figure is the analytical approximation of the resonant electric field given by Equation 4.32. There is a discontinuity in this line at $V_{||}$=0 because of the change in direction of $V_{||}$ being in phase with different directions of ExB drift. There is a small difference between the linear regression and the general solution. The reason for this is that Equation 4.32 does not account for the integration over the velocity, which is performed when the viscosity is calculated. In Figure 4. 13, it is seen that the resonant electric field in QHS with the current model is over two times higher than that predicted by the older model under the assumption that $V_{||}$=0. The figure also shows that the electric field needed to find the resonance

in the Mirror configuration is almost half of the resonant electric field for the QHS configuration, making the Mirror configuration a very attractive option to search for the resonance in HSX.

4.5 Comparison to Tokamaks

While looking at the data of previous experiments, presented in Chapter 1 in Figures 1.4 [9], 1.5 [10], and 1.6 [11], the question arises as to why the resonance was observed in other machines close to the value predicted if $V_{\|}=0$, but not in HSX. To explore this, the steady-state values for HSX were calculated in a fictional "Tokamak configuration". In these calculations, all the machine parameters remain the same as the QHS configuration, except for the magnetic spectrum. The QHS (4,1) mode was set to be a (0,1) mode, while all other modes were ignored.

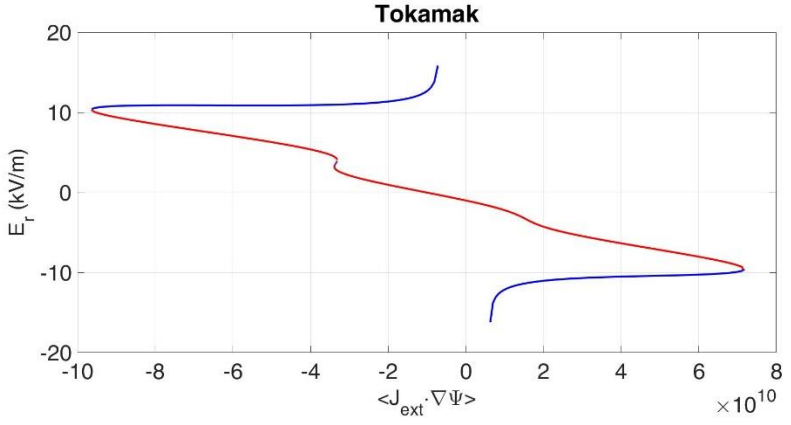

Figure 4. 14 The steady-state radial electric field as a function of external current in the Tokamak configuration. The resonant electric field values are 10kV/m and -10kV/m.

Figure 4. 14 shows the radial electric field of the Tokamak configuration of HSX as a function of external current. The resonant electric fields shown in this figure are about four

times lower than those of the QHS configuration. While this difference in resonant electric field is partially explained by the magnetic mode numbers of the configuration, the velocity driven by the current shown in Figure 4.17 is also responsible.

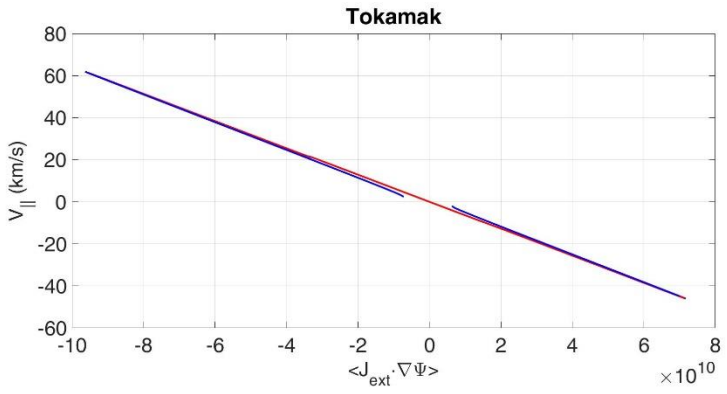

Figure 4. 15 The steady-state parallel mass flow as a function of external current in the Tokamak configuration. The flows driven at the resonance points are 62km/s and -46km/s.

While Figure 4. 15 clearly shows a lower parallel flow driven by the external current than the QHS configuration, it is important to examine how much the parallel flow shifts the resonant electric field from the $V_{||}$=0 prediction in this Tokamak configuration. To observe this, the poloidal viscous damping of the Tokamak configuration was calculated for $V_{||}$=0 and $V_{||}$=62km/s.

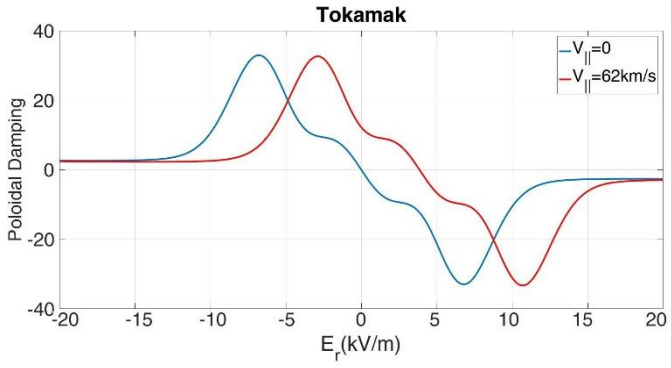

Figure 4. 16 The poloidal viscous damping as a function of the radial electric field for the Tokamak configuration with $V_{||}$=0 (blue) plotted against $V_{||}$=62km/s (red) where the resonant electric fields occur at 7kV/m and 10kV/m respectively.

Figure 4. 16 shows the shift in the resonant electric field going from the $V_{||}$=0 approximation to $V_{||}$=62km/s that is calculated to be present at the resonance. The 62km/s driven in the Tokamak configuration only shifts the resonant electric field by about 4kV/m compared to the $V_{||}$=0 case. To compare this shift with the shift in QHS configuration, the viscous damping was calculated in the QHS configuration for $V_{||}$=0 and $V_{||}$=62km/s.

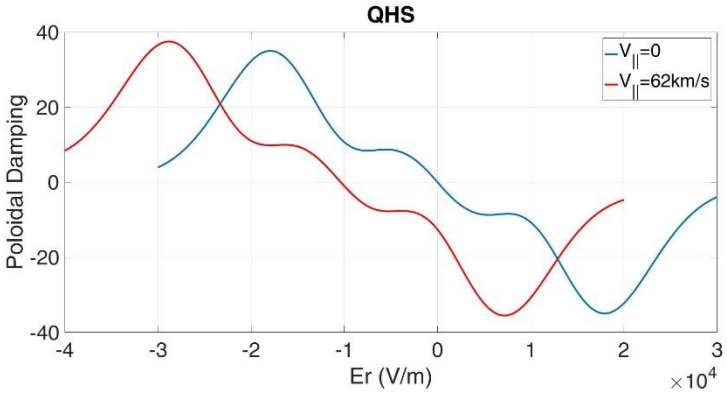

Figure 4. 17 The poloidal viscous damping as a function of the radial electric field for the QHS configuration with $V_{||}$=0 (blue) plotted against $V_{||}$=62km/s (red).

Figure 4. 17 shows a large shift in the resonant electric field in QHS configuration for $V_{\|}$=62km/s compared to the shift seen in Figure 4. 16. In the QHS configuration, the resonant electric field is shifted by 10.8kV/m with $V_{\|}$=62km/s, about 2.5 times the shift in the Tokamak configuration for the same velocity. This is consistent with Equation 4.32, where the shift due to the parallel velocity is multiplied by a factor determined by the magnetic mode numbers: $\frac{m-nq}{m}$. For a tokamak, this factor is equal to 1. For QHS, it is equal to 3. Thus, one would expect a factor of 3 difference in shift going from tokamak to QHS configurations. These results further explain why the resonance was seen in other machines but not HSX. The viscosity in QHS is more susceptible to shifts from parallel flows than in other configurations. Unfortunately, due to the lack of available information of TEXTOR's parameters, it has not been possible to accurately model TEXTOR at the time of writing.

References

[1] K. C. Shaing, "Test of tokamak low-mode-high-mode transition theory in stellarators," *Physics of Fluids B: Plasma Physics,* vol. 5, no. 11, p. 3841, 1993.

[2] S. P. Hirshman and D. J. Sigmar, "Neoclassical transoport of impurities in tokamak plasmas," *Nuclear Fusion,* vol. 21, no. 9, p. 1079, 1981.

[3] Ag2gaeh, "Wikipedia," [Online]. Available: https://en.wikipedia.org/wiki/Spherical_coordinate_system#/media/File:Kugelkoord-lokb-e.svg. [Accessed 16 06 2021].

[4] M. Coronado and J. N. Talmadge, "Evolution of the plasma rotation and the radial electric field for a toroidal plasma in the Pfirsch-Schluter and plateau regimes subject to a biased electrode," *Physics of Plasmas,* vol. 5, no. 4, p. 1200, 1993.

[5] M. Coronado and J. Galindo Trejo, "Calculation of Hamada coordiantes for a large-aspect-ratio tokamak," *Physics of Fluids B: Plasma Physics,* vol. 2, no. 3, p. 530, 1990.

[6] J. N. Talmadge and S. Gerhardt, "Numerical calculation of the Hamada basis vectors for three-dimensional toroidal magnetic configurations," *Physics of Plasmas,* vol. 12, no. 7, p. 072513, 2005.

[7] J. N. Talmadge, *Personal Communication,* 2021.

[8] T. Dobbins, S. T. A. Kumar, J. N. Talmadge and D. T. Anderson, "The role of neutral friction in governing parallel flows in the HSX stellarator," *Nuclear Fusion,* vol. 59, no. 2, p. 046007, 2019.

[9] H. Dahi, "Nonlinear Viscosity in the Interchangeable Module Stellarator," *University of Wisconsin-Madison,* 1997.

[10] S. Kitajima et al, "LH transition by a biased hot cathode in the Tohoku University Heliac," *Nuclear Fusion,* vol. 46, no. 2, p. 200, 2006.

[11] R. R. Weynants, S. Jachmich and M. Van Schoor, "Electrode Biasing on TEXTOR: A Tool for Fundamental Physics Studies," *Fusion Science and Technology,* vol. 47, no. 2, p. 202, 2005.

---5---

An Analysis of the Stability of Solutions to the Momentum Balance Equations

In the previous Chapter, two steady-state solutions of the momentum balance equations were focused on as they relate to the ion resonant electric field and calculating its value. In this Section 5.1, we show that there is a third solution in this model and discuss the physical criteria for the creation of further solutions. In Section 5.2, a vector field is created to determine the stability of the three solutions. In Section 5.3, the stability of the solutions is analyzed and the physical mechanism driving the instability of one of the solutions is discussed. Finally, in Section 5.4 the hysteresis behavior of the plasma as it transitions between different stable states is shown for both the parallel flow and radial electric field.

5.1 Identifying additional steady-state solutions

In Chapter 4, the only two solutions discussed were those pertaining to the ion resonance. We defined Solution 1 as occurring when the viscosity is increasing with respect to the E_r where and Solution 2 occurs when the viscosity is decreasing with respect to E_r. However, this was an incomplete definition as Solution 2 ceases to exist while the viscosity decreases with increasing E_r. We now modify the definition to say that Solution 2 exists when the viscosity is decreasing with respect to E_r and the viscosity remains the dominant damping mechanism. Where the neutral damping has increased to the point where it is the dominant damping mechanism and the total poloidal damping is once again increasing as a function of E_r, we define as the beginning of Solution 3.

It was discussed earlier in Section 4.4 that it was unlikely that the velocities in HSX will reach as high as shown in Figure 4.6 due to damping mechanisms present in HSX that are not currently included in the model, such as turbulence. In order to account for a variety of additional damping mechanisms, the neutral density was increased to ten times the experimental value, similar to Gerhardt's method of matching his model to his experimental results [1]. All calculations and plots will use this increased neutral density for the remainder of this document. Plotting the total poloidal damping with the new neutral density, similar to Figure 4.4, clearly shows the existence of more solutions than accounted for in Chapter 4.

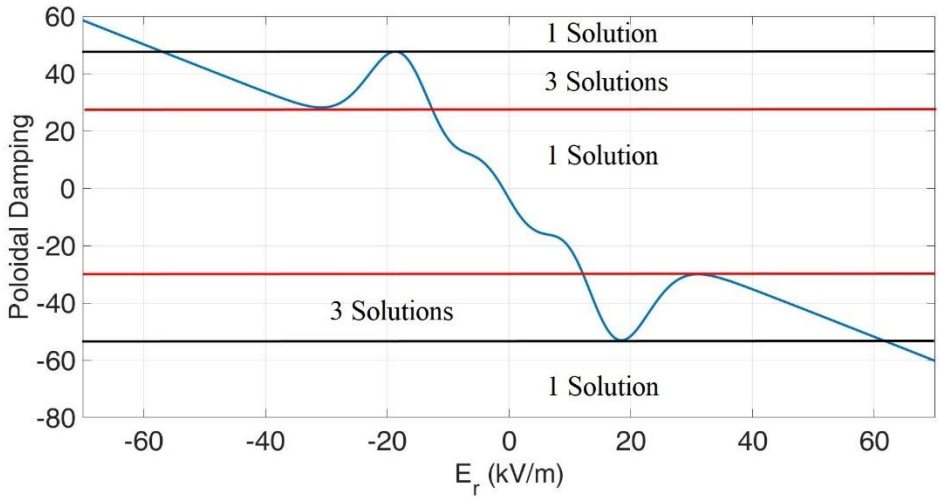

Figure 5. 1 Regions of multiple solutions due to the non-linearity of viscosity with ten times the experimental neutral density. The horizontal lines indicate the boundaries of regions where a different number of solutions to the momentum balance equations exist.

As seen in Figure 5. 1, a third solution is prominent in the region between the red and black lines. This solution is due to the neutral damping becoming the dominant damping mechanism as it continues to rise linearly while the viscosity decreases. While this solution is present, though barely visible, in Figure 4.4, the rate at which neutral damping increased was so

miniscule that the third solution was not considered relevant then. Though it is not explicitly shown in Figure 5. 1, the third solution continues to extend linearly past the black lines.

With this new third solution in mind, we then recalculate the steady state solutions of the momentum balance equations with the increased neutral damping.

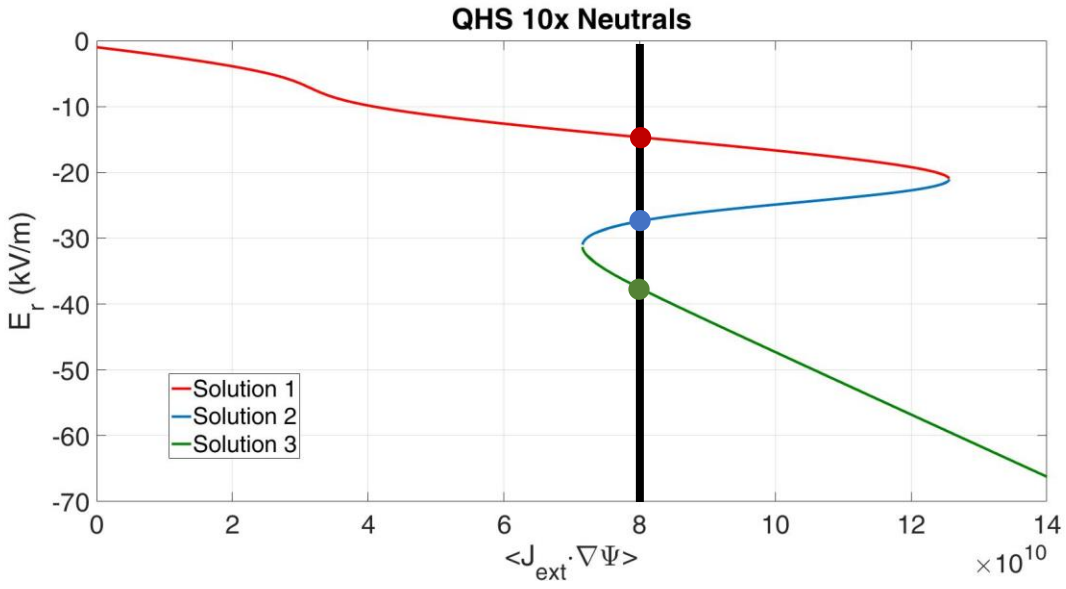

Figure 5. 2 The steady state radial electric field as a function of the external current in the QHS configuration with ten times the experimental neutral density. In addition to a lower resonant electric field than seen in Figure 4.7, the third solution is prominently shown. The black line indicates the external current value that will be used in later calculations.

Figure 5. 2 is similar to Figure 4.7 in that it shows the steady state solutions for the radial electric field as a function of the external current. Once again, Solution 1 and Solution 2 are plotted in red and blue respectively and where they meet corresponds to the location of a maximum in poloidal damping. However, unlike Figure 4.7, Figure 5. 2 also has Solution 3 plotted in green. The point where Solutions 2 and 3 meet therefore corresponds to a minimum in the poloidal damping, seen in Figure 5.1.

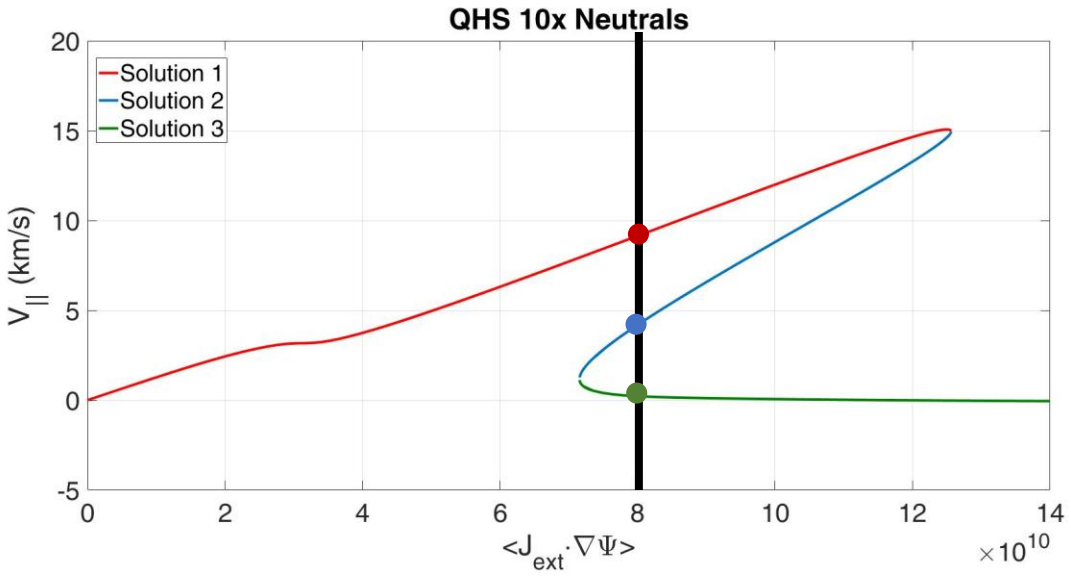

Figure 5. 3 The steady state parallel mass flow as a function of the external current in the QHS configuration. The flow driven at the resonance point is 15km/s and the third solution is shown to have extremely low parallel mass flow. The black line indicates the external current value that will be used in later calculations.

Figure 5. 3 is similar to Figure 4.8 in that it shows the steady state solutions for the parallel mass flow as a function of the external current. However, due to the increased neutral density, the parallel mass flow does not increase nearly as much as it did for the experimental value of the neutral density. At its peak, the parallel mass flow is barely more than what was measured by Briesemeister in the core of HSX without external momentum sources [2]. Because of the low parallel mass flow, the resonant electric field with ten times neutrals is much closer to the $V_{\|} = 0$ approximation. Additionally, the parallel mass flow goes to zero in the third solution due to the parallel viscosity having decreased to the point to where there can no longer be flow in that direction. Drawing on the physical model discussed in Shaing and Crume [3], the radial electric field drives an $\boldsymbol{E} \times \boldsymbol{B}$ flow that is perpendicular to the field line. Parallel viscosity then drives a parallel flow so that the net flow is in the direction of minimal gradient in |B|. For HSX,

this is in the direction of quasihelical symmetry. As the parallel viscosity becomes negligible at high values of E_r, the parallel flow also becomes negligible. The strong ExB drift from the high electric field forces the plasma flow almost entirely in the perpendicular direction.

It is worth noting that in this model, there are only three solutions maximum to the momentum balance equations, depending on the external current. However, there could be more if more non-linear damping terms are added. In the event that there is another damping term that is also non-linear with respect to the radial electric field, and it becomes the dominant damping mechanism at some point, then two more steady-state solutions to the momentum balance equations would be created. Thus, depending on the number of damping mechanisms and their relative magnitudes, one could imagine that many equilibrium solutions may exist in complex systems. Conversely, if there is a single damping mechanism that dominates all the others, such as an extremely high neutral damping term, then there would only be a single equilibrium solution and the ion resonance would not even be seen.

5.2 Determining the stability of the steady-state solutions

With a third solution identified, we now turn our attention back to analyzing the stability of the different solutions to the momentum balance equations. In order to analyze the stability, a vector field was created for the system under a given external current and applied to the momentum balance equations 2.39 and 2.40.

The current was chosen to be $\langle \boldsymbol{J_{ext}} \cdot \boldsymbol{\nabla \Psi} \rangle$ = 8e10 as all three solutions exist with that current. A qualitative assessment of the stability properties of the steady-state solutions (or fixed points) of the momentum balance equations can be provided by plotting the phase portrait consisting of the vector field of points that correspond to $\frac{\partial \Phi'}{\partial t}$ and $\frac{\partial \lambda}{\partial t}$ from Equations 3.16 and

3.17 at each point given by Φ' and λ on a two-dimensional grid and then converted to the E_r, $V_\parallel$ plane. If the vectors surrounding a steady state value (E_{r0}, $V_{\parallel 0}$) are pointing toward that point, then the solution is stable. If there are vectors pointing away, then the solution at (E_{r0}, $V_{\parallel 0}$) is unstable. The resulting plot can then provide a clear overview of the stability of the three solutions and how the plasma evolves under different conditions.

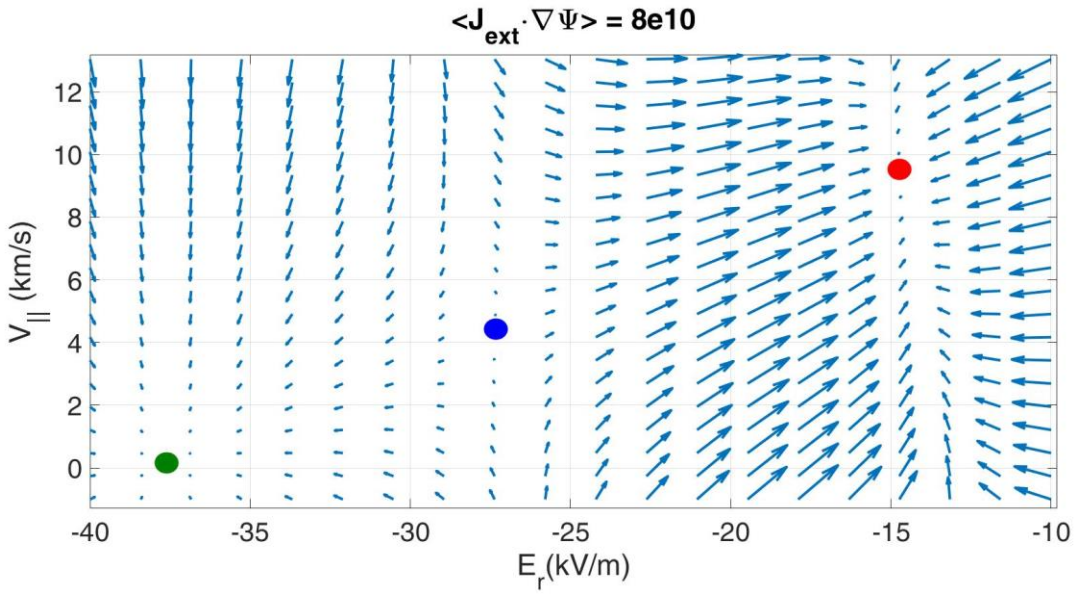

Figure 5. 4 A vector plot of E_r and $V_\parallel$ space showing the stability of the three solutions for a given external current. Solutions 1, 2, and 3 are marked by red, blue, and green dots respectively. The magnitudes of the vectors are the time derivatives $\frac{\partial \Phi'}{\partial t}$ and $\frac{\partial \lambda}{\partial t}$ of Φ' and λ and then converted to E_r and $V_\parallel$.

As can be seen in Figure 5. 4, Solutions 1 and 3 can be called stable due to the vectors pointing to those solutions. Conversely, the vectors point away from Solution 2, indicating that it is unstable. This would imply that transitions seen in other machines past the resonance point jump from Solution 1 to Solution 3, bypassing Solution 2 entirely.

5.3 Determining destabilizing mechanisms in the system

With the stability of the three solutions now determined, we turn our attention to identifying the mechanisms which cause the second solution to become unstable. In order to do this, we apply the eigenvalue method. Applying that method to this system, we analyze the time evolution of Φ' and λ when small, linearized perturbations are introduced about the steady state point (and then converted to E_r and $V_{||}$ as discussed previously). These take the form:

$$\lambda(t) = \lambda^{SS} + \Delta\lambda \tag{5.1}$$

$$\Phi'(t) = \Phi'^{SS} + \Delta\Phi' \tag{5.2}$$

Where Φ'^{SS} and λ^{SS} are the steady state values for Φ' and λ respectively and $\Delta\Phi'$ and $\Delta\lambda$ are the perturbations in Φ' and λ respectively. The time dependence is then expanded in a Taylor series about the steady-state point so that,

$$\frac{d}{dt}\begin{bmatrix}\Delta\lambda \\ \Delta\Phi'\end{bmatrix} = \begin{bmatrix}\frac{\partial J_{||}}{\partial\lambda} & \frac{\partial J_{||}}{\partial\Phi'} \\ \frac{\partial J_P}{\partial\lambda} & \frac{\partial J_P}{\partial\Phi'}\end{bmatrix}\begin{bmatrix}\Delta\lambda \\ \Delta\Phi'\end{bmatrix} \tag{5.3}$$

where the zeroth order term is zero at the steady state point and the higher order terms are ignored. The 2x2 matrix in Equation 5.3 is the Jacobian evaluated at the steady-state points, $J_{||}$ is the parallel damping and J_P is the poloidal damping and the drive term, corresponding to the right-hand sides of Equations 3.2 and 3.4 divided by the coefficients on the left hand side that multiply the $\frac{\partial\Phi'}{\partial t}$ and $\frac{\partial\lambda}{\partial t}$ terms respectively with $\langle \boldsymbol{J_{ext}} \cdot \boldsymbol{\nabla}\Psi \rangle$ = 8e10. By evaluating the equation $\det(A-\gamma I)=0$, where A is the Jacobian matrix, I is the identity matrix, and γ is the eigenvalue, the eigenvalues of the system at a given point are determined. The eigenvectors, **v**, are determined by solving $A\mathbf{v} = \gamma\mathbf{v}$ for each eigenvalue γ. This leads to general solutions of the form or $\boldsymbol{x}(t) = \boldsymbol{c_1 v_1} e^{\gamma_1 t} + c_2 \boldsymbol{v_2} e^{\gamma_2 t}$ where **x** contains both Φ' and λ with initial condition $x(t=0) = \boldsymbol{c_1 v_1} +$

$c_2\boldsymbol{v_2}$ [4]. A positive eigenvalue is an exponential growth away from the fixed point, indicating instability, while a negative eigenvalue is a decay back to the fixed point, indicating stability.

The Jacobian is evaluated at the steady state points for the selected external current to determine the eigenvalues and eigenvectors of the system for each of the three solutions.

Solution	1	2	3
γ_1	-4,890	-4,889	-4,890
γ_2	-30,110	+9,942	-4,380

TABLE 1: Eigenvalues for the momentum balance equations at each of the three steady state points when $\langle \boldsymbol{J_{ext}} \cdot \boldsymbol{\nabla \Psi} \rangle$= 8e10.

As seen in Table 1, Solutions 1 and 3 have two negative eigenvalues implying that these solutions are inherently stable. Meanwhile, Solution 2 has a negative and a positive eigenvalue implying that Solution 2 is an unstable saddle point.

We can further visualize the behavior of the plasma by plotting the eigenvectors around the steady state points to visualize the paths that the plasma will converge to and grow or decay along. The black solid lines are the solutions to the time-dependent equations given in Equations 3.2 and 3.4 with initial conditions that correspond to points on the boundary. The arrows show the direction of the solution, toward or away from the fixed points. By overlaying the eigenvectors with time traces, we can see that the eigenvectors predict the behavior of the plasma around the steady state points.

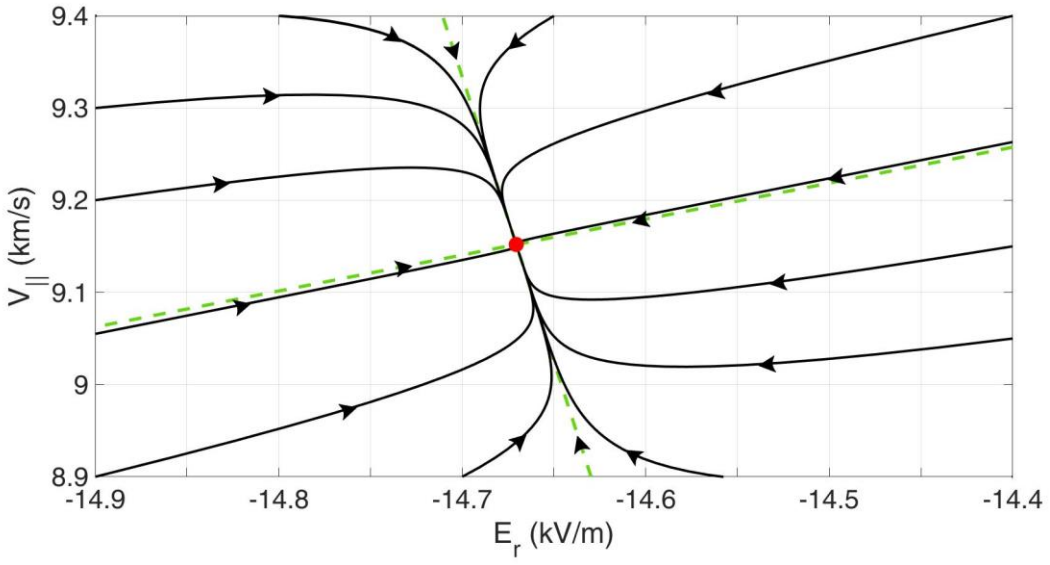

Figure 5. 5 The stable eigenvectors of Solution 1 (dashed green) and the time traces of the radial electric field and parallel mass flow (solid black).

Note that from Table 1, solution 1 has two eigenvalues with $|\gamma_2| > |\gamma_1|$. As seen in Figure 5.6, the larger amplitude eigenvalue γ_2 corresponds to the eigenvector with positive slope while the smaller eigenvalue corresponds to the eigenvector with negative slope. Since the general solution is of the form $e^{\gamma t}\boldsymbol{v}$, for positive time $t > 0$ the larger negative eigenvalue dies off quickly and the trajectories approach the fixed point parallel to the eigenvector with the smaller eigenvalue. Similarly for time $t < 0$ the trajectories move away from the fixed point parallel to the eigenvector with the larger eigenvalue.

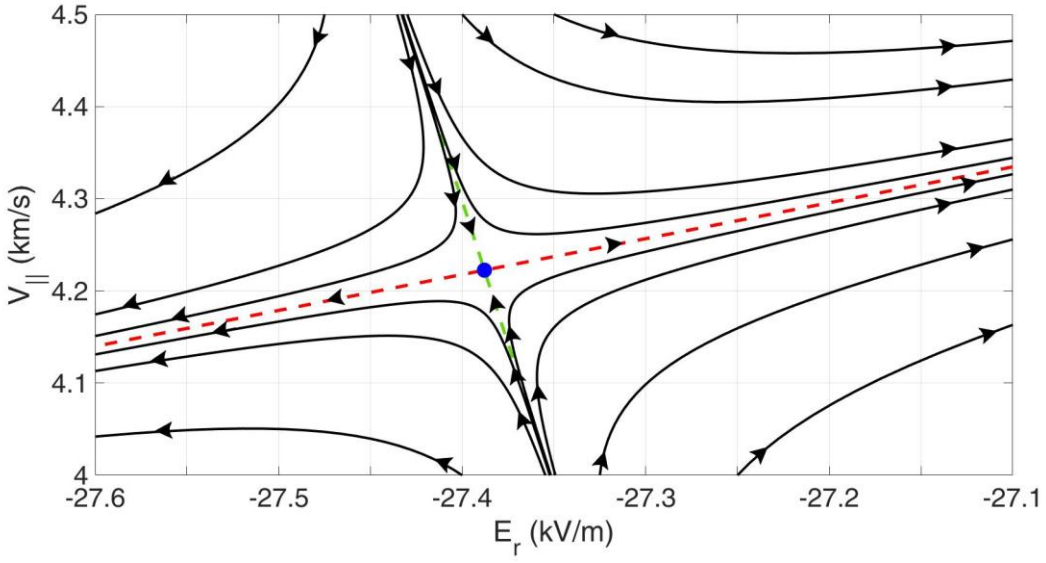

Figure 5. 6 The stable eigenvectors of Solution 2 (dashed green), the unstable eigenvectors (dashed red), and the time traces of the radial electric field and parallel mass flow (solid black).

Figure 5. 6 is similar to Figure 5. 5 in that it overlays the eigenvectors for Solution 2 with time traces of E_r and $V_{\|}$. Figure 5.6 shows the eigenvectors and trajectories for solution 2, which is an unstable saddle point. The eigenvector corresponding to the positive eigenvalue is shown in red. For this case all the trajectories diverge away from the fixed point parallel to the unstable eigenvector for time $t > 0$. Similarly, for time $t < 0$, the trajectories become parallel to the stable eigenvector. Note that the eigenvectors agree with the vector plot of Figure 5.4; the trajectory is toward the fixed point roughly parallel to the $V_{\|}$ axis and away from the fixed point roughly parallel to the E_r axis. The physical mechanism that leads to this instability is related to the relationship between E_r and the poloidal damping, which will be discussed later in this section. This leads to the saddle-point behavior seen in the figure.

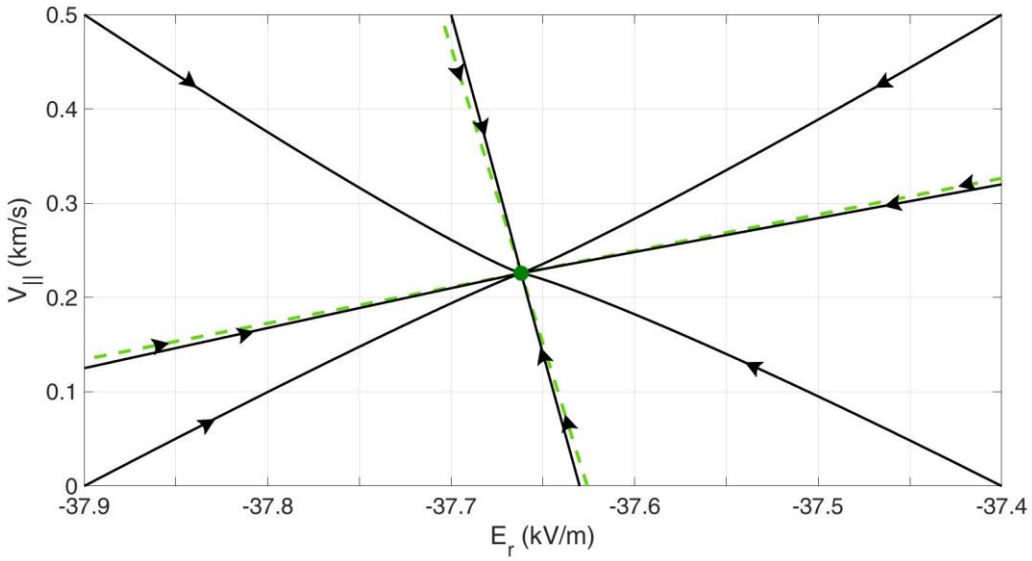

Figure 5. 7 The stable eigenvectors of Solution 3 (dashed green) and time traces of the radial electric field and parallel mass flow (solid black).

Finally, Figure 5. 7 shows the eigenvectors for Solution 3 with time traces showing the stability of the steady state point. Unlike the other two solutions, the eigenvalues for Solution 3 are almost equal. This is the case where the viscous damping is negligible and only damping due to neutrals exist. A linear combination of two eigenvectors, $x(t=0) = \boldsymbol{c_1 v_1} + c_2 \boldsymbol{v_2}$ leads to $\boldsymbol{Ax} = \boldsymbol{c_1 \gamma v_1} + c_2 \gamma \boldsymbol{v_2} = \boldsymbol{\gamma x}(\boldsymbol{t=0})$ so any linear combination of the two eigenvectors is also an eigenvector of the system. In this case all trajectories are straight lines and the steady-state solution is known as a star node [4]. For solution 3, the eigenvalues are not exactly equal and close to the fixed point it can be seen that the trajectories bend toward the eigenvector with the smaller eigenvalue (the green dashed line with positive slope).

While these plots may not provide much information that cannot be gathered from Figure 5. 4, the physical mechanism behind the instability of Solution 2 is seen when evaluating the elements of the Jacobian. The element of the Jacobian that causes the 2nd eigenvalue to change

sign is the derivative of the poloidal damping with respect to E_r. With this in mind, we plot the poloidal damping as a function of E_r.

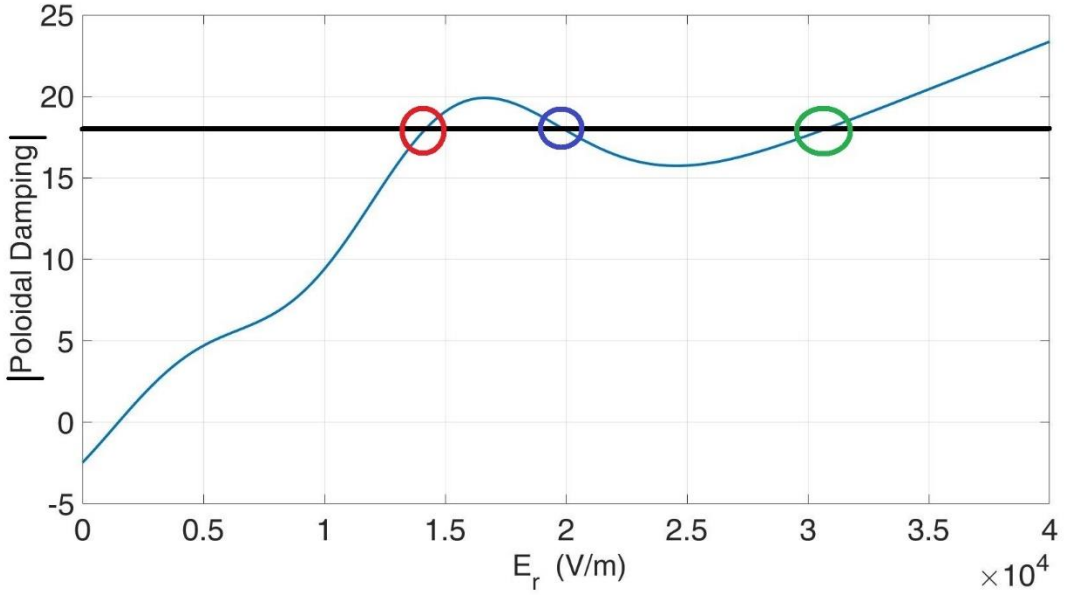

Figure 5. 8 The poloidal damping as a function of the radial electric field. The approximate locations of Solutions 1, 2, and 3 seen in Figure 5. 2 are shown by red, blue, and green circles respectively for the given external current indicated by the black line.

Figure 5. 8 shows the approximate locations of the three solutions on a plot of the magnitude of the poloidal damping for a given external current. The locations are approximate because the damping is plotted as a function of Er for a fixed $V_{||}$ whereas the three solutions actually have slightly different values of $V_{||}$ as seen in Figure 5.4.

As seen in Figure 5. 8, Solutions 1 and 3 both lie on regions of the curve where the magnitude of the poloidal damping is increasing with increasing E_r. If one were to perturb the plasma by increasing E_r at those two points, it would be met with increased damping and cause E_r to settle back at its steady state point. Similarly for perturbations involving a decrease in E_r, the damping decreases and the plasma again settles at the equilibrium point. However, Solution

2 lies on a region where the poloidal damping decreases with increasing E_r. Thus, any perturbative increase to E_r leads to a decreased damping, thus further increasing E_r and moving it away from the fixed point. Furthermore, we can say that stable solutions to the momentum balance equations only occur when the derivative of the poloidal damping with respect to the radial electric field is positive.

5.4 Transitioning between stable steady-state solutions

With the stability of all three solutions determined and the destabilizing mechanism identified, our attention once again turns to what a transition above the viscosity peak would look like in HSX. To simulate this, a time dependent external current is applied to the plasma.

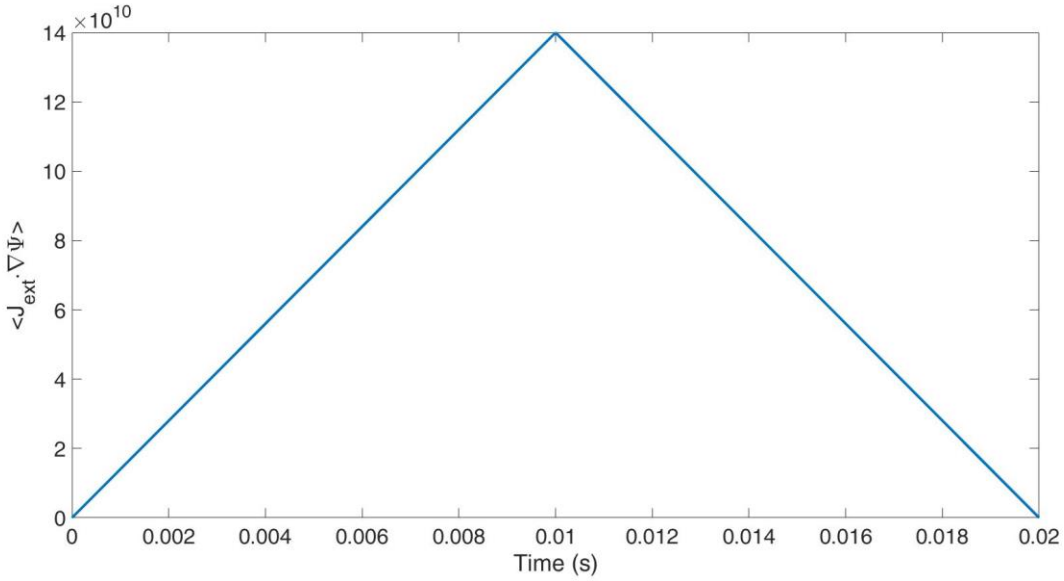

Figure 5. 9 The external current applied to the model to simulate transitions between Solution 1 and Solution 3.

Figure 5. 9 shows the triangular waveform of the current being simulated. The shape of the current was chosen to have two properties to clearly simulate the transition between Solution

1 and Solution 3. The first was that the peak current was selected such that only Solution 3 can exist at that point, thus ensuring a transition can occur. The second is that the timescale over which the current is increased is long enough such that both E_r and $V_{\|}$ are able to reach approximately 90% if their steady state values for the external current at a given time. This is done so that the solution space of E_r and $V_{\|}$ can be clearly determined by comparing their values with Figure 5. 2 and Figure 5. 3 respectively.

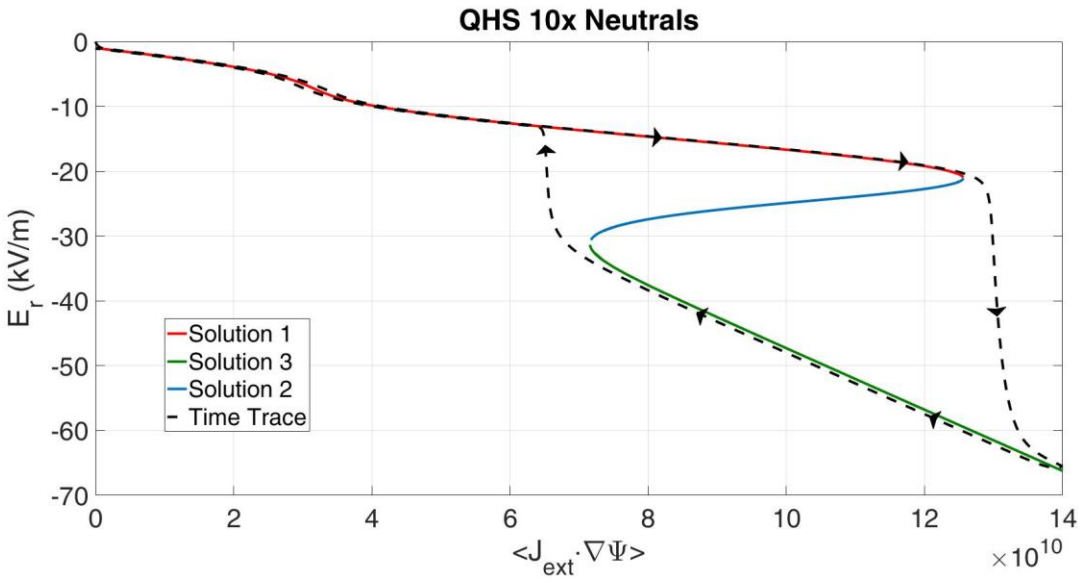

Figure 5. 10 A time trace of the radial electric field due to the external current shown in Figure 5.9 compared to the equilibrium solutions shown in Figure 5. 2. The radial electric field closely follows Solutions 1 and 3, but never Solution 2.

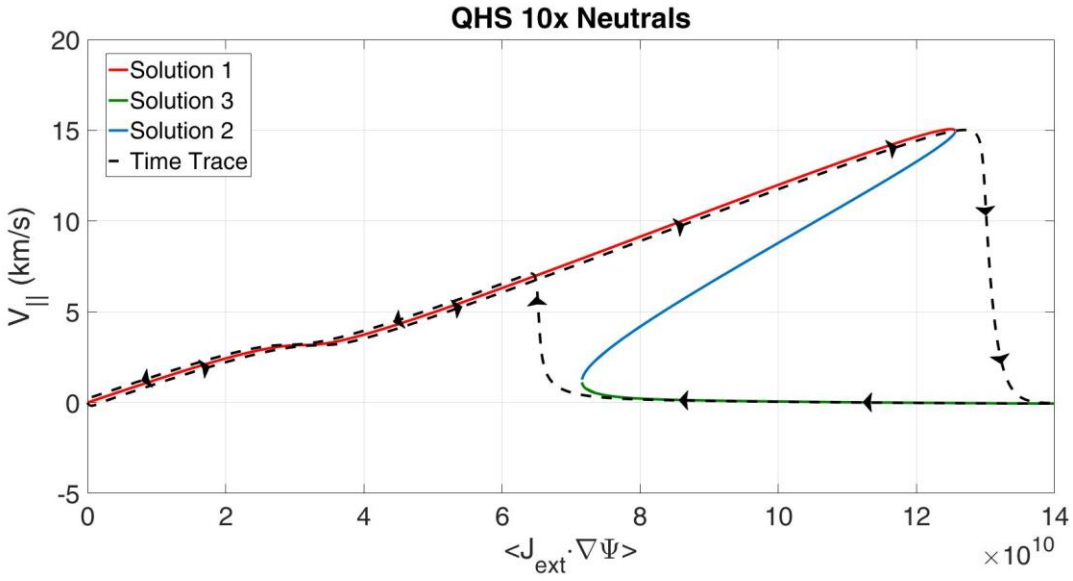

Figure 5. 11 A time trace of the parallel mass flow due to the external current shown in Figure 5.9 compared to the equilibrium solutions shown in Figure 5. 3. The parallel mass flow closely follows Solutions 1 and 3, but never Solution 2.

Figure 5. 10 and Figure 5. 11 show how the plasma evolves from a base state with no external current to a point with high external current and back to the base state. As can be seen clearly in both figures, E_r and $V_{||}$ evolve very closely along Solution 1 until the end of that solution space is reached. Then, both E_r and $V_{||}$ transition very rapidly to Solution 3 where the external current peaks. Once the external current begins to decrease, E_r and $V_{||}$ continue along the space of Solution 3 until the end of that solution space where it transitions quickly back to Solution 1 and returns to its base state as the external current reaches zero. As expected, the plasma never exists in the space of Solution 2 due to its unstable nature.

References

[1] S. Gerhardt, "Measurements and Modeling of the Plasma Response to Electrode Biasing in the HSX Stellarator," *University of Wisconsin-Madison,* 2004.

[2] A. Briesmeister, "Measurement and Modeling of the Flows and Radial Electric Field in the HSX Stellarator," *University of Wisconsin-Madison,* 2013.

[3] K. C. Shaing and E. C. Crume, "Bifurcation Theory of Poloidal Rotation in Tokamaks: A Model for the L-H Transition," *Physical Review Letters,* vol. 63, p. 2369, 1989.

[4] S. H. Strogatz, Nonlinear Dynamics and Chaos: with applications to physics, biology, chemistry, and engineering, Reading, Massachusetts: Perseus Books Publishing, 1994.

---6---

Conclusions and Future Work

Having shown the computational results in the previous chapters regarding the effect of the parallel flow on the radial electric field, the stability of different solutions to the momentum balance equations, and time evolution of E_r and $V_{||}$ as calculated by the momentum balance equations, we now discuss certain implications of these results as well as possible directions for future work. Section 6.1 summarized the major results of the preceding chapters. Section 6.2 discusses the implications of the parallel flow affecting the resonant electric field. This includes explanations for previously anomalous experimental results in HSX as well as implications for codes that solve the momentum balance equations. In Section 6.3, we discuss the behavior of the plasma as it transitions between different solutions. We compare the simulations to the experimental results as well as discuss how the transitions may differ given an expansion of our model. Finally, we conclude with thoughts on the future of this line of work in Section 6.4.

6.1 Summary of Results

In Chapter 2 of this document, an overview of the HSX machine was shown. Quasihelical symmetry was explained and HSX's way of breaking said symmetry to operate in other magnetic configurations was shown. The work that had been done on the machine in the past by scientists and graduate students that relate to the evolution of the parallel flow and radial electric field were discussed.

Chapter 3 introduced the momentum balance equations that became the foundation for the calculations performed in the rest of this document. The importance of using Hamada

coordinates in this work was covered and the terms included in the momentum balance equations were explained. The linear viscosity model was then applied to the momentum balance equations to show how the parallel flow and radial electric field evolve in the presence of an external bias. The importance of including the parallel flow due to its low damping in HSX was then discussed.

Chapter 4 introduced Shaing's model of non-linear viscosity. This model was able to calculate the ion resonant electric field with an analytic expression and was applied to the momentum balance equations. The equations were then solved in steady state to show the value of the ion resonant electric field while taking the parallel flow into account. It was shown that the inclusion of the parallel flow in the calculations shifts the ion resonant electric field and that by controlling the damping of the parallel flow, the ion resonant electric field could be shifted in a predictable manner.

Chapter 5 introduced the existence of a third solution to the momentum balance equations. The stability of all three solutions was investigated by using vector fields and eigenvalues. By examining Jacobian elements that were used to calculate the eigenvalues, the physical mechanisms behind the instability were found. The momentum balance equations were then solved to simulate transitions between the stable solutions and hysteresis behavior was observed for the radial electric field and the parallel flow.

The results in this work highlighted the role of the parallel flow in the calculation of the resonant electric field. The prominence of the parallel flow is a result of the unique property of quasihelical symmetry that HSX has which leads to a low viscous damping in the direction of quasisymmetry combined with the (4,1) mode's prominence in HSX allowing the resonance shift to be seen more easily. By solving the time dependent momentum balance equations with linear

viscosity, fast and slow damping timescales were observed, with the slow timescale dominating the evolution of the parallel flow. The radial electric field 's time evolution changed from being dominated by the fast timescale to the slow timescale as it gets further from the core. While the QHS configuration has a low viscosity to the point where neutral damping dominates the contribution to the slow timescale, this is not the case in the Mirror and F14 configurations where the viscosity plays a much larger role in the slow timescale.

When introducing Shaing's model of nonlinear viscosity and looking at its resulting expression for the ion resonant electric field, it is seen that parallel flows on the order of or greater than the ion thermal velocity can significantly impact the resonant electric field. While other machines have experimentally demonstrated that the resonant electric field is determined by the leading terms in the magnetic field spectrum, there have been no experimental attempts to determine the impact that the parallel flow has on the resonant electric field at the time of this writing. When taking this into account, the parallel flows cause the resonant electric field to increase by a factor of 2.5 in QHS configuration compared to the its calculated value assuming there are no parallel flows. In other configurations such as Mirror and F14 or when the neutral density is increased, the increased damping shifts the resonant electric field to a lower value. HSX would provide a unique environment in which to observe the resonant electric field change in different configurations that have different viscous damping, but the same dominant (4,1) magnetic mode.

6.2 Implications of the Dependence of the Resonant Electric Field on the Parallel Flow

As mentioned in Chapter 2 of this document, the electron root has not been observed in HSX, despite neoclassical calculations predicting a large electron root in the core.

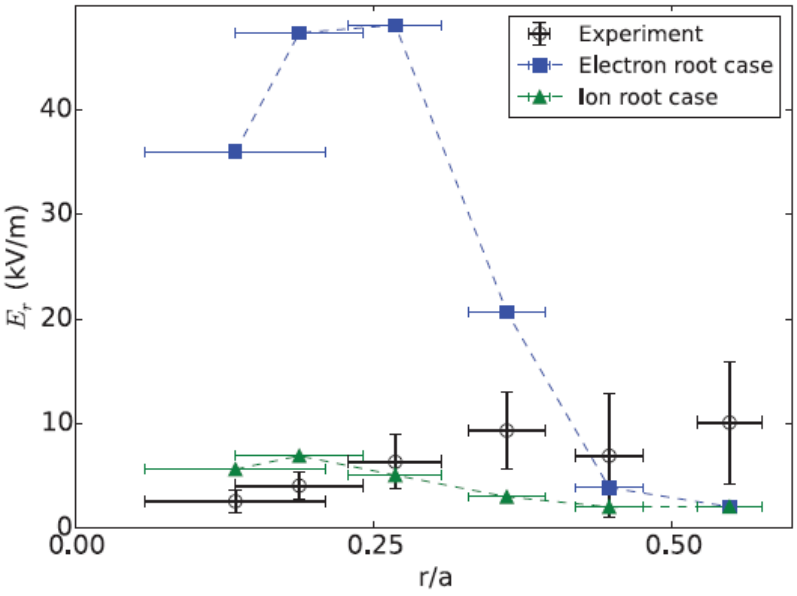

Figure 6. 1 The radial electric field in HSX as a function of r/a. The predictions of the electron root (blue squares) and ion root (green triangles) cases are shown in and compared to experimental measurements (black crosses) [1]

Figure 6. 1 shows that measurements of the radial electric field in the core of HSX point to the existence of an ion root. However, Jeremy Lore has performed calculations using neoclassical codes, such as DKES and PENTA, to predict which roots would be seen in the plasma and found that the ion root should not exist in the core.

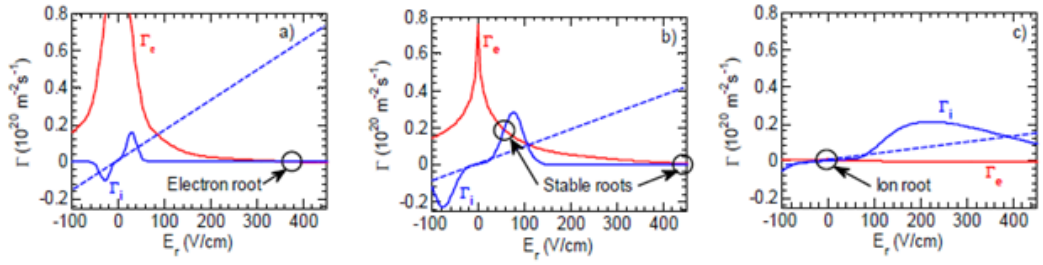

Figure 6. 2 Neoclassical particle fluxes versus E_r for three different radii: r/a=0.1, T_e=2keV, T_i=70eV (a); r/a=0.3, T_e=750eV, T_i=60eV (b); r/a=0.5, T_e=300eV, T_i=55eV (c). The ion particle flux ignoring the effect of the resonance is shown as a dashed line for reference. *[2]*

As seen in Figure 6. 2a, created with the PENTA code, the electron root should be visible in the core of HSX as the ion root does not exist. The peak in ion flux in this figure corresponds to the resonant electric field discussed in this work. Table 6.1 is a comparison of the resonant electric fields estimated from Figure 6. 2 for the three r/a locations to the approximation to the resonant E_r obtained from Equation 4.32 as well as from the full calculation of the poloidal viscosity as given by Equation 4.24. For both the approximation and the full calculation, the parallel flow was set to zero. Similar to the result shown in Figure 4.2, the approximation of the resonant E_r is about 60% of the full calculation. The PENTA value of the resonant E_r agrees well with that obtained from the Shaing poloidal viscosity at r/a = 0.5 and not as well closer to the plasma core. The inference from this comparison is that PENTA does not take into account the parallel flow when calculating the resonant electric field. If for example there was a substantial parallel flow at the resonant E_r it is conceivable that the ion flux (in blue) at r/a = 0.1 would be shifted so that the peak would intersect the electron flux. This would allow for an ion root at the plasma core that is more in agreement with the experimental measurements.

r/a	Resonant electric field calculated by PENTA	Approximate resonant electric field calculated with Equation 4.32	Resonant electric field calculated with the poloidal viscosity given by Equation 4.24
0.1	3kV/m	3.00kV/m	4.49kV/m
0.3	8kV/m	7.69kV/m	12.7kV/m
0.5	20kV/m	11.8kV/m	19.9kV/m

Table 6.1 Resonant electric field calculated by DKES compared to Equation 4.32 and 4.20 for different r/a values assuming no parallel flow.

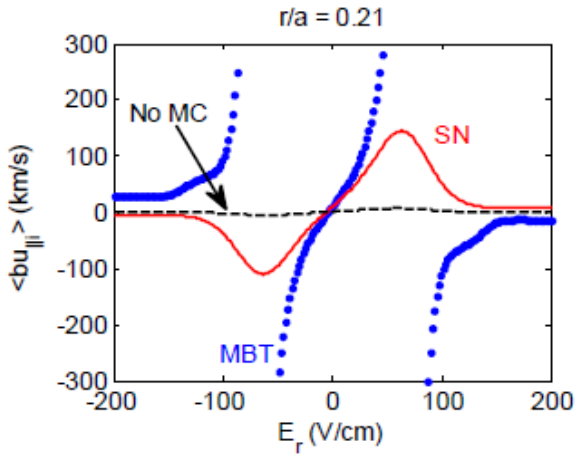

Figure 6. 3 Parallel flows versus the radial electric field for ions with momentum correction (red) and without (black) using the Sugama Nishimura method and the Maassberg-Beidler-Turkin method (blue), including the effect of the resonance for r/a=0.2. *[2]*

Figure 6. 3 is also from Lore's thesis [2] and provides further evidence that PENTA does not include the parallel flow in calculating the resonant electric field. As seen in the figure, there is a large parallel flow of 150km/s at the resonance, but the resonant electric field is only about 7kV/m. This electric field is close to the resonant electric field calculated in Table 6.1 for r/a =

0.3, but the calculations in Table 6.1 also assume no parallel flow. Previous calculations with the PENTA code have shown that an increased radial electric field drives parallel flow up to the ion resonance. As seen in Figure 6. 3, an increase in the radial electric field leads to an increase in the parallel flow which peaks around 8kV/m at r/a=0.2. This peak corresponds to the resonant electric field.

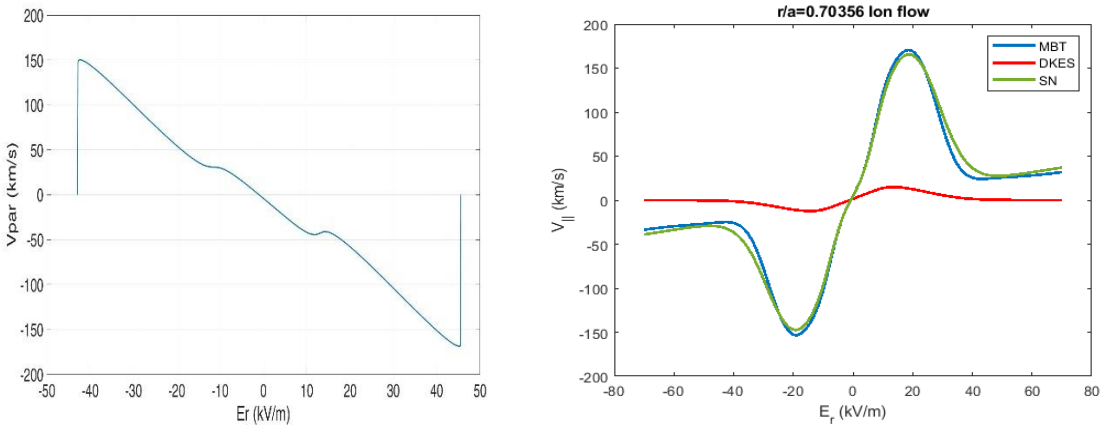

Figure 6. 4 (Left) Shaing model comparing the radial electric field to the parallel flow at r/a=0.7. (Right) PENTA calculation of the parallel velocity as a function of radial electric field. The Maassberg-Beidler-Turkin (MBT, blue), Sugama-Nishimura (SN, green), and Drift Kinetic Equation Solver (DKES, red) methods of calculation were used *[3]*.

Figure 6. 4 compares calculations made by PENTA against calculations made with the Shaing model for the parallel velocity and the radial electric field at r/a=0.7. For a direct comparison, the left plot in Figure 6. 4 was calculated by only using the parallel momentum balance equation, 3.2. As seen by comparing both sides, a large parallel velocity, about 150km/s, should be present at the resonant electric field. However, the resonant electric field predicted by each is much different, with the Shaing model predicting about 45kV/m, and PENTA predicting around 18kV/m. The prediction made by PENTA agrees more with the calculated resonant electric field seen in Figure 4.3, where the parallel flow was set to 0.

PENTA may be updated to include the effect of the parallel flow on the ion resonant electric field to see if its results then agree with this model.

As seen by comparing the left and right sides of Figure 6. 4, both PENTA and the Shaing model agree that at the resonant electric field, there should be a very large parallel flow. It should be noted that the fact that the calculated flows are similar is coincidental as PENTA does not take neutral damping into account in the results shown, but a flow well above the ion thermal velocity is calculated none-the-less. The main difference between the two models is the resonant electric field shifts with increasing parallel velocity in the Shaing model, while it does not in PENTA. A shift in the ion flux in Figure 6. 4a due to parallel velocity could lead to the electron and ion flux intersecting in multiple locations, possibly explaining why an ion root has been experimentally observed in HSX's core, but not the electron root.

6.3 Discussion of the plasma parameters and the transitional plasma behavior

In Section 5.1, we adopted an increased neutral density to approximate additional damping mechanisms not covered by the model presented in Chapter 3. While this approximation allowed Solution 3 to become more prevalent which led to an ease of illustrating stability and transitional behavior between solutions, there are some assumptions that may not be valid. For example, in Figure 4.6, very high parallel flows are sustained in the presence of external bias, on the order of 150 km/s, that surpass even the ion thermal velocity. Thus, in addition to turbulence as an additional damping mechanism, it would not be beyond the realm of possibility that shock phenomena could also occur to keep the parallel mass flow from reaching

such extreme values. In the work presented here the $\boldsymbol{V} \cdot \boldsymbol{\nabla V}$ term has been neglected. As neither of these phenomena increase linearly with respect to radial electric field (which could be true for other damping mechanisms not considered here), it is not entirely appropriate when considering an experiment that there only be three solutions to the momentum balance equations. If other damping mechanisms are also non-linear with respect to or independent of the radial electric field and peak in different locations than the poloidal viscosity, then that would give rise to more stable (and subsequently unstable) solutions to the momentum balance equations.

As seen in Section 5.4, the plasma undergoes a hysteresis-like behavior as it transitions between different states with increasing and decreasing external current. There is evidence to suggest that this is not simply an artifact of the simulation due to unrealistic machine parameters but would be seen experimentally in HSX. Hysteresis-like behavior has been observed experimentally in the Large Helical Device (LHD) [4].

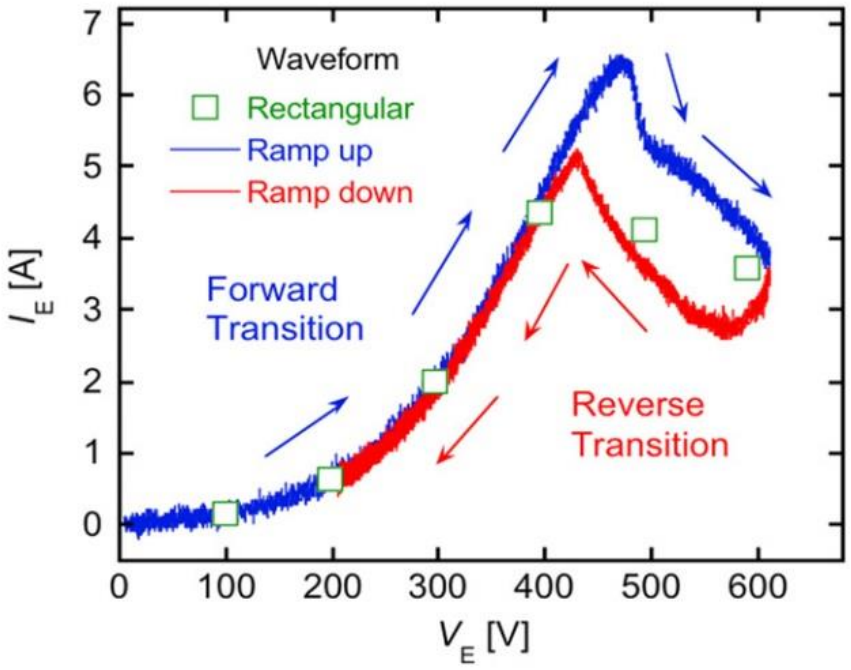

Figure 6. 5 Hysteresis behavior of a bias experiment in the Large Helical Device. The bias current to voltage ratio changes depending on if the voltage is being increased or decreased *[4]*.

As seen in Figure 6. 5 from LHD, there is a hysteresis that occurs as plasma parameters change during a bias experiment. In this experiment, an external bias voltage (and subsequently current) was ramped up to the point where the viscosity peak was surpassed and then brought back down to zero, similar to the simulation described in Section 5.4. Different plasma parameters at distinct bias voltages depending on whether the voltage was increasing or decreasing at the time. While not measured in the results shown in [4], this model predicts an additional hysteresis in the parallel flow that could be measured in future experiments. Similar behavior due to ramping biasing was seen in the Tohoku University Heliac [5] with multiple parameters exhibiting hysteresis behavior, as discussed in Section 1.3.

Finally, we address the speed at which the external current was ramped up in the simulation in Section 5.4. The total time of the simulation was chosen to be 20ms to allow E_r and $V_{||}$ to evolve clearly along the steady state solution spaces. However, HSX currently has a

discharge time of about 10ms, which includes the time it takes for the plasma to be formed and become stable. While the HSX upgrade (HSXU) will have longer discharge times, it is not currently feasible to replicate the simulation of Section 5.5 experimentally. Furthermore, should the external current ramp up faster such that E_r and especially $V_{\|}$ are not allowed to equilibrate, it could change the entire dynamic of the transition. As seen in Figure 4.5, the viscosity peak shifts as $V_{\|}$ increases. So, if $V_{\|}$ is not allowed time to increase very much, then it will not shift the resonance point as much. As seen by the vectors in Figure 5.4 and the time traces in Figure 5.5, E_r evolves faster in the space of Solution 1, so it is feasible that the transition from Solution 1 to Solution 3 would occur before the E_r value indicated by the resonance points in the figures showing steady-state solutions.

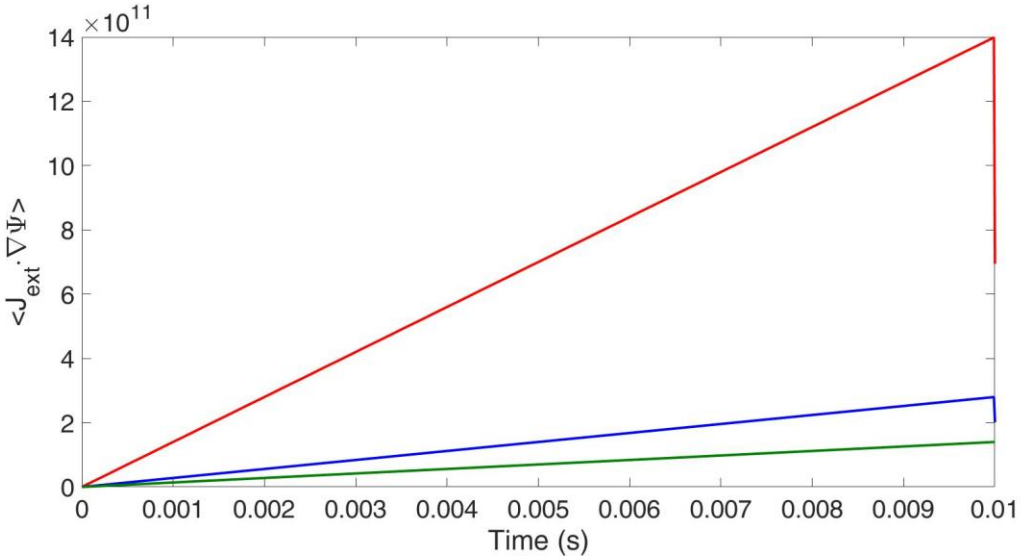

Figure 6. 6 Three external current ramping speeds applied to the simulation. The green line is the same as Figure 5.10, the blue line rises twice as fast as the green, and the red line rises ten times as fast as the green.

Figure 6. 6 shows three different external current profiles that were applied to the simulation. The green line is identical to the one shown in Figure 5.10, the blue line increases twice as fast as the green, and the red line increases ten times as fast as the green. In Chapter 5,

the rise speed of the green line was selected to be such that the parallel flow had time to evolve to 90% of its steady state value for a given value of external current. Now, the other lines are introduced to show what happens to the transitional behavior when the parallel flow is not given time to evolve.

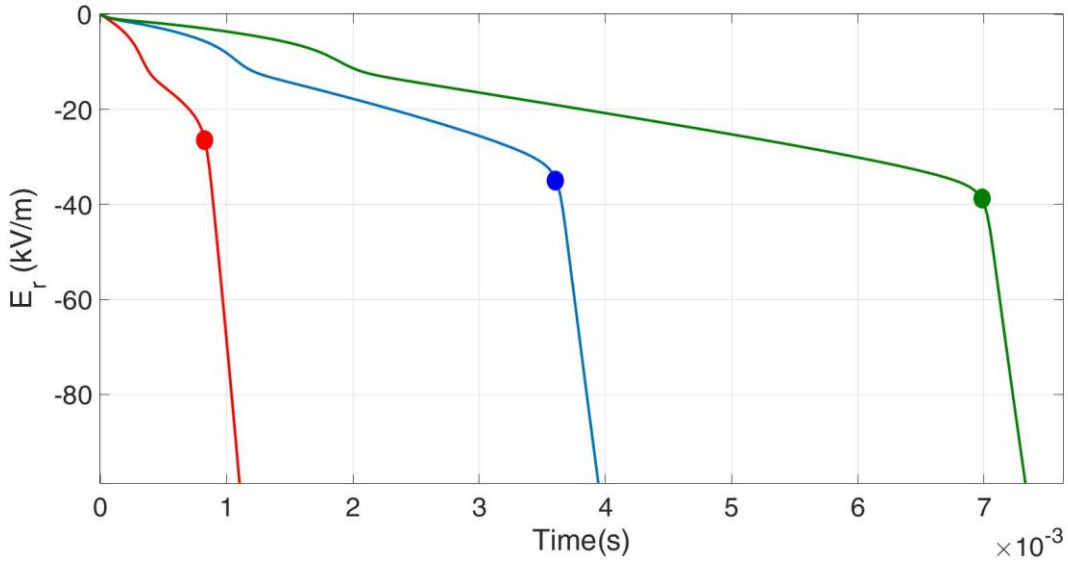

Figure 6. 7 The time evolution of the radial electric field as a function of time. The parameters between the three lines shown are the same, with the only difference being the rate at which the external current increases shown in Figure 6. 6. The points of transition are marked for each line.

Figure 6. 7 shows how the speed at which current ramps affects the point at which the plasma transitions from Solution 1 to Solution 3. The parameters for all three lines are the same with the only difference being the rate at which the external current is increasing, which is shown in Figure 6. 6. As such, not only does the red line transition faster, but it also does so at a lower value of the radial electric field. The radial electric fields at the time of transition are -31.82, -35.97, and -40.47kV/m for the red, blue, and green lines respectively. This is because the parallel velocity has not had time to evolve and shift the resonance point. If this holds true in experiments and the E_r value at which the transition occurs is a function of the external current

ramping time, and other non-linear damping mechanisms that give rise to new steady state solutions exist, as discussed previously in this Section, then it would also be feasible that the observation of intermediate modes could be dependent on the speed at which the current ramps up. This could lead to transitioning at a lower electric field and reaching to a theoretical stable solution that is located fully inside the hysteresis track.

6.4 Suggested Future Work

This work, while providing important insight into the behavior of the plasma in the presence of an external current leaves areas to expand in the future. The immediately obvious next step to this work is an experimental validation of the model. This can be done in a series of experiments.

In the first set of experiments, a bias electrode would be inserted into the plasma of HSX and turned on to a voltage that is below what is expected to hit the ion resonance. From there, the time evolution of both radial electric field and the parallel flow would be measured using both physical and optical diagnostics. These quantities would then be compared to the model in order to gain insight into additional damping mechanisms present in the machine. This can be done in all three configurations: QHS, Mirror, and F14 to see how the damping varies between each. The additional damping can then be added to the model in order to improve the predictions of the simulations.

With the model updated to include the experimental results, the next set of experiments would focus on reaching the ion resonance, beginning with the Mirror configuration as it has the lowest resonant electric field at its base parameters, as seen in Figure 4.13. The bias capacitor bank was recently upgraded to be able to reach voltages that this model predicts will allow the

ion resonance to be reached in all three configurations. Additionally, the capacitor bank outputs a square wave. This means that if the simulation results shown in Figure 6. 7 hold true and the resonant electric field decreases with increasing ramping time, then the ion resonance and the subsequent transition would be seen at lower voltages than predicted. Upon seeing the transition, the parallel flow and the radial electric field would be compared to the model. If the transition is seen and bias power supply is upgraded to enable a steady voltage ramp, then the hysteresis behavior between steady state solutions described in Chapter 5 may be observed.

During the biasing experiments, plasma parameters such as the temperature and density should be recorded in order to see how they change once an external bias has been applied. These changes, along with the addition of different damping mechanisms that are prevalent in HSX would allow for an expansion of the model, which could then be used to model other experiments with pre-existing bias experiments. In addition to expanding it in this way, the model can also be updated to include the new parameters that will be present in the HSX upgrade, which is nearing completion at the time of this writing.

References

[1] S. T. A. Kumar et al, "Determination of radial electric field from Pfirsh-Schluter flows in the HSX stellarator," *Nuclear Fusion,* vol. 57, no. 3, p. 036030, 2017.

[2] J. Lore, "Measurement and Transport Modeling with Momentum Conservation of an Electron Internal Transport Barrier in HSX," *University of Wisconsin-Madison,* 2010.

[3] S. T. A. Kumar, *Personal Communication,* 2020.

[4] S. Kitajima, "Transition of Poloidal Viscosity by Electrode Biasing in the Large Helical Device," *Nuclear Fusion,* vol. 53, no. 7, p. 073014, 2013.

[5] H. Takahashi and et al, "Hysteresis during transition into improved mode on biasing experiment under the electrode current control in Tohoku University Heliac," *Plasma Physics and Controlled Fusion,* vol. 48, no. 1, p. 39, 2005.

[6] S. Ding et al, "On the very high energy confinement observed in super H-Mode DIII-D experiments," *Nuclear Fusion,* vol. 60, no. 3, 2020.